Oxydation of Clay Nanoreinforced Polyolefins

Glennys Giovanna Gutiérrez

To cite this version:

Glennys Giovanna Gutiérrez. Oxydation of Clay Nanoreinforced Polyolefins. Materials. Arts et Métiers ParisTech, 2010. English. NNT : 2010ENAM0045 . pastel-00550432

HAL Id: pastel-00550432

https://pastel.hal.science/pastel-00550432

Submitted on 27 Dec 2010

2010-ENAM-0045

École doctorale n° 432 : SMI, Sciences des Métiers de l'Ingénieur

Doctorat ParisTech

THÈSE

pour obtenir le grade de docteur délivré par

l'École Nationale Supérieure d'Arts et Métiers

Spécialité “ Mécanique – Matériaux ”

présentée et soutenue publiquement par

Glennys Giovanna GUTIERREZ CASTRO

le 30 novembre 2010

OXIDATION OF NANOREINFORCED POLYOLEFINS

Directeur de thèse : **Gilles REGNIER**
Co-encadrement de la thèse : **Bruno FAYOLLE**

Jury

M. Roland SEGUELA	Directeur de Recherche au CNRS, UMT, Université Lille1, Lille.	Président
Mme Sandrine THERIAS	Chargée de Recherche HDR, Université Blaise Pascal, Clermont- Ferrand	Rapporteur
M. Mathew CELINA	Directeur de Recherche, Sandia National Laboratories, New Mexico.	Rapporteur
M. Jorge MEDINA	Professeur, CIPP - CIPEM, Université des Andes, Bogota.	Examinateur
M. Gilles REGNIER	Professeur, PIMM, Arts et Métiers ParisTech- Centre de Paris.	Examinateur
M. Bruno Fayolle	Professeur, PIMM, Arts et Métiers ParisTech- Centre de Paris.	Examinateur

THÈSE

Arts et Métiers ParisTech - Centre de Paris
Procédés et Ingénierie en Mécanique et Matériaux, PIMM

To my beloved family…

I want to express my gratitude to Professor Verdu and his wise advices at the right time, to Gilles and Bruno for their great support, their faith in my work and their camaraderie.

Also, I thank my friends for all the moments we shared and all the good memories.

I'm grateful to my family for the joy of life they impressed on me and their constant encouragement.

Finally I want to thank Gabriel, my soul mate, for being with me and walk this path together.

OXIDATION OF NANOREINFORCED POLYOLEFINES

INDEX OF SYMBOLS

%w	Per cent in weigh	
2θ	Scanned angle in X-ray diffraction	[°]
d	Silicate interlayer space	[nm]
d_0	Basal space of the clay	[nm]
D	Diffusion coefficient	[m^2s^{-1}]
D_o	Diffusion coefficient of polymer matrix	[m^2s^{-1}]
D_c	Diffusion coefficient of clay nanocomposite	[m^2s^{-1}]
D_{O2}	Oxygen diffusion coefficient	[m^2s^{-1}]
$D_{O2\ am}$	Oxygen diffusion coefficient of amorphous phase	[m^2s^{-1}]
L	Horizontal dimension of the silicate layer,	
	half-value of sample thickness	[nm, µm]
M_w	Weigh average molar mass	[kg mol^{-1}]
M_E	Weigh average molar mass between entanglements	[kg mol^{-1}]
$M_{w\ 0}$	Weigh average initial molar mass	[kg mol^{-1}]
p	Gas partial pressure	[Pa]
P	Permeability coefficient	[$m^2s^{-1}Pa^{-1}$]
P_{O2}	Oxygen permeability coefficient	[$m^2s^{-1}Pa^{-1}$]
$P_{O2\ am}$	Oxygen permeability coefficient of amorphous phase	[$m^2s^{-1}Pa^{-1}$]
S	Solubility coefficient	[mol $l^{-1}Pa^{-1}$]

S_{O2}	Oxygen solubility coefficient	[mol $l^{-1}Pa^{-1}$]
$S_{O2\ am}$	Oxygen solubility coefficient of amorphous phase	[mol $l^{-1}Pa^{-1}$]
W	Thickness of the silicate layer	[nm]
t_i	Induction time	[h]
r_s	Oxidation rate during stationary state	[mol $kg^{-1}h^{-1}$] [mol $l^{-1}h^{-1}$]
δ	Density	[kg m^{-3}]
s	Chain scission number	[mol l^{-1}]
[x]	Concentration of the “x” specie	[mol kg^{-1}] [mol l^{-1}]
X_{clay}	Clay mass fraction	
$X_{c\ by\ \delta}$	Apparent crystalline ratio	
r_W	Weigh average gyration ratio for a polymer	
r_{WE}	Weigh average gyration ratio for an entanglement	
γ_s	Chain scission efficiency factor	
α	Clay aspect ratio, stoichiometric coefficient	
ϕ	Volume fraction of the clay	
τ	Tortuosity factor	
β	Stoichiometric coefficient	
γ	Stoichiometric coefficient	
Ψ	Parameter depending on chemical structure and crystallization conditions.	
MMT	Montmorillonite, volumic fraction of organically modified clay (*MMT-O*)	

INTRODUCTION

Nanocomposite materials are attracting great search for better performing materials with improved thermal, mechanical, electrical and barrier properties. Using polymers as a matrix in this technology is advantageous due to their capability to improve such properties by incorporating nanofiller quantities lower than the 20 % vol required by conventional fillers such as talc, calcium carbonate, and glass fibers. Higher aspect ratios as those provided by clay layers permit stronger superficial contact between *MMT-O* and polymer justifying nowadays use of such clay as fillers.

Nanocomposites present good properties when they are produced, however the question is: does a clay nanocomposite exhibit a different oxidative behavior compared to those of the pure polymer? Do the improved permeability properties change the material thermo oxidative behavior under used conditions?

In the case of thermo-oxidation (above melting temperature), there are few studies regarding the nanofilled polypropylene and polyethylene aging kinetics, even so all were developed at high temperatures and integrating an empiric approach of study. Since these experimental data was obtained at very high temperatures, such information can not be extrapolated at lower temperatures.

The aging process induced by photo-oxidation in polymer-matrix nanocomposites has been studied by several researchers. Through those studies it was found that the incorporation of nanoclays decreases induction times during UV exposure, meaning that the organically modified montmorillonite (*MMT-O*) essentially accelerates the oxidation process.

The aim of this work is to study the montmorillonite filler influence over the oxidation process of unstabilized polypropylene and polyethylene at low and moderated temperatures between 60 ºC and 100 ºC by using a non-empiric method of approach to predict lifetime

A dual *MMT-O* nature will be looked closer in order to understand effects caused by it within the matrix degradation process: first aspect to be considered is the chemical role played by the clay during a simple thermo-oxidation process. At this point two main questions come up:

Do the degradation mechanisms of the pure matrix remain unchanged or they will be affected by the clay presence?

May the clay result an effective catalytic agent during a thermal oxidation process of the polyolefinic matrix?

The second aspect will be related to a clay attribute frequently mentioned in literature as the theory of the tortuous path when nanoclays are present. If nanoclay represents a physical barrier when small gas particles pass through nanocomposite films, does this impediment effect be remarkable when coupled with the thermal oxidation process? Does clay affect heterogeneous thermal oxidation when oxygen diffusion limitations drive the oxidation process?

In order to get an answer to all these questions we tackled the problem from an experimental and a modelling point of view. A great experimental work is performed using independently two different unstabilized polyolefin/coupling agent/clay systems, each case of study will contribute to elucidate different aspects going deeper in the subject of the clay/polyolefin thermo-oxidation: polypropylene/*MMT* and polyethylene/*MMT*. At the same time, polypropylene and polyethylene matrix oxidation without filler are examinated.

Computational simulations of the thermo-oxidation process will be a counterpart of the practical observations: they are performed for both systems in homogeneous and heterogeneous conditions (non controlled and controlled by oxygen diffusion) and for the temperature range under study.

To conclude this introduction section, the general text structure is provided. It accounted with a brief description of the content of each chapter, included with the aim to assist and guide the lector when looking for a desired topic.

Chapter I - Bibliographic Study - presents the state of the art of the thermal oxidation of clay nanoreinforced polyolefins. This compilation comprehends relevant aspects regarding nanocomposite composition and morphological characterization as well as the main features concerning the study of long term properties of polymer materials.

Chapter II - Materials and experimental Methods – provides a detailed description of raw materials, sample preparation and test conditions used for each experimental procedure performed in this work. Such information is stratified going from a small matter-scale to a macro scale: experimental procedures corresponding to the molecular scale are first presented, secondly those regarding morphologic and macroscopic scale.

Chapter III – Clay Nanoreinforced Polypropylene – corresponds to the study of the thermo-oxidation behavior of the montmorillonite / polypropylene system. This first case permits put in evidence main effects of the clay presence in the polyolefinic matrix. A kinetic study is performed at low and moderated temperatures. Furthermore, effects of oxygen diffusion limitations are explored especially when coupled with the thermal degradation.

Chapter IV – Clay Nanoreinforced Polyethylene – regards the case of study of the / polyethylene system. This section not only contains a kinetic study of the materials but also goes further into the catalytic effect induced by the clay in order to quantify it. Thanks to the nature of the matrix, the thermal oxidation and the oxygen diffusion phenomena could be independently studied. Additional aspects related to the oxidative degradation such as changes of molecular mass, crystallinity ratio and oxygen permeability changes are studied and linked in order to get to a in-depth analysis of the processes taking place. Finally, the influence of the oxygen diffusion limitations on the oxidation profiles is studied. This study includes simulations of degradation profiles using our diffusion limited oxidation modeling.

General Conclusions and Perspectives

INTRODUCTION

Les matériaux nanocomposites suscitent un intérêt grandissant grâce aux améliorations qu'ils apportent sur de nombreuses propriétés : propriétés thermiques, mécaniques, électriques ou barrières. L'utilisation de nanocharges dans une matrice polymère apporte de nombreux avantages du au fait qu'il suffit un moindre pourcentage de charge comparativement aux charges classiques (talc, carbonate de calcium, ou fibre de verre) pour améliorer ces propriétés. Les rapports de forme élevés caractérisant les feuillets d'argile permettent en effet d'optimiser la surface de contact entre la charge et la matrice.

Considérant que l'introduction de nanocharges améliore les propriétés des polymères, une question reste posée : quel rôle peut jouer la présence de ces nanocharges quant à la durabilité du nanocomposite comparativement à la matrice seule ? Est-ce-que ces nouvelles propriétés de barrière vont changer le comportement thermo oxydative du matériau sous les conditions d'utilisation?

Dans le cas de la thermo-oxydation quelques études traitent des nanocomposites à matrice polypropylène et polyéthylène mais ils ont été menés à hautes températures (largement supérieures à la température de fusion), ainsi leurs conclusions sont difficilement applicables à des vieillissements à températures modérés et basses.

Le vieillissement photoxydant de nanocomposite a été étudié par quelques équipes dans le monde. Ces études ont montré que l'incorporation de nanocharges à base d'argile conduit à diminuer le temps d'induction au cours d'une irradiation par UV, ce qui indique que la montmorillonite organiquement modifiée (*MMT-O*) accélère le processus d'oxydation. survenant à des faibles températures.

L'objectif de ce travail est d'étudier l'influence d'une charge de montmorillonite sur l'oxydation du polypropylène et du polyéthylène non stabilisés à basses températures en utilisant une approche non empirique permettant de prédire une durée de vie.

Deux aspects de l'ajout de *MMT-O* sur la dégradation de la matrice polymère seront abordés dans ce travail. Un premier aspect s'attachera à mettre en évidence le rôle « chimique » joué par la MMT dans le processus d'oxydation. On tentera de répondre aux deux questions suivantes :

Les mécanismes chimiques à l'origine de la dégradation à l'œuvre dans la matrice sont-ils modifiés par la présence de MMT ?

Si oui, la *MMT-O* peut-elle être considérée comme une catalyseur efficace des réactions d'oxydation dans le cas de la thermo oxydation de polyoléfines ?

Le deuxième aspect que nous étudierons traitera des conséquences bien connues de l'introduction de MMT-O sur les propriétés de transport à l'oxygène (par augmentation de la tortuosité). En effet si les feuillets d'argile réduisent la diffusion d'oxygène, quelles sont les conséquences de cette réduction sur un processus d'oxydation limité par la diffusion d'oxygène ? En d'autres termes, l'introduction de *MMT-O* va-t-elle modifiée l'hétérogénéité de l'oxydation lorsque celle-ci est contrôlée par la diffusion d'oxygène ?

Pour répondre à ces questions, on se propose de mettre en place une démarche expérimentale et de modélisation. La démarche expérimentale se basera sur l'étude simultanée de deux systèmes polyoléfines/agent de couplage/argile différents. Ces deux systèmes ne présenteront pas de stabilisant pouvant compliquer l'interprétation des résultats. Le premier système est un nanocomposite à matrice polypropylène, le deuxième ayant pour matrice un polyéthylène.
A titre comparatif, l'oxydation des matrices seules sera étudiée en parallèle.

Des simulations numériques de la cinétique de thermooxydation seront réalisées sur les deux systèmes en se basant sur une modélisation cinétique homogène d'une part et sur une modélisation cinétique hétérogène d'autre part.

Le présent manuscrit s'articule selon les chapitres suivants :

Le Chapitre I: *Etude Bibliographique* présente l'état de l'art sur la thermo oxydation des nanocomposites à matrice polyoléfine. Cette étude comprend différents aspects relatifs aux nano composites comme la caractérisation de l'état de dispersion des nanocharges dans la matrice et une description de notre méthodologie pour prédire la durabilité des polymères lorsqu'ils sont soumis à une oxydation.

Le Chapitre II : Matériaux et méthodes expérimentales décrit en détail les matériaux de l'étude, leur préparation et les conditions utilisées dans chaque méthode de caractérisation.

Les différentes méthodes sont regroupées par échelle d'observation : de l'échelle moléculaire à l'échelle macroscopique en passant par une échelle morphologique.

Le chapitre III : Nanocomposite à matrice polypropylène - traite de l'influence de l'incorporation de *MMT-O* sur l'oxydation du polypropylène. Les cinétiques d'oxydation du nanocomposite et de la matrice seules aux faibles températures d'exposition sont présentées et simulées par un modèle d'oxydation couplé à la diffusion d'oxygène.

Le Chapitre IV : Nanocomposite à matrice polyéthylène - a pour objet d'étudier l'ajout de *MMT-O* dans du polyéthylène. Ce chapitre contient non seulement une étude cinétique mais approfondit aussi l'effet catalytique induit par l'argile. Grâce à une spécificité du polyéthylène par rapport au polypropylène, il nous est permis d'étudier d'une façon indépendante la cinétique d'oxydation en conditions homogènes et hétérogènes (i.e. contrôlée par la diffusion d'oxygène). D'une façon complémentaire, la dégradation oxydante est étudiée au travers de mesures de masses molaires, de taux de cristallinité et de perméabilité à l'oxygène. On s'attachera à établir un lien quantitatif entre toutes ces mesures. Enfin, on mettra en évidence les profils de dégradations au travers de plusieurs techniques, les résultats expérimentaux étant systématiquement simulés en utilisant une modélisation de l'oxydation couplée à la diffusion d'oxygène.

Conclusions générales et perspectives

Chapter I

Bibliographic Study

Index of Figures

Index of Tables

Résumé Chapitre I

Etude Bibliographique

Ce chapitre consiste en une revue bibliographique concernant les polyoléfines nano-structurés à base de montmorillonite et les approches permettant de prédire leur comportement aux temps longs lorsqu'ils sont soumis à un vieillissement oxydant.

Apres un bref rappel concernant les polymères de cette présente étude, à savoir le polypropylène et le polyéthylène, on s'attardera à présenter les morphologies de ces matériaux nano composites en insistant plus particulièrement sur les techniques de caractérisation de ces morphologies. Les nano-charges utilisées dans cette étude sont de la famille des argiles disposées sous forme de feuillets (montmorillonite, *MMT*).

L'enjeu en termes de préparation des nanocomposites est de réaliser des mélanges dans lesquels les feuillets de montmorillonite sont bien séparés et dispersés dans la matrice polymère (intercalés ou exfoliés) de façon à favoriser les interactions avec la matrice polymère, qui est dans notre cas faiblement polaire.

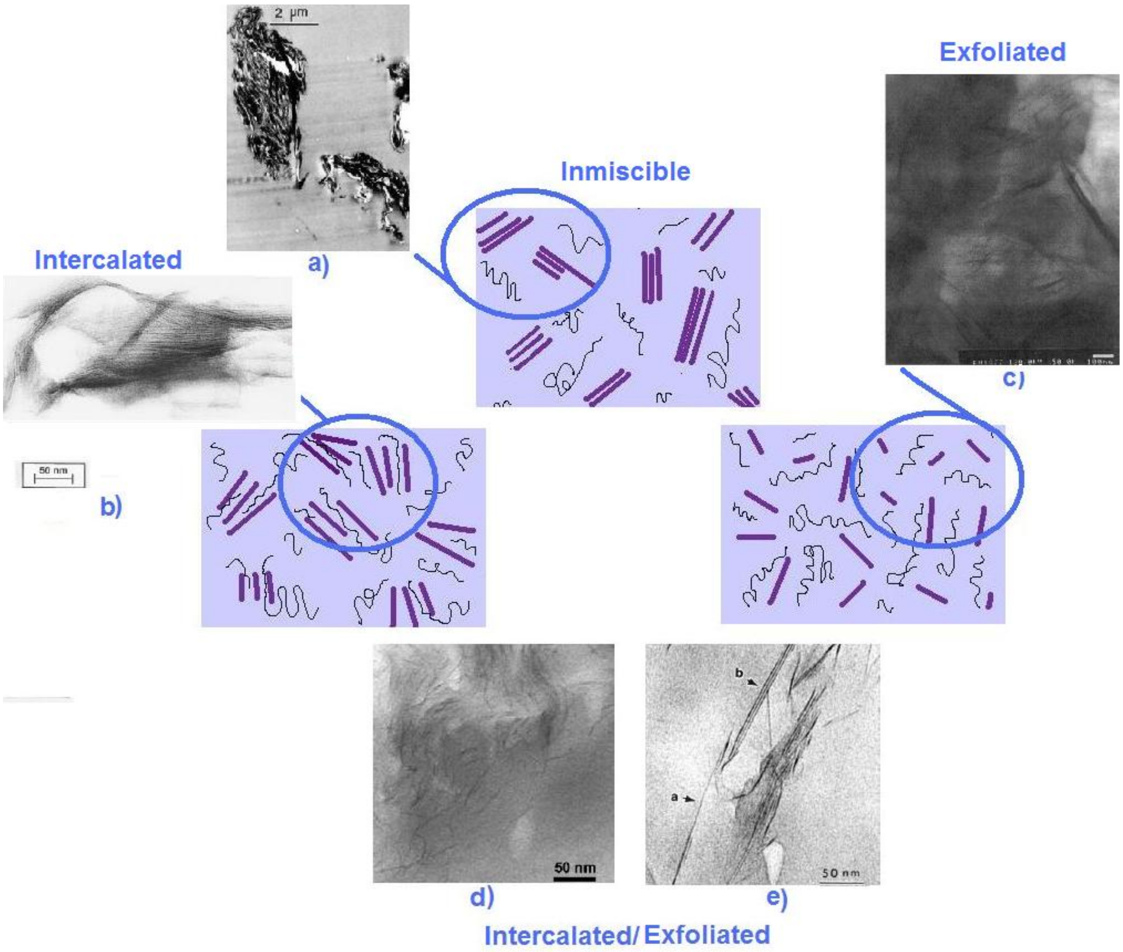

Etats morphologiques de dispersion des feuillettes argileuses pour les nanocomposites.

Trois voies sont disponibles pour assurer la meilleure dispersion possible des feuillets à l'échelle nanométrique : la première consiste à préparer le mélange charge-polymère en présence de solvant. S'il est judicieusement choisi, ce dernier doit permettre de favoriser la séparation des feuillets d'argile et la diffusion des chaînes de polymère entre ces feuillets. La deuxième voie consiste, toujours en présence de solvant, de réaliser la polymérisation du polymère en présence des charges. Enfin, la dernière voie et non la moindre d'un point de vue industriel, consiste à mélanger les charges avec le polymère quand celui-ci est porté à l'état fondu. C'est cette dernière voie qui a été choisie pour notre étude.

On rappelle ensuite les différentes techniques de caractérisation de l'état de dispersion des feuillets d'argile dans une matrice polymère : diffraction des rayons *X* et microscopie électronique en transmission.

Les propriétés attendues de ce type de matériau sont rappelées en portant une attention toute particulière sur les conséquences d'ajout de nano-charges sur les propriétés de transport vis-à-vis de gaz comme l'oxygène. On présente les modèles disponibles dans la littérature permettant de prédire l'influence de nano charges sur la perméabilité et donc aussi les coefficients de solubilité et de diffusion. En effet, l'ajout de feuillet à de faibles pourcentages (inférieurs à 10% en masse) doit conduire à une réduction du coefficient de diffusion de gaz comme l'oxygène au travers du nanocomposite. En théorie, cette réduction est liée à un phénomène d'augmentation de la tortuosité de la trajectoire des molécules de gaz dans le polymère entre les feuillets d'argile, ces derniers pouvant être considérés comme imperméable.

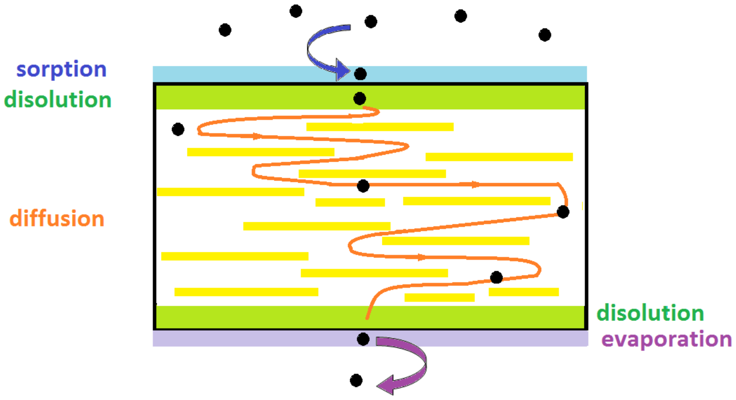

Schéma du mécanisme de perméation de gaz dans des nanocomposites à base d'argile.

La deuxième partie de ce chapitre bibliographique appelle les enjeux et les méthodologies mis en place pour prédire le comportement des polymères lorsqu'ils sont soumis à un vieillissement oxydant. La méthode que nous employons ici est résumée : il s'agit d'une méthodologie non empirique qui s’attache à décrire les mécanismes de dégradation qui sont à l’origine des modifications du polymère, à quantifier la cinétique de ces mécanismes et enfin de relier les modifications chimiques de propriétés macroscopiques. Dans le cas de nos matrices polyoléfines semi-cristallines, on s’intéressera plus particulièrement aux conséquences du phénomène de coupure de chaine induit par l’oxydation sur la morphologie cristalline (phénomène de « chimie-cristallisation »).

Sachant que les mécanismes d’oxydation du polypropylène et du polyéthylène ont font l’objet de nombreux travaux, on rappelle ici le modèle cinétique développée par notre équipe et les hypothèses qui y sont associées (homogénéité à petites échelles permettant l’utilisation de la cinétique chimique par exemple).Ce modèle est basé sur un schéma en boucle fermée comme suit :

$POOH \rightarrow 2P^{\bullet}$	k_{1u}	(Ia)
$2POOH \rightarrow P^{\bullet} + PO_2^{\bullet}$	k_{1b}	(Ib)
$P^{\bullet} + O_2 \rightarrow PO_2^{\bullet}$	k_2	(II)
$PO_2^{\bullet} + PH \rightarrow POOH + P^{\bullet}$	k_3	(III)
$P^{\bullet} + P^{\bullet} \rightarrow \mathit{Inactive} \quad \mathit{products}$	k_4	(IV)
$P^{\bullet} + PO_2^{\bullet} \rightarrow \mathit{Inactive} \quad \mathit{products}$	k_5	(V)
$PO_2^{\bullet} + PO_2^{\bullet} \rightarrow \mathit{Inactive} \quad \mathit{products}$	k_6	(VI)

Les phénomènes à l’origine d’hétérogénéité de l’oxydation sont présentés en insistant sur le cas où l’oxydation est limitée par la diffusion d’oxygène. En effet dans ce cas, la cinétique d’oxydation est contrôlée par la cinétique d’apport d’oxygène depuis la surface de l’échantillon si ce dernier est suffisamment épais. Ce contrôle se manifeste alors par l’apparition de gradient d’oxydation dans l’épaisseur de l’échantillon. Pour modéliser ce phénomène, on se basera sur un modèle couplant oxydation et diffusion dont chacun des paramètres seront identifiés d’une façon indépendante par méthode inverse.

Chapter I

Bibliographic Study

This chapter represents a compilation of the available information regarding the different aspects involved in a thermo-oxidation process and the methods used with traditional materials attempting to predict the aging process and the lifetime under different conditions.

In addition, different techniques and approaches used nowadays for the study of the thermal behavior of clay nanocomposite materials are also presented.

Finally, this background includes other implicit aspects such as the nature of the nanocomposites, their preparation process and their morphologic characterization.

1. General Aspects of Nanocomposites

In view of the differed properties and performance that nanocomposites show under specific environments and conditions, their activity is highly studied in the research field.

Nanocomposite materials are fabricated by mixing a small quantity of nano filler with a matrix. In the case of a polyolefin matrix, several filler materials can be used as aggregates: calcium carbonate, carbon nanofibers, aluminum and zinc containing isobutyl silsesquioxanes (*POSS*), graphite nanoflakes, carboxilate alumoxane nanoparticles, synthetic clay fibers such as fluorohectorite, short glass fibers, hydrotalcite, rhodamine B, talc, mica and clays [1,2,3,4,5,6,7,8].

Conventional polymer composites are filled with a high load of 20- 40% w in order to improve their properties, but also resulting in a weight increase. On the other hand, nanocomposites need much lower amounts of filler to reach remarkable improvements in their behavior. For instance, the load of a clay nanocomposite oscillates between 5 to 10%w with barely noticeable weight increase [9,10].

A great sort of polymers can be used as a matrix: vinyl polymers as methyl methacrylate, methyl methacrylate copolymers, acrylates, selective polymers such as *PVC* and ethyl vinyl alcohol copolymers; condensation polymers such as the nylon 66, polycarbonates, polybutadiene, epoxy polymer resins, and polyurethanes. Finally, the polyolefin family has as main exponents the polyethylene (*PE*) and polypropylene (*PP*), which are the materials used in the present study [11].

1.1 Polypropylene

The polypropylene (*PP*) is a vinyl polymer constituted by carbon and hydrogen molecules. It has the propylene as monomer in which a tertiary hydrogen has been substituted by a methyl group (Figure 1).

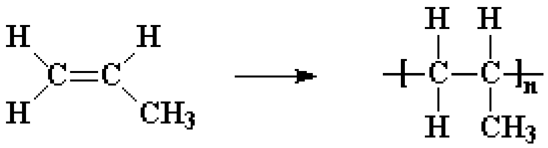

Figure 1 Polypropylene

The polypropylene is a low cost semi crystalline thermoplastic material. *PP* also shows good mechanical properties especially against fatigue and impact even at high temperatures (generally up to 100°C). Nevertheless, *PP* is ultraviolet (*UV*) sensitive and shows fragility under low temperatures. Indeed, due to the tertiary carbon (Figure 1) *PP* is more sensitive to oxidation process compared to polyethylene. This variety of properties explains why such material is a commodity widely used in diverse applications such as fibers, films, molded parts, liquid containers, geotextiles and reinforcement in asphaltic mixtures and for packaging applications, amongst others [9,12,13,14].

Polypropylene copolymers are also used in industry and they can be obtained by adding a co-monomer to the polymer chain without following a specific order. Such is the random polypropylene- ethylene copolymer case, where the ethylene content varies between 1 and 7%w in order to form an elastomeric phase ethylene – polypropylene flowing on a polypropylene matrix [15].

1.2 Polyethylene

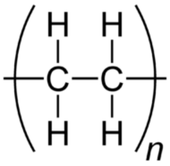

Figure 2 Polyethylene monomer

The polyethylene is another member of the vinyl family (Figure2) and its monomer is the ethylene. This thermoplastic material has not only excellent chemical resistance, good mechanical properties and lower density and *UV* sensitivity than the *PP,* it also presents good behavior at low temperatures due to its low crystal melting temperature. *PE* is widely used in industry for several applications such as pipes, cables, toys, communication equipment and packaging [16].

1.3 Montmorillonite

The montmorillonite (*MMT*) is the kind of clay the most widely used in industry as well as the bentonite and the saponite clays. The size of the clay is a determinant factor of the clay physical-chemical properties. In the montmorillonite case, it presents a very small particle size (less than 2 mm) and a high aspect ratio (between 10 and 1000). Such characteristics added to its high cationic interchange capacity (about 60 and 200 meq / 100g, the highest value in clays), and its specific area (between 60 and 300 m^2 / g), make the *MMT* a good candidate for nanofiller [17].

The montmorillonite is a phyllosilicate since its minimal entity is a layer. Such crystalline lattice is constituted by two tetrahedral silica sheets linked by oxygen molecules to a central octahedral sheet of alumina or magnesia [18]. (Figure 3). This configuration with chemical formula $(Si_2O_5)^{-2}$, known as 2:1 or T:O:T (Tetrahedric: Octahedric: Tetrahedric), corresponds to the main unit of the phyllosilicate and when assembled with equals constitutes a 1nm-thick layer that can be laterally extended from 30 nm to several micrometers larger [19].

The space between two stacks, is filled with water molecules and cations, is called gallery or interlayer. The interaction between cations such as Na^{+1}, Ca^{+1} and metallic oxides (especially Fe^{+3}) provides an electric charge equilibrium. One last characteristic of a clay is its basal space which comprises the length of a layer plus the length of a gallery [11].

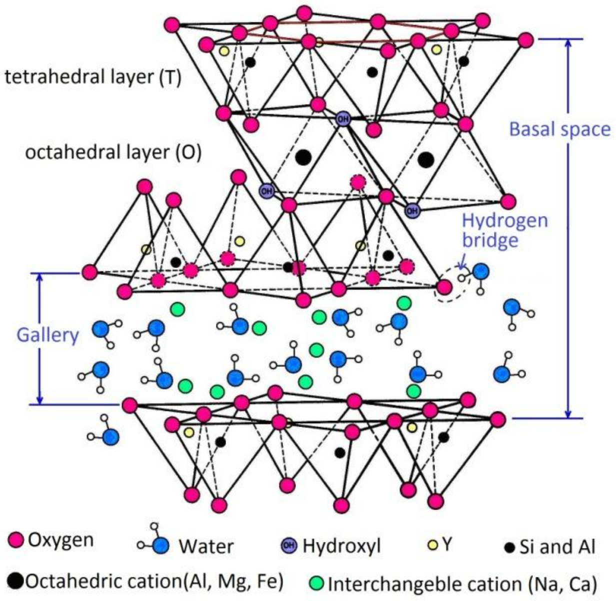

Figure 3 Montmorillonite, ***MMT***

The Van der Walls forces keeping the stack structure together are much weaker when compared to those generated by the ions located in the gallery. That is why phyllosilicates present a clear tendency to separate or exfoliate their sheets in a parallel fashion [20].

In order to use clay as a nanofiller, different authors as Shina Ray and Vaia [11,19] advised that the surface of the *MMT* must be organically modified to reduce surface energy of the clay sheets helping to develop stronger interactions between the phyllosilicate and the non-polar polymer matrix. Indeed, authors such as Okada, Giannelis and Biswas [21,22,23,24] confirmed that more important superficial interactions permit a better dispersion at a nanometric level and homogeneous dispersion of the inorganic phase in the organic (polymeric) domain, resulting in more remarkable improvements in the final properties of the nanocomposite. As an alternative or as a complement to the clay organic modification (*MMT-O)* a modified polymer matrix may be used to improve the clay dispersion in the matrix. These materials are commercially known as coupling agents.

1.4 Nanocomposite Preparation Methods

The preparation of a nanocomposite can be achieved through three methods [11,18,25,26]:

- Intercalation of polymer or pre-polymer from solution, also known as the exfoliation-absorption method: it involves the swelling of the clay in a solvent (such as water, toluene, or chloroform) where the polymer or pre-polymer is soluble. On account of the separation of the clay sheets into the solvent, polymer chains stick onto the gallery and therefore a permanent clay exfoliation takes place. Finally, the solvent is removed and the polymer layered silicate (*PLS*) structure remains. Despite the usefulness of this method in the production of thin films, it can only be used with certain polymers. For instance, Greenland et al have used *PVA* [27], Jeon et al used *HDPE* [28], and Kawasumi et al [29] experimented with liquid crystal. Moreover, it has a high environmental cost related to the solvent removal.

- In-situ intercalative polymerization: after swelling the clay in a solvent where the monomer is soluble, polymerization process is initiated by heat or radiation. Therefore, polymer chains are formed into the clay stacks reaching a reinforced *PLS* structure. The N6/MMT produced by Toyota is the most representative example of clay nanomaterial obtained by this method, which has been thoroughly described by Usuky et al [26].

- Melting Intercalation method: this technique involves a mechanical action used to mix the clay with the polymer in molten state in order to obtain either an intercalated or an exfoliated structure. The melting intercalation method does not require any solvent, thus open the possibility to make clay nanocomposites with any polymers that could not be processed by the previously mentioned methods. Nowadays, such method has become standard for the preparation of nanocomposites.

Different preparation methods and experimental conditions generate distinct types of nanocomposite morphology, with several levels of interaction between the components and phases present in the system.

1.5 Morphology of Nanocomposites

In nanocomposites three main different morphological states can be identified [11, 18]:

a) Immiscible: this state is characterized by the non-mixture of the clay into the matrix. Two distinct phases, with equivalent associations to those found in a microcomposite, can be seen. Figure 4 a) illustrates such situation in an immiscible novalac-based cianate ester nanocomposite obtained by Gilman et al [30] by mixing ester resin at high-shear with montmorillonite clay and coupling agent at 150°C.

b) Intercalated: this morphology corresponds to the first step in the separation of the clay stacks towards their segregation into individual clay sheets. In fact, clay presents a finite expansion of its layers allowing some polymer chains to penetrate into the gallery, it results in a well ordered multilayer structure constituted by alternated clay and polymer layers. Figure 4 b) is an example obtained by Vaia et al [19] by using melt state processing in a polystyrene montmorillonite system.

c) Exfoliated: the last step to attain a full separation of the clay stacks in a random but homogeneous distribution at nano and microscopic scale in the polymer matrix is called exfoliation. Extensive polymer chain penetration occurs into the gallery: each clay layer is surrounded by polymer chains permitting high superficial interactions improving material the behavior. To illustrate, Figure 4 c) corresponds to a fully exfoliated clay polystyrene nanocomposite obtained by Doh et al [31] using the in-situ polymerization method.

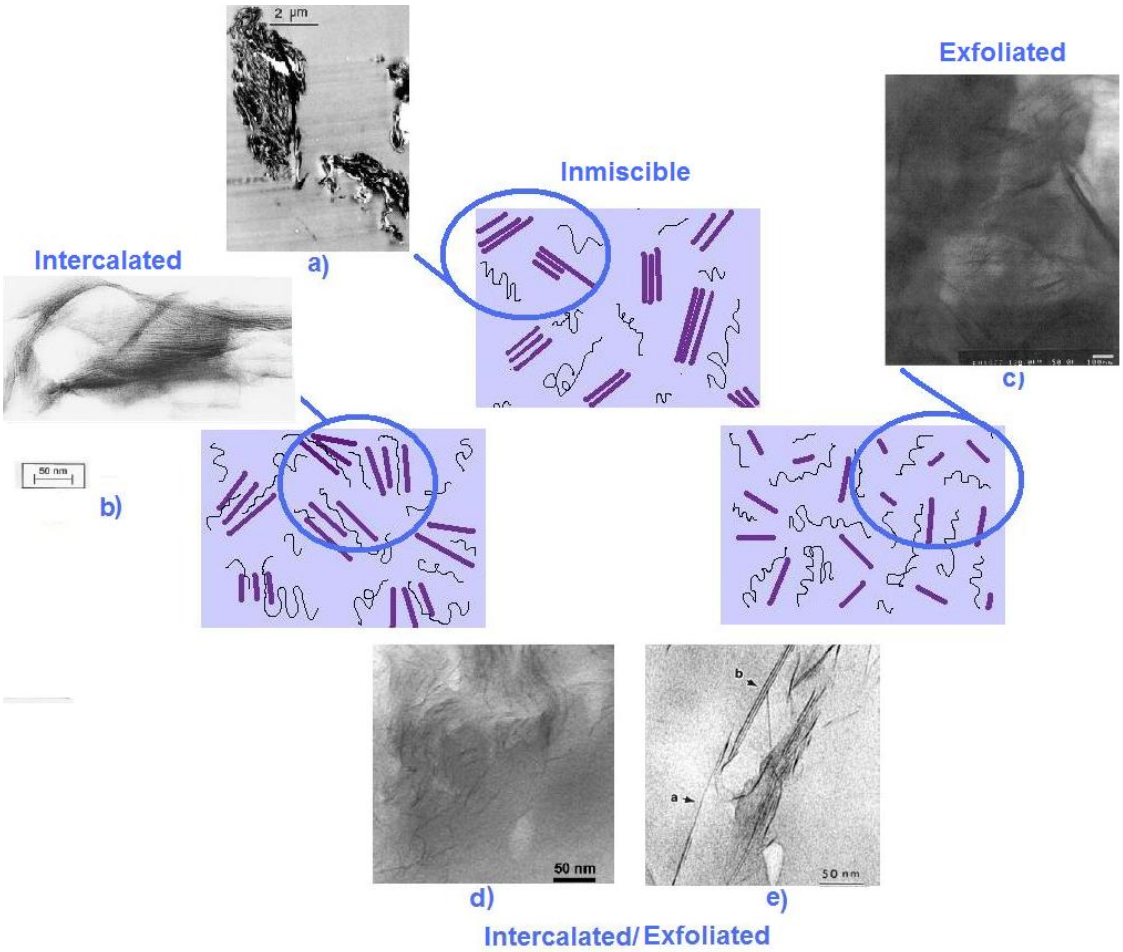

Figure 4 Morphological states in nanocomposites

Finally, two intermediary states can be seen: the immiscible-intercalate and the intercalate-exfoliated which correspond respectively to the transition state between immiscible and intercalate and between intercalate and exfoliate configurations. Their characteristics are a result of the mixing of the two predominant morphological states from which they are derived. Figures 4 d) and 4 e) exemplify intercalate-exfoliate arrangement for a clay high density polyethylene obtained by Swain et al [32] and for a clay polystyrene nanocomposites by Zhu et al [33], respectively. Such type of morphology is often obtained in of the nanocomposite prepared by using the melt state intercalation method.

1.6 Characterization of the Nanocomposite Morphology

Authors such as Shina Ray et al and Davis et al [11, 34] agreed that at least two methods should be employed to characterize the morphology of nanocomposites: the wide angle x ray diffraction (*WAXS*) and the transmission electron microscopy (*TEM*).

In the *WAXS* test, the angle 2θ is scanned between 11.3° and 90° so that the constructive interference caused by the crystalline structures can be detected. Fukushima et al [4] affirmed that it provides a convenient method to determine the interlayer space between silicate layers. Such "*d*" distance is an indicator of the degree of clay distribution in the matrix. For instance, in an intercalated sample there is an increase of clay–clay space when "*d*" is bigger than the basal space of the clay (d_o). Usually, "*d*" values are ranked between 1-4 nm (Figure 5). According to Ray et al [11], when the interlayer space after mixture (*d*) is bigger than 6-7 nm, it can be said that the clay sheets are fully exfoliated.

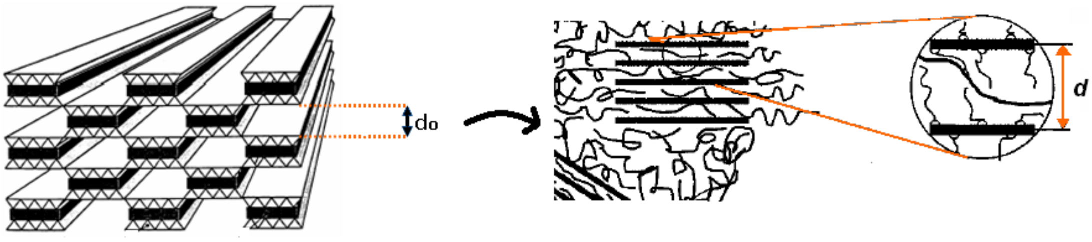

Figure 5 Clay monolayer: basal space

Despite the *WAXS* test is a good approach to get information on the nanocomposite morphology , it is not a fail proof indicator since it could present the same kind of response for two different morphologies: this occurs because constructive interference neither exists in the immiscible nor in the fully exfoliated cases. For this reason, Morgan et al [35] suggested using a complementary method (*TEM)* to inspect additional morphology aspects in order to corroborate information provided by *WAXS*.

The *TEM* test supplies a quantitative information of the internal distribution of the phases. Information describing size and geometry of the clay sheets is accurate and permits to calculate the aspect ratio of the clay. Besides the geometric description of the filler, it is possible to verify the dispersion degree of the clay into the matrix.

In addition to these two methods, some other tests leading to additional information to characterize different aspects of the nanocomposites [4,11,36]:
The evaluation of the filler thermal stability by Thermal Gravimetric analysis (*TGA*) [3,34], the crystallization behavior by Differential Scanning Calorimetry (*DSC*) [37], the stability of the morphologic configuration during small amplitude oscillatory shear experiments of rheology [38], the characterization of the orientation of the clay sheets by Fourier Transform Infra Red (*FTIR*) [39], Small Angles X-ray Scattering (*SAXS*) [11,36] and finally the interface structure and mobility by Nuclear Magnetic Resonance (*NMR*) [40].

1.7 Nanocomposite Properties

Several effects are produced by the clay insertion in polyolefins. However, the most affected properties are the mechanical ones. Several authors [5,19, 24, 32, 41,42,43] reported some other effects in polypropylene and polyethylene-based nanocomposites such as a decrease of thermal expansion, improvements of dimensional stability, higher solvent resistance, enhanced ionic conductivity, flame retardance and reduced gas permeability.

1.7.1 Gas permeability of Clay Nanoreinforced Polyolefins

The permeability of clay nanocomposites depends on several factors. Concerning the clay aspects the filler content and the morphological and chemical aspects like aspect ratio and interaction between filler and permeant are crucial. For the pure polymer and the coupling agent, their crystallinity and initial permeability properties are characteristics to be taken into account. Finally, additional practical aspects such as the ratio filler/coupling agent, the dispersion of the clay pallets relative orientation are also fundamental to better understand and predict the permeability properties of nanocomposites [44,45].

1.7.1.1. Semicrystalline Polymers

In the case of the pure semicrystalline polymer, Compañ et al [46] proposed an expression for the variation of the diffusion coefficient (D) in function of the crystalline ratio (X_c) and the temperature.

$$D_{O2}(X_c, T) = D_{am} * \exp\left(- A(T) * X_c\right) \qquad (1)$$

Under the premise that the crystalline phase is impermeable to gas, D_{O2} is the measured oxygen coefficient and D_{am} represents the coefficient of the amorphous phase of the polymer.

The A coefficient is the amorphous-crystalline phase rate conversion of polyethylene, which corresponds to the slope in the graph ln D against X_c. For oxygen diffusion at 23°C, A= -1.7461.

Furthermore, an expression for measured permeability P has been proposed taking into account X_c, A and the permeability of the amorphous face (P_{am}) [46].

$$P(T) = X_c * P_{am} * \exp\left(-A(T) * X_c\right) \tag{2}$$

Finally, given that the solubility of the amorphous phase (S_{am}) corresponds the material solubility (S) since the crystalline face is a gas barrier, P_{am} may be defined as:

$$P_{am} = D_{am} * S_{am} \tag{3}$$

1.7.1.2. Clay Nanocomposites

The presence of clay nanoparticles in a polymer matrix changes the permeation mechanisms by increasing the effective path length for diffusion when a permeant traverses the material from one surface to another [22].

The first step of the permeation – diffusion mechanism is the gas sorption on the sample surface: this stage is barely affected by the clay particles since it is directly related to the chemical interaction between polymer and permeant (which corresponds to the solubility or sorption coefficient, S). Next, permeant particles are dissolved in a thin layer to initiate a molecular diffusion process (described by the Fick’s diffusion law) until their arrival to the opposite dissolution layer in their way out of the sample (Figure 6). It is during the diffusion step that the clay particles play a crucial role in the barrier properties of the material: they act as a physical barrier creating a tortuous path through the polymer matrix, forcing the gas particles to pursuit longer distances than in a non filled matrix [47].

As a result of this steric effect, the small low-molecular weight particles have a restricted mobility and the rate of their mass transfer process is remarkably slowed down especially in the case of oxygen (O_2), carbon dioxide (CO_2), nitrogen (N_2) helium (He) and water molecules (H_2O) [11]. For these molecules, the gas permeability of the nanocomposite can attain a value between 50 and 500 times lower than that of pure polymer [45].

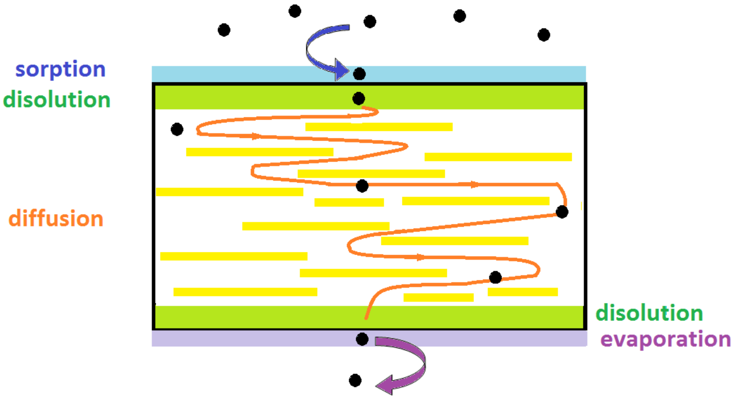

Figure 6 Scheme of the gas permeability mechanisms in a clay nanocomposite system

In order to illustrate the impact of the montmorillonite clay filler on real nanocomposites some examples are presented: in nanocomposites having a polystyrene (PS) matrix, permeability improvements of approximately 18% to 35% were found [48]. Similar results were reported for poly-ester systems charged at 2%w and 15%w of montmorillonite reaching respectively 20% and 58% of permeability decrease [49]. Finally, for a poly (ethyleneterephtalate) (*PET*) system with 2%w of montmorillonite, the permeability of the nanocomposite was 34% lower compared to the pure *PET* matrix [50].

In the case of polypropylene/organically modified montmorillonite/coupling agent systems, oxygen permeability reductions were ranged between 10% and 44% as reported by Golebiewski et al [51], and Mizadeh et al [52]. In the case of the polyethylene/organically modified montmorillonite (4- 5%w clay content) /coupling agent system the decrease of oxygen permeability was between 25% and 50% when compared to the pure matrix [53,54].

In order to describe the effect of nanoclay reinforcement on the permeability properties of polymer materials several models have been proposed: Barrer and Petropoulus presented a model in which regular arrays of clays platelets exist in the matrix and where the permeability properties vary in function of the proportion of the clay content.

Later, Nielsen proposed a semi-empirical model using very thin impermeable rectangular layers with thickness (W), finite horizontal extension (L) and aspect ratio $(\alpha = \frac{L}{W})$ [45]. Those layers are homogeneously dispersed perpendicularly to the flux of permeant. The solubility coefficient of the composite (S_c) is calculated in function of the solubility coefficient of the pure polymer (S_o) and the volume fraction of the clay (ϕ) (Equation 4).

$$S_c = S_0(1-\phi) \qquad (4)$$

The diffusion coefficient of the composite (D_c) is calculated as the ratio between the diffusion coefficient of the pure material (D_o) and the tortuosity factor (τ):

$$D_c = \frac{D_0}{\tau} \qquad \text{with} \qquad \tau = \frac{l'}{l} = 1 + \frac{L}{2W}\phi \qquad (5)$$

l' being the path length for the permeant diffusion in presence of filler, and *l* the path length for diffusion of the permeant in the pure matrix.

As a result, the permeability of the composite (P_c) is related with the permeability of the pure polymer (P_o) as :

$$\frac{P_c}{P_o} = \frac{1-\phi}{1+\frac{L}{2W}\phi} \tag{6}$$

The Nielsen's model provides good prediction of the nanocomposite materials permeability properties in the dilute regimen (when the clay has a large aspect ratio and volume fraction lower than 10). Cussler et al [55] proposed a renewed version of Nielsen's expression which can be used for semi-dilute regimen at volume fractions higher than 10 for systems where the clays presents a low aspect ratio. In this model the clay is represented not by rectangular but by randomly oriented circular layers and the gas permeability is driven not only by the tortuosity factor but also by pore constrictions. Moreover, Cussler's model includes the aspect ratio term (α) when expressing the relationship between the diffusion coefficient of the nanocomposite (D_c) and those of the pure matrix (D_o) (Equation 7).

$$\frac{D_c}{D_o} = \left(1+\frac{\left(\frac{\phi\alpha}{2}\right)^2}{1-\phi}\right)^{-1} \tag{7}$$

The relationship between the permeability of the nanocomposite and the one of the pure polymer is expressed as:

$$\frac{P_c}{P_o} = \frac{1-\phi}{1+\left(\frac{\left(\frac{\phi\alpha}{2}\right)^2}{1-\phi}\right)} \tag{8}$$

Other models have been proposed by varying the geometry of the filler, distribution and agglomeration of the platelets in the matrix [45]. Nevertheless, for most nanocomposites (mostly under dilute regimen) Nielsen's equation provides a good description of the experimental results.

2. Prediction of the Long Term Behavior

The progressive changes of the material structure with time are known as aging. Two classes of aging can be distinguished: physical and chemical. In the former, only reversible chemical and physical changes (no permanent modification of the polymer structure) take place. Those changes are classified in three categories: the structural relaxation observed in amorphous polymer, the absorption of solvent and small molecules by the polymer and the loss of additives initially present in the polymer.

On the other hand, the slow and irreversible process of a material structure and properties is known as chemical aging. It alters the material aspect and induce to profound permanent and irreversible changes of the macromolecular structure.

When the polymer does not interact with the environment, only anaerobic thermal aging is possible. Otherwise, several mechanisms are present during chemical aging, all of them alter the chemical polymer structure by creating or breaking atomic bonds: hydrolysis (polymer + H_2O), thermo-oxidation (polymer + O_2 + low to medium temperatures), photo-oxidation (polymer + O_2 + *UV)*, and radiolysis (polymer + irradiation) are some examples.

Nonetheless, pursuant to Colin et al [56], despite there are many considerable causes of polymer degradation, temperature deserves particular attention due to its enhancing aging power when coupled to another chemical aging source. Moreover, physical-chemical associations may exist during aging: they are related to stabilizers loss when polymer is in service. In practice physical and chemical aging phenomena often coexist and interact having an impact on the long term behavior.

2.1 Lifetime Definition

Since polymer behavior changes in time as its structure is modified like a degradation consequence, a Δt parameter is defined in order to determine the moment where the material cannot longer be used. According to Verdu [57], such lifetime can be defined as the time interval between the piece fabrication and the moment when certain property fails to attend the minimal threshold.

2.2 Methodologies to Study Long Term Behavior

Although aging is responsible for the failure of the material, it is not its start that causes the break. Indeed, secondary steps determine the actual moment where aging reaches a critical point. A general cause chain of material fail is schematized to illustrate the steps involved during the process (Scheme 1).

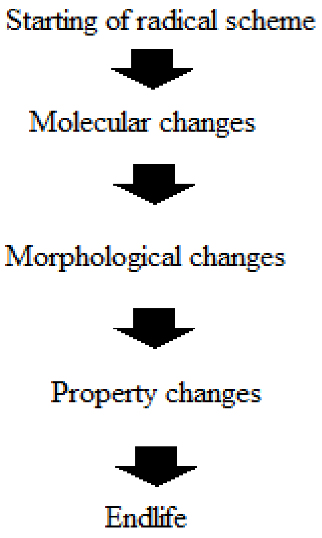

Scheme 1. Cause chain of material failing.

Chemical degradation leads to a molar mass decrease due to a chain scission process that will induce morphological modifications and derive to material endlife.

For instance in polypropylene, chain scission process is associated to carbonyl formation which is the predominant phenomenon during its oxidation (Figure 7):

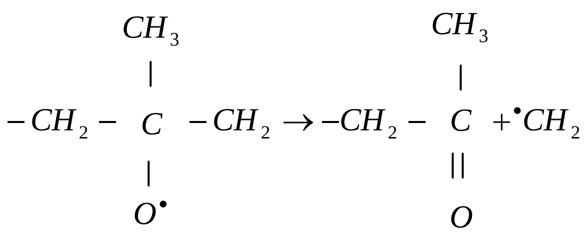

$$\begin{array}{ccccccc} & CH_3 & & & CH_3 & \\ & | & & & | & \\ -CH_2- & C & -CH_2 \rightarrow -CH_2- & & C & +{}^{\bullet}CH_2 \\ & | & & & || & \\ & O^{\bullet} & & & O & \end{array}$$

Figure 7 Schema of the β scission on the polypropylene tertiary carbon.

Fayolle et al [58] provided evidence to support that the chain scission causes the fall of molar mass, the decrease of molecular weight and a chain length reduction that bring to an easier disentanglement of the polymer chains. Such process induces the chemicrystallization process which involves morphological changes regarding the mobility of the amorphous phase and its integration to the crystalline phase. The thickening of lamella leads to rapidly attain the ductile – brittle transition criteria associated to a critical interlamellar thickness (l_c) under which the material becomes brittle [59]. Physical-chemistry provides a detailed description of the chemical changes occurring during such processes however, it does not take into account kinetic aspects of the failure. In practice fatigue tests studied the kinetics aspects of the failure process through tests basically focus on macroscopic reflex of the material inner configuration [60,61]. Nonetheless, they neglect how and why structure changes during degradation, which is definitely where the origin of such behavior can be found.

Empiric methods have been proposed in the 50’s in order to study the kinetics of the aging process at molecular scale, hence a more accurate prediction of the long term behavior of the materials was latter developed.

2.3 Empiric Methods for the Lifetime Prediction

They are based on accelerated aging tests at temperatures higher than use temperature, so that an equivalent aged state corresponding to the same material but exposed at lower temperature could be faster reached. Prior to experimentation, a property is chosen as critical and a lifetime ending condition is defined. Measurement and control of the property are then performed while material is been aged and a lifetime value is calculated at each experimental temperature using the fail criterion previously established. Next, assuming that material follows the Arrhenius law, an Arrhenius diagram $L_n t_f = f\left(T^{-1}\right)$ is built to graphically asses the best lineal regression. Finally a lifetime (t_f) is extrapolated for the use thermal condition:

$$t_f(T) = t_{f0} \exp\left(\frac{E_a}{RT}\right) \quad (9)$$

where T is the use temperature [K], R is the ideal gas constant [$\mathrm{Jmol^{-1}K^{-1}}$], t_{f0} is the pre-exponential factor [same time units than t_f], and E_a is the activation energy of the reaction [$\mathrm{Jmol^{-1}}$]. t_{f0} and E_a are constants determined from experimental data. Such approach supposes that the activation energy (E_a) does not vary with temperature and that the aging mechanism is independent of the exposure temperature. In other words, it is tacitly assumed that material attains an identical final aged state regardless the thermal route it follows, if the other exposure conditions remain unchanged. Le Huy et al [62] illustrated the Arrhenius principle for a "*y*" property, an endlife criterion "*Yi*", at three temperatures T_1, T_2, T_3 and the times t_1, t_2, and t_3 associated (Figure 8 a)). Finally, the relation between lifetime and absolute temperature is deducted by a thermal endurance profile (Figure 8 b)). The graphic is constructed as *1/T* in abscise and Ln *t* in the ordinate.

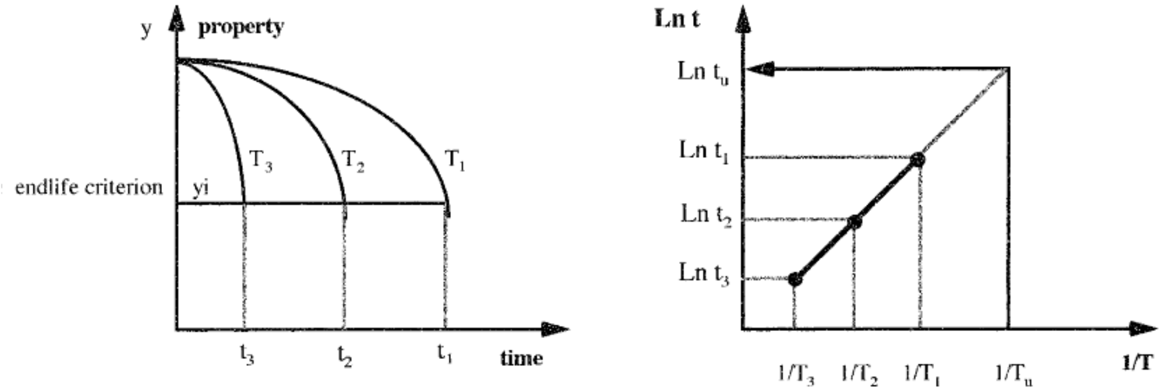

a) b)

Figure 8 Arrhenius methodology

When using an empirical method it is important to notice that such approach does not provide any information about the origin of the failure. Thus it does not permit to deal with the cause of fail in order to solve the problem. Besides, when using a thermal endurance profile in order to ascertain a lifetime under a determinate condition, extrapolations in logarithmic scale could induce great incertitude when put in linear time scale. As reported by Celina et al [63] non Arrhenius behavior has been observed due to differences of the activation energy for competitive process at different temperatures over a wide temperature range, consequently no linear extrapolation should be done.

Often, due to easy measurements lost weight is selected as the variable to be tracked during exposition at high and even at very high temperatures in order to deduct the kinetic material behavior. Nowadays, several authors apply such methodology to study thermal stability of nanocomposites by using thermo-gravimetric analysis, *TGA*. However, it has to be noted that *TGA* analysis performed at high temperatures is a very controversial method to be used in order to assess the thermal stability behavior at low temperatures.

Zanetti et al [64] have performed *TGA* to montmorillonite / ethyl vinyl acetate (*EVA*) system in oxygen and nitrogen atmospheres at temperatures ranged between 50°C and 550°C. They reported a thermal destabilization effect manifested as an increase of the initial degradation of the nanocomposite which could take place at lower temperatures than for the pure polypropylene. The use of clay speeds up deacylation from 350°C to 338°C and degradation from 470°C to 425°C.

Later, several research groups provided experimental evidence acquired by *TGA* on thermal stability improvements of polypropylene and polyethylene clay nanocomposites. In order to collect more information, additional parameters were included: not only the temperatures where the main changes started but also those where a 10% weight loss (T_{10}) and the maximum weight loss (T_m) are attained become indicators of changes in thermal stability.

Bertini [65] studied a montmorillonite/ coupling agent/ polypropylene system in temperature range between 50°C and 700°C. He found that under atmosphere air, nanocomposites can reach T_{10} and T_{rm} under 18°C and 31°C respectively. These temperatures are higher than those of the pure polymer. Qin et al [66] who studied a montmorillonite/ polypropylene system at 200°C confirmed such tendency reporting temperature degradation improvements between 20°C and 50°C for nanocomposites. Both research groups identify a possible *MMT* catalytic role at the beginning of polymer decomposition by diminishing the temperature at which weight loss starts compared to the PP pure. For polyethylene systems such as montmorillonite/high density polyethylene and *HDPE*/ coupling agent studied by Minkova et al [67] it was found that the degradation process of the nanocomposites proceeds by the clay organic modification which degrades at temperatures above 300°C. Also, Lomakin et al [68] described an accelerated formation and decomposition of hydroperoxides during thermal oxidation at temperatures up to 170°C. They associated such effect to a catalytic action of the *MMT-O*.

As a consensus, authors attributed thermal stability improvements of nanocomposites to physical effects of silicate layers which play a gas barrier role. However, such barrier effect involves all diffusion phenomena: neither oxidation products go out of the sample nor does environmental oxygen diffuses toward the sample bulk. In other words, increase of decomposition temperature can also be ascribed to the hindered diffusion of volatile decomposition products caused by the clay particles, not necessarily involving a thermal stabilization. Additionally, they associated such stabilizing effect to a degree of clay dispersion in to the matrix.

Finally, *TGA* is also used to deduce individual chemical reactions involved during thermal degradation at high temperatures. Authors such as Lomakin et al [69] have used such approach in order to describe the thermal oxidation of clay polypropylene and clay polyethylene nanocomposites. *A*s a result *TGA* indicates the evaporation of degradation products, this fact which may be associated to bond breaking. Results can be interpreted either as a multi step process made of independent steps or as a system composed by parallel, competitive or consecutive reactions [70].

According to Opfermann [71], the principle used to develop the kinetic analysis of *TGA* results supposes that material decomposes according to:

$$A_{solid} \rightarrow B_{solid/liquid} + B'_{gas} \tag{10}$$

The rate expression of a reactant "*e*", $\frac{de}{dt}$ is assumed to be defined by:

$$\frac{de}{dt} = k(T)xf(e, p) \tag{11}$$

where p is the product concentration, *k* is a kinetic constant that obeys the Arrhenius law $k = A\exp\left(\frac{-E_a}{RT}\right)$, A is the frequency factor, E_a is the activation energy and *R* is the ideal gas constant.

Nevertheless, knowing that aging is a complex process, using the Arrhenius requires certain precautions [72,73]:

- The Arrhenius approach can be reliably used when a process can be described just by an elementary reaction. This is not the case of the chemical ageing where at least three different reactions are involved.

- The global reaction rate of a complex process (v, is a linear combination of the rate reaction of its sub-reactions: $v= v^{\alpha 1}+v^{\alpha 2}+\ldots+v^{\alpha n}$; therefore E of the global reaction is $E=\alpha_1 E_1+\alpha_2 E_2+\ldots\ldots+\alpha_n E_{n.}$
- In the case of a complex process such as aging, which results from a succession of several elementary reactions most of them competitive at a given temperature, the Arrhenius law could be reasonably applicable in a temperature domain where the kinetic regimen of the elementary reactions does not change and chiefly, where the competitive relationship between concurrent reactions is not altered by the exposition temperature during testing. In practice, this represents a complex situation since different reaction temperatures have associated different proportion and distribution of aging products.

Celina et al [63] compiled experimental data obtained by several authors of thermo-oxidation studies for polymers such as polypropylene (*PP*), polyethylene (*PE*), high density polyethylene (*HDPE*) and some elastomers. They came to the conclusion that in all cases thermo-oxidation behavior presents a curvature indicating a non- Arrhenius behavior above a critical temperature. Such temperature varies for each polymer and evidences changes of kinetic regimen of degradation sub-reactions. When temperature rises thermo-oxidation is globally accelerated, meaning that each sub-reaction is concerned in function of its own activation energy.

Pursuant to thermal studies carried out by Gugumus [74], Richters [75] and Gijsman [76] mentioned by Celina et al [63], different activation energies for pure polypropylene thermal-degradation appear at temperatures above and below 83 ± 2°C. Transition of the thermo-oxidative regimen for polyethylenes was assessed either by thermal analysis of oxygen uptake above their melting point of approximatively 130°C. Such results suggest that not only thermal oxidation itself is concerned when temperature varies but also the oxygen diffusion process. Further experimental information regarding a non- Arrhenius behavior of the oxygen diffusion was provided by Gillen [77] for chlorosulfonated polyethylenes samples and changes in activation energy values were detected when calculated at lower or higher temperatures than 100°C. It suggests that oxygen diffusion phenomena may not follow a linear behavior in a large range of temperatures, hence, thermal degradation may present important deviations of the Arrhenius extrapolation when those two phenomena are coupled.

Those results indicate that a different non-empirical approach must be applied to study thermo-oxidation process, only a methodology based on a detailed kinetic model able to describe the non–Arrhenius behavior may provide realistic information of individual reactions and their temperature dependence.

2.4 Non Empiric Methods for the Lifetime Prediction

Methodology of non empiric study concerns several aspects related to different morphological scales. Scheme 2 presents main steps of the cause chain of material embrittlement which leads to endlife.

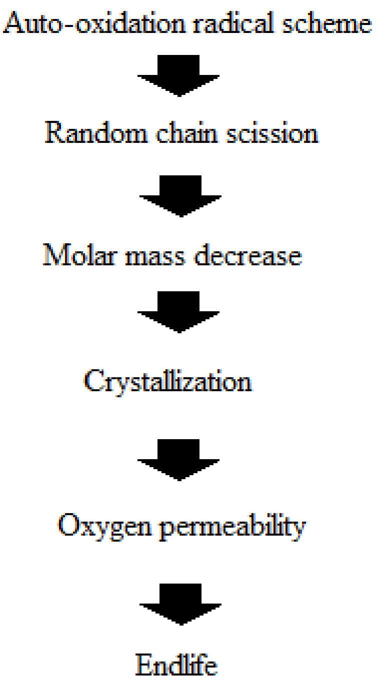

Scheme 2. Methodology of study of several processes involving different material scales during material embrittlement.

In the 40's, Bolland [78] proposed the first general kinetic model in order to describe the course of oxidation based on experimental identification of the oxidation products of linoleate thermo-oxidation at low temperatures between 45°C- 75°C.

As a first consideration, the proposed mechanism must fully describe the kinetic characteristics of the oxidation, secondly it ought to provide a complete explanation of the peroxide role and its catalytic action, and finally it should be consistent with experimental information. As a result, an auto-oxidation scheme involving the generation of several ion species, including peroxides, was proposed. The free radical mechanism consists in three steps: initiation, propagation and termination:

$$2POOH \rightarrow P^{\bullet} \text{ or } PO_2^{\bullet} \tag{12}$$

$$P^{\bullet} + O_2 \rightarrow PO_2^{\bullet} \tag{13}$$

$$PO_2^{\bullet} + PH \rightarrow P^{\bullet} + POOH \tag{14}$$

$$P^{\bullet} + P^{\bullet} \rightarrow Inactive\ \ products \tag{15}$$

$$P^{\bullet} + PO_2^{\bullet} \rightarrow Inactive\ \ products \tag{16}$$

$$PO_2^{\bullet} + PO_2^{\bullet} \rightarrow Inactive\ \ products \tag{17}$$

Here, the principle of kinetic equivalence is applied in order to describe using the fewest number of representative reactions, a group of sub-stages that independently may not have a remarkable effect on their equivalent reaction.

Such scheme became a useful tool to determine the overall rate of oxidation process and additionally clarify the origin of peroxide molecules during oxidation: their formation is preceded by a radical chain mechanism in which two types of radical are involved.

Even if the Basic Autooxidation Scheme (*BAS*) had been rapidly diffused to study thermal and photo–oxidation of olefins [79] proposed the first general kinetic model in order to describe the course of oxidation based on experimental identification of the oxidation products of linoleate thermo-oxidation at low temperatures between 45°C- 75°C there was no general consensus on the individual involved reactions.

Different alternatives were proposed in order to solve the *BAS* without simplifying assumptions regarding the oxygen excess or limitation involving interrelationship between termination constants and the assumption of a long kinetic chain length. Such hypotheses were often made to mathematically simplify the problem although, final results were not realistic. Gillen et al [80] proposed a general model that can be solved by using a mathematical approach. As a result, such approach predicts oxygen diffusion dependence under some conditions as well as the general allure of oxidation profiles when oxidation is diffusion limited. On the other hand, an analytical solution was proposed by Audouin et al [81] based on the assumption of a steady state for radical concentration. Besides the previous theoretical predictions such approach is capable to predict the main features of oxidation:

- Kinetic curves in agree with experimental results.
- Induction time value and its non-dependent behavior when the initial concentration of $POOH$ is low.
- Autonomy of the steady state rates regarding the rate of $POOH$ decomposition.
- Description of the non-Arrhenius behavior of the oxidation process.
- Prediction of the relationship between the induction times of initiation and termination process.

Verdu et al [82], proposed a numerical alternative in order to deal with a non-stationary state case. Nonetheless, the resulting system covers practically the same aspects than the analytical solution proposed by Audouin and it is much harder to solve due to the difficulty to obtain certain parameters.

Finally, Achimsky et al [83] defined a general which they named “Closed Loop Model” (*CLM)* aiming to study thin films of saturated polyolefins. Such system has the polymer branching as only source of alkyl radicals $P^{\bullet}$ and hydroperoxyls and permits the analysis of thermo-oxidation or photo-oxidation process at low and moderated temperatures.

Additionally, *CLM* assumed that oxygen is in excess thus equations involving $P^{\bullet}$ radicals were neglected. Since its definition such model has been successfully applied and enriched in our laboratory (Procédés et Ingénierie en Mécanique et Matériaux, *PIMM*, group of Vieillissement des Matériaux Organiques) in order to study thermo-oxidation process of a wide variety of polyolefin and thermoset materials [84,85].

2.5 Closed Loop Model, *CLM*

The closed loop model is composed of three stages: initiation, propagation and termination. The main characteristic of such scheme is the production of its own initiator (hydroperoxides) as an oxidation product during propagation reactions, thus hydroperoxyde group produced during initiation and propagation accumulates in the material inducing an autocatalytic behavior. This tendency lasts until neutralization of radical species through reaction with similar result in the creation of inactive products.

2.5.1 Initiation Reactions

Since hydroperoxyde $POOH$ decomposition constituted the sole source of radicals alkyl $P\bullet$ and peroxyl $PO_2^{\bullet}$ to initiate the radical chain equation (I) is a general form to represent the initiation reaction [85]:

$$\lambda POOH \rightarrow \alpha P^{\bullet} + \beta PO_2^{\bullet} \qquad k_1 \qquad \text{(I)}$$

where λ, α and β are coefficients that characterize hydroperoxide decomposition mode. In the unimolecular case $\lambda = 1$, $\alpha = 2$ and $\beta = 0$ and for the bimolecular situation $\lambda = 2$, $\alpha = 1$

and $\beta = 1$. Their respective equations are identified as (Ia) and (Ib) and have speed constants k_{1_u} and k_{1_b} respectively.

$POOH \rightarrow 2P^{\bullet}$	k_{1_u}	Unimolecular (Ia)
$2POOH \rightarrow P^{\bullet} + PO_2^{\bullet}$	k_{1_b}	Bimolecular (Ib)

Verdu et al [81] highlighted that the kinetic importance of the $POOH$ decomposition at low and moderated temperatures is related to the fact that such step is the slowest reaction in the degradation reaction chain, thus, it virtually governs the oxidation process. For instance, in the case of unimolecular initiation the increase of the $PO_2^{\bullet}$ and $P^{\bullet}$ concentrations is related to the square root of the $POOH$ concentration.

Mechanism of Unimolecular Reaction ($\lambda = 1$, $\alpha = 2$ and $\beta = 0$)

As mentioned before, each equation presented in the *CLM* is a representative reaction of the individual sub-reactions involved in a single step. Following, the mechanism of the unimolecular initiation shall be described in detail [56]:

The first step is the homolytic dissociation of one single hydroperoxide molecule:

$$POOH \rightarrow PO^{\bullet} + {}^{\bullet}OH \qquad (I_{u1})$$

Steps I_{u2} and I_{u3} correspond to reactions followed by the peroxyl and the hydroxyl ${}^{\bullet}OH$ radicals when they react with the substrate PH. A "α" fraction of the peroxyl radicals will follow the main reaction route and the remaining fraction $(1-\alpha)$ will follow an alternative reaction to produce alkyl radicals (I_{u4}).

$$\alpha PO^{\bullet} + \alpha PH \rightarrow \alpha POH + \alpha P\bullet \qquad (I_{u2})$$

$$^{\bullet}OH + PH \rightarrow P\bullet + H_2O \qquad (I_{u3})$$

$$(1-\alpha)PO^{\bullet} \rightarrow (1-\alpha)P=O + (1-\alpha)P\bullet \qquad (I_{u4})$$

$$POOH + (1+\alpha)PH \rightarrow 2P^{\bullet} + \alpha POH + (1-\alpha)P=O + H_2O \qquad (I_u)$$

Since reactions I_{u2}, I_{u3} y I_{u4} are very fast reactions it can be consider that unimolecular decomposition directly produces $P^{\bullet}$ radicals, as it is assumed in the general equation.

Mechanism of Bimolecular Reaction ($\lambda = 2$, $\alpha = 1$ and $\beta = 1$)

The first step of the mechanistic scheme corresponding to the bimolecular decomposition is a homolytic dissociation of one of the $POOH$ molecules (just as in the unimolecular case) associated to a heterolytic division of the second hydroperoxide unit (I_{b1}):

$$POOH + POOH \rightarrow PO^{\bullet} + ^{\bullet}OH + POO^{\bullet} + H^{\bullet} \qquad (I_{b1})$$

Reaction of $PO^{\bullet}$ with subtract is represented by equations I_{b2} and I_{b3}:

$$\alpha PO^{\bullet} + \alpha PH \rightarrow \alpha POH + \alpha P\bullet \qquad (I_{b2})$$

$$(1-\alpha)PO^{\bullet} \rightarrow (1-\alpha)P=O + (1-\alpha)P\bullet \qquad (I_{b3})$$

$$POOH + POOH + \alpha PH \rightarrow PO_2^{\bullet} + P^{\bullet} + H_2O + \alpha POH + (1-\alpha)P=O \qquad (I_b)$$

Achimisky et al mentioned the possibility of the existence of either a competition of the initiation mode or a predominance of one mode in function on exposure temperature [86]. Colin et al [56] pointed that the initiation mode is done in function of the exposure temperature and the initial concentration of hydroperoxide $POOH_0$ which is kinetically equivalent to the radical species present in un-aged polymers [81].

Metallic Catalysis

Audouin et al [81] suggested that the metal catalysis may be integrated as an additional act of the initiation step preferably at low or moderated temperatures, argument reinforced by experimental results obtained by Gijsman et al from their polypropylene titanium Ti^{+3} system [76]. Such reaction induces a reduction of induction time in a degree related to the metal amount, however it would not modify the steady state [82]. Reaction (I_m) with speed constant k_{1m} is always competitive with hydroperoxide decomposition reactions (I_u and I_b).

Complex transition metals such as iron and copper follow auto-oxidative reactions in order to decompose hydroperoxide molecules. The catalytic reactions for a bivalence metal ion (I_{m1}) and (I_{m2}) with peed constants k_{1m_1} and k_{1m_2} are [87]:

$$POOH + M^{n+} \rightarrow PO^{\bullet} + M^{(n+1)+} + HO^{-} \qquad k_{1m_1} \qquad (I_{m1})$$

$$POOH + M^{(n+1)} \rightarrow POO^{\bullet} + M^{n+} + H^{+} \qquad k_{1m_2} \qquad (I_{m2})$$

$$POOH + POOH \rightarrow PO^{\bullet} + POO^{\bullet} + H_2O \qquad k_m \qquad (I_m)$$

The action of metal particles is based on the formation of active radicals which prime the initiation reaction and transformation of hydroperoxides in secondary oxidation products such as ketones, alcohols, aldehydes and carboxylic acids.

2.5.2 Propagation Reactions

This stage involves the addition of oxygen to the alkyl radical $P^{\bullet}$ to form a peroxyl radical $PO_2^{\bullet}$ (reaction II) followed by one hydrogen extraction, producing one hydroperoxide molecule and one alkyl radical (reaction III). PH is the substrate, k_2 and k_3 are the kinetic constants corresponding to reaction (II) and (III) respectively.

$$P^{\bullet} + O_2 \rightarrow PO_2^{\bullet} \qquad k_2 \qquad \text{(II)}$$

$$PO_2^{\bullet} + PH \rightarrow POOH + P^{\bullet} \qquad k_3 \qquad \text{(III)}$$

The reaction (II) is very fast (k_2 has order of magnitude ranked between 10^8 and 10^9 $\text{lmol}^{-1}\text{s}^{-1}$) [87] thus another reaction is hardly competitive with it even though under certain oxygen pressure conditions such reaction can be diffusion controlled [57]. The rate of the hydrogen extraction (reaction III) depends on the bond strait of dissociated energy for hydrogen molecules. In terms of hydrogen abstraction, tertiary hydrogens are the first to be removed, followed by secondary hydrogens and finally primary hydrogens [88]. George et al [89] indicated that for polypropylene such hydrogen abstraction happens in tertiary hydrogens due to its high reactivity. On the other hand, in the case of polyethylene, hydrogen extraction is made from secondary carbons.

In the polyethylene case the hydrogen abstraction proceeds:

$$POO^{\bullet} + \left[CH_2 - CH_2\right]_n \rightarrow POOH + \left[CH_2 - \underset{\bullet}{C}H\right]_n$$

For polypropylene:

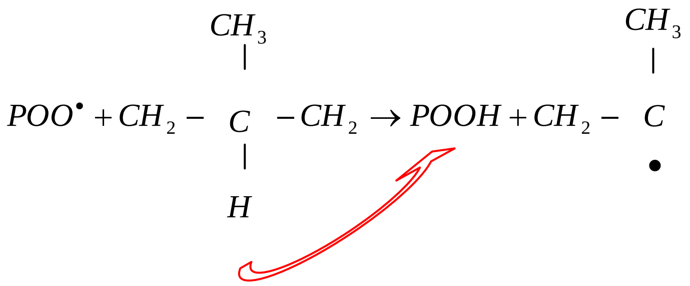

$$POO^{\bullet} + CH_2 - \underset{\underset{H}{|}}{\overset{\overset{CH_3}{|}}{C}} - CH_2 \rightarrow POOH + CH_2 - \underset{\bullet}{\overset{\overset{CH_3}{|}}{C}}$$

Besides the hydroperoxide molecules which are the main product of oxidation, several oxidation products such as aldehydes, peroxides, ketones, carboxylic acids, alcohols and hydroxyls may also be produced in small quantities in function of the termination reactions efficiency [90,91,92].

2.5.3 Termination Reactions

The propagation step finishes when all active radicals $P^{\bullet}$ and $PO_2^{\bullet}$ are neutralized after reacting with equals and producing inactive compounds. Reactions (IV), (V) and (VI) with rate constants k_4, k_5 and k_6 are the main three routes of termination of a non-stabilized polymer:

$$P^{\bullet} + P^{\bullet} \rightarrow Inactive \quad products \qquad k_4 \qquad \text{(IV)}$$

$$P^{\bullet} + PO_2^{\bullet} \rightarrow Inactive \quad products \qquad k_5 \qquad \text{(V)}$$

$$PO_2^{\bullet} + PO_2^{\bullet} \rightarrow Inactive \quad products \qquad k_6 \qquad \text{(VI)}$$

According to Gillen et al [80], termination reactions between a very active radical and a less reactive one are very fast and the value of its speed rate is close to that of a termination between two highly reactive radicals (at low temperatures $k_4 > k_5 >> k_6$ is valid). According to radiochemical data, termination reactions involving alkyl radicals $P^\bullet$ at low or moderated temperatures are immediately converted into $PO_2^\bullet$. For that reason, reactions (IV) and (V) can be neglected in the case of oxygen excess [81].

2.6 Applied Kinetic Scheme

The constitutive equations of the *CLM* used in this study and their respective rate constants are:

$POOH \rightarrow 2P^\bullet$	k_{1u}	(Ia)
$2POOH \rightarrow P^\bullet + PO_2^\bullet$	k_{1b}	(Ib)
$P^\bullet + O_2 \rightarrow PO_2^\bullet$	k_2	(II)
$PO_2^\bullet + PH \rightarrow POOH + P^\bullet$	k_3	(III)
$P^\bullet + P^\bullet \rightarrow Inactive \quad products$	k_4	(IV)
$P^\bullet + PO_2^\bullet \rightarrow Inactive \quad products$	k_5	(V)
$PO_2^\bullet + PO_2^\bullet \rightarrow Inactive \quad products$	k_6	(VI)

A set of ordinary differential equations expressing the concentration changes of the involved reactive species is derived from this scheme. A general solution for these analytical expressions is sought without any simplifications regarding steady state conditions for radical concentrations, oxygen pressure, kinetic chain length or kinetic relationships between termination rate values.

$$\begin{aligned}\frac{d\left[P^{\bullet}\right]}{dt} &= 2k_{1u}\left[POOH\right] + k_{1b}\left[POOH\right]^{2} \\ &\quad - k_{2}\left[P^{\bullet}\right]\left[O_{2}\right] + k_{3}\left[PO_{2}^{\bullet}\right]\left[PH\right] - 2k_{4}\left[P^{\bullet}\right]^{2} - k_{5}\left[P^{\bullet}\right]\left[PO_{2}^{\bullet}\right]\end{aligned} \tag{18}$$

$$\begin{aligned}\frac{d\left[PO_{2}^{\bullet}\right]}{dt} &= k_{1b}\left[POOH\right]^{2} + k_{2}\left[P^{\bullet}\right]\left[O_{2}\right] - k_{3}\left[PO_{2}^{\bullet}\right]\left[PH\right] - k_{5}\left[P^{\bullet}\right]\left[PO_{2}^{\bullet}\right] \\ &\quad - 2k_{6}\left[PO_{2}^{\bullet}\right]\end{aligned} \tag{19}$$

$$\frac{d\left[POOH\right]}{dt} = -k_{1u}\left[POOH\right] - 2k_{1b}\left[POOH\right]^{2} + k_{3}\left[PO_{2}^{\bullet}\right]\left[PH\right] \tag{20}$$

Despite the fact that the reaction rate of the polymer decomposition ($PH \rightarrow P^{\bullet}$) is very slow when compared to the other reaction of the *CLM* and the concentration of the substrate can be considered constant $\left[PH\right] \approx \left[PH\right]_{O}$ in the majority of the cases, the concentration changes of the subtract PH may also be included in the *CLM*, for instance, in the case of high conversion rates where the substrate consumption is not negligible during reaction (Equation18):

$$\frac{d\left[PH\right]}{dt} = -\gamma_{1u}k_{1}\left[POOH\right] - \gamma_{1b}k_{1b}\left[POOH\right]^{2} + k_{3}\left[PO_{2}^{\bullet}\right]\left[PH\right] \tag{21}$$

where γ_{1u} and γ_{1b} are the available hydrogens that can be subtracted during the initiation step [93]:

$POOH \rightarrow PO^{\bullet} + {}^{\bullet}OH$	Decomposition	(Ia)
$HO^{\bullet} + PH \rightarrow P^{\bullet} + H_2O$	Hydrogen abstraction	(Ib)
$PO^{\bullet} + PH \rightarrow P - OH + P^{\bullet}$	Hydrogen abstraction	(Ic)
$PO^{\bullet} \rightarrow P = O + P^{\bullet}$	Chain β scission	(Id)
$POOH + (\gamma = 2 - \xi_1)PH \rightarrow 2P^{\bullet} + H_2O$ $+ (1 - \xi_1)P - OH + \xi_1 P = O$	Balanced equation	(I)

γ is an adjustable value, $-1 < \gamma < 2$.

The initial and boundary conditions to solve the system of differential equation are $[PO_2^{\bullet}] = 0$, $[P^{\bullet}] = 0$, $[POOH] = [POOH]_0$, $[PH] = [PH]_0$, where $[PH]_0$ $and[POOH]_0$ are the initial concentrations of the $[PH]and[POOH]$ species, respectively.

2.7 Heterogeneity Features of the Oxidation Process

Two main levels are concerned by heterogeneity: intrinsic heterogeneity and heterogeneity related to oxidation process.

2.7.1. Intrinsic Heterogeneity

Un-aged materials are not made by a homogeneous substance ergo initiation process ought to start around punctual imperfections [94] . Such defaults may refer to morphological gradients and textures, to the presence of two phases [89,95] (amorphous and crystalline) as in the case of a semi crystalline polymer such as polypropylene or polyethylene and to little imperfections created during processing by gradients of thermal fields.

At this level, heterogeneity can be studied by the changes of the molecular weight distribution: if after exposure the analysis of molar mass show that the initial weigh distribution does not change its shape but only shifts its average value to lower molecular weights, it is a homogeneous oxidation. Otherwise, oxidation process is heterogeneous (Figure 9) [96].

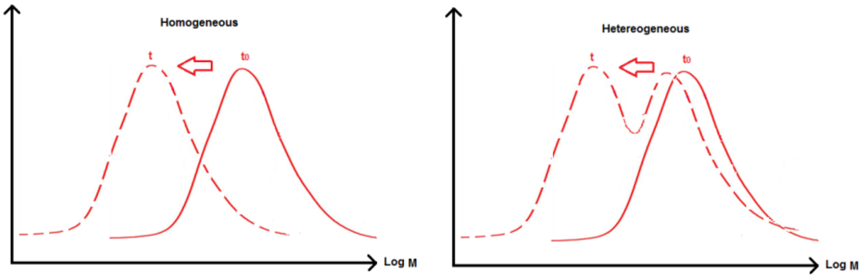

Figure 9. Effects of the homogeneous and heterogeneous degradation on mass distribution changes.

2.7.2. Heterogeneity Limited by the Oxygen Diffusion

The first aspect to be considered is that oxidation process at a mesoscopic scale (especially because morphology is directly concerned) is a heterogeneous process. Although it could be considered as homogeneous at a smaller scale, since crystalline phase is impermeable to oxygen and oxidation takes place only in the amorphous phase [97]. The oxidation can be treated as a homogeneous phenomenon and the local concentration of the oxidation products can be converted to average values of concentration ($[C]_{av}$) such as those provided by using the *CLM*:

$$[C]_{av} = [C](1 - X_c) \tag{22}$$

where X_c is the crystalline fraction of the polymer.

- Finally, the limitations caused by oxygen diffusion generate gradients of the oxidation products distribution in the thickness of the sample [98,99]. The gradients on the distribution of oxidation products are present when there is no oxygen excess during the oxidation process or in thick samples where the diffusion reaction is slower than oxidation, becoming, hence, the dominant phenomenon.

2.8. Phenomenon of Oxygen Diffusion

The phenomenon of oxygen diffusion is a mechanism followed by the oxygen molecules in order to pass through a membrane in which its gradient of concentration drives a solubilization of the gas into the matrix. Such molecular movements depend on chemical interactions between gas and matrix and on the rate between the size of the gas particles and the micro spaces into the matrix: these conditions are well described by the oxygen diffusion coefficient (D_{O2}) and the oxygen solubility (S_{O2}) of the gas into the polymer matrix [100].

The notion of gas diffusion makes allusion to permeability which corresponds to an intrinsic property of materials related to the flux of a fluid (oxygen in this particular case) trough them and which is inversely proportional to the thickness of the sample [100]. Fick's law of diffusion permits to model the permeation of the flux of a simple gas such as oxygen, nitrogen or carbonic gas (J) during a time interval through a surface in presence of a gradient of concentration dc/dx:

$$J = -D\left(\frac{dc}{dx}\right) \tag{23}$$

In order to resolve equation 23, the concentration of the gas can be calculated by using the Henry's law where the concentration of the gas is directly proportional to its partial pressure and its solubility (*S*):

$$c = S * p \tag{24}$$

Stivala [101] was one of the first authors who reported a thickness effect during thermo-oxidation on the rate of formation of total carbonyl content for 190 µm-thick polypropylene samples. Such behavior was explained by oxygen diffusion–control effects present in samples with a thickness bigger than 127µm. In the early 80's Billinghan and Calvert emphasized about the importance of the oxygen diffusion effects in the thermal oxidation of polyolefins at high temperatures and added that such effect should be more important in the photo-oxidation case under the same thermal conditions [102]. In the photo-oxidation case the oxygen limitation effect was found in the case of 200 hours of photo-oxidation at 23°C of 3mm-thick films of low density polyethylene [100]: for depths over 600µm the oxidation rates were diffusion controlled and reaction profiles were found.

Fairgrieve et al [98] made a distinction of the three zones generated by the oxygen diffusion limitations in a film sample: a first zone is comprised between the surface of the sample and a thickness in which oxygen diffusion does not limit oxidation reactions. After such thin film there is a second region where there are still no diffusion effects but when oxygen penetrates beyond such critical thickness the oxygen diffusion limitations start to manifest.

When taking into account the oxygen consumption term in the *CLM* oxygen diffusion limitations can be studied, permitting the prediction of features of the heterogeneous oxidation such as distribution of oxidation species in the material. This last point is fundamental in the case of polypropylene since the heterogeneity of its thermal degradation in solid state has been demonstrated [81,83, 96].

The oxygen diffusion effect is also included by adding the oxygen diffusion term in the expression corresponding to concentration changes of oxygen (Equation 25).

$$\frac{d[O_2]}{dt} = D_{O_2}\left(\frac{\partial^2 [O_2]}{\partial^2 x^2}\right) - k_2 [P^\bullet][O_2] + k_6 [PO_2^\bullet]^2 \qquad (25)$$

The first term in the right corresponds to the Fickian gas diffusion; *x* is the distance from the surface of the sample, D_{O2} is the coefficient of oxygen diffusion in the polymer and $[O_2]$ is the available concentration of oxygen Henry's law:

$$[O_2] = S_{O2} p_{O2} \qquad (26)$$

where S_{O2} is the solubility coefficient of oxygen in the polymer (in the amorphous phase) [mol l^{-1} Pa^{-1}] and p_{O2} is the oxygen partial pressure [Pa].

The initial condition regarding the oxygen diffusion is $[O_2] = [O_2]_s$, where $[O_2]_s$ is the initial concentration of the $[O_2]$ specie. $[O_2]_s$ is directly related to the partial pressure of oxygen p_{O2} calculated by the Henry's Law (Equation 26)

The *CLM* input is completed by adding an extra condition related to the oxygen diffusion: at any time, $[O_2] = [O_2]_s$ for $x = -\frac{L}{2}$ and $x = \frac{L}{2}$, the origin of depth coordinates is the middle of the sample (*L*).

As a conclusion, in order to solve the system seven rate constants (k_{1u}, k_{1b}, k_2, k_3, k_4, k_5, k_6), two physical characteristics associated to a coefficient of the polymer (S_{O2}, D_{O2} ,three initial conditions ($[POOH]_0$, $[PH]_0$, $[O_2]_s$,) and the exposure conditions given by p_{O2} value are required.

2.9. Application of the CLM in the Study of the Composite Degradation

The clay nanocomposites studied in this work have polyethylene and polypropylene matrices. Therefore, as a first approach to modeling their degradation behavior and determining their lifetime using a non empiric method, studies performed on the plain *PP* and *PE* polymers are used as references.

For being semi-crystalline polymers, polypropylene and polyethylene present degradation process only in their amorphous phase since their crystalline phase is inert of oxygen permeation. They can be studied as homogeneous materials where average values of oxidation products can be calculated in function of the crystallinity fraction by adding a correction factor related to the crystalline proportion. Comparing the behavior of *PP* and *PE* towards degradation, it is noticeably that polypropylene is much more sensitive than polyethylene: its tertiary CH is highly reactive and promotes faster reactions of hydrogen subtraction [97].

Figure 10 represents a kinetic curve displaying the typical behavior of a material during oxidation. In this curve (based on experimental data from measurements of carbonyl concentration or oxygen absorption) two main stages can be distinguished: the first one, corresponding to the induction period during carbonyl growth, is autoaccelerated. This stage can also be associated (in stabilized polymers) to the time where thermal stabilizers are completely consumed. The end of this stage is related to the induction time (t_i). In the second region, the steady state rate (r_s) can be calculated because at this stage carbonyl is being produced at a constant rate.

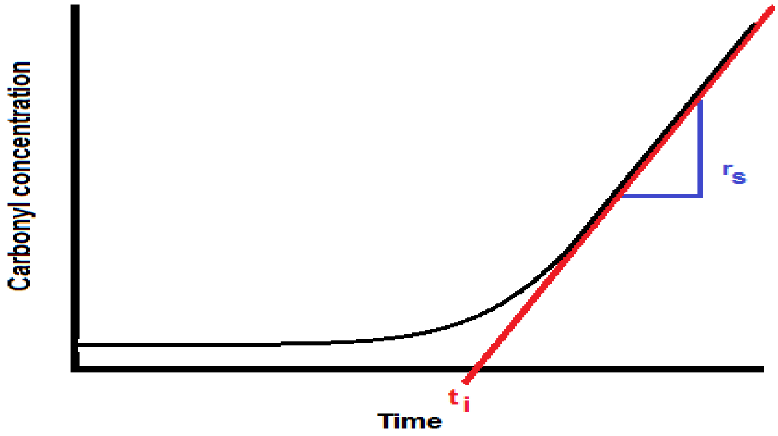

Figure 10 Scheme of an autoaccelerated curve of thermal degradation of a polymer

There is one additional region of the curve (not illustrated in figure 10) that corresponds to the complete consumption of the substrate in which the speed of carbonyl production is equal to zero. Due to important weight lost during this last step experimental measurements are not representative of the oxidation kinetics [86].

Regarding the application of a *CLM* to the study of thermal oxidation of polypropylene at low and moderated temperatures two works can be mentioned:

Rincon-Rubio et al [85] studied thermal-oxidation of a non-stabilized polypropylene at temperatures ranked between 80°C and 150°C under an oxygenated environment. Realistic estimations of the lifetime values and a good description of the hydroperoxide concentration and oxygen consumption were obtained. Besides the kinetic study, they indicated that thermal degradation became oxygen diffusion limited in samples with thickness between 10 and 100μm. The oxygen diffusion limitations and its coupling with the thermo-oxidation process were studied through a combination of experimental and modeling approaches: Fourier transmission infra-red (*FTIR*) measurements of the oxidation products in the transverse direction of the sample all the 35 μm-thick were done in order to built up the profiles of the oxidation products. Such results were compared with the *CLM* simulations when adding equations that govern the oxygen diffusion. The modeling results were in a reasonable good agreement with experimental profiles and provided an estimation of their shape in the same order of magnitude that the experimental results.

Finally, they provided an order of magnitude for kinetic constants in a temperature range of 80°C to 150°C:

k_1 = $10^1 – 10^{-4}$ s^{-1} k_2 = 10^{10}-10^{11} $cm^3mol^{-1}s^{-1}$ k_3 = 10^3-10^9 $cm^3mol^{-1}s^{-1}$

k_4 =10^{10}-10^{11} $cm^3mol^{-1}s^{-1}$ k_5 =10^9-10^{10} $cm^3mol^{-1}s^{-1}$ k_6=10^6-10^7 $cm^3mol^{-1}s^{-1}$

Richaud et al [73] studied the effect of oxygen pressure on unstabilized polypropylene at 80°C in order to simulate its thermo-oxidative behavior and asses the values of the kinetic constants for the *CLM*. They used an inverse methodology to determinate the values of the kinetic constants by fitting simulated curves to experimental results. Such study comprehends a fist stage where there is an excess of oxygen: k_1 and $\frac{k_3^2}{k_6}$ were established. Rate constants k_4, k_5 were assessed through a second step which considers the oxygen diffusion. They presented the values of a complete set of kinetic constants including $[PH]_0$=20 mol l^{-1}, k_{1u}, and k_{1b}:

	k_{1u} [s^{-1}]	k_{1b} [$lmol^{-1}s^{-1}$]	k_2 [$lmol^{-1}s^{-1}$]	k_3 [$lmol^{-1}s^{-1}$]	k_4 [$lmol^{-1}s^{-1}$]	k_5 [$lmol^{-1}s^{-1}$]	k_6 [$lmol^{-1}s^{-1}$]
k_i at 80°C	2.0 10^{-8}	1.0 10^{-5}	1.2 10^{7}	2.5 10^{-2}	1.0 10^{10}	2.6 10^{9}	3.0 10^{3}
ln k_{i0}	25.5	28.3	17.8	18.4	23.0	21.7	27.4
Ea_i [$kJmol^{-1}$]	135	100	5	60	0	0	60

Table 1. Kinetic parameters for polypropylene modeling at 80°C

In the case of polyethylene, Colin et al [56] demonstrated a quasi-universal behavior of the thermo-oxidation of polyethylene pointing to a bimolecular decomposition of $POOH$ as main initiation reaction regardless branching, crystallinity and other structural irregularities. Consequently, a full list of rate constants, pre-exponential factors and activation energies was provided in order to calculate the values of all speed constants at different temperatures as $k_i = k_{io} \exp\left(\frac{-E_{ai}}{RT}\right)$. Additionally, they used $[PH]_0$=60 mol l^{-1} as a valid condition to run the kinetic model for polyethylene.

Rate constant, k_i [s^{-1} or $lmol^{-1}s^{-1}$]	Pre-exponential factor, k_{io} [s^{-1} or $lmol^{-1}s^{-1}$]	Activation Energy, E_{ai}[$kJmol^{-1}$]
k_{1u}	$2.0\ 10^{12}$	145
k_{1b}	$1.9\ 10^{7}$	86
k_2	10^{8}	0
k_3	$1.5\ 10^{10}$	73
k_6	$5.6\ 10^{8}$	0

Table 2. Parameters for kinetic modeling of polyethylene

Later, Colin et al [103] published another work regarding thermal oxidation of un-stabilized polyethylene under air atmosphere at 100°C presenting a comparison between experimental and simulation oxidation profiles. A good fit was reached by using $[PH]_0$ =60 mol l^{-1} and:

k_{1u} [s^{-1}]	k_{1b} [$lmol^{-1}s^{-1}$]	k_2 [$lmol^{-1}s^{-1}$]	k_3 [$lmol^{-1}s^{-1}$]	k_4 [$lmol^{-1}s^{-1}$]	k_5 [$lmol^{-1}s^{-1}$]	k_6 [$lmol^{-1}s^{-1}$]
$1\ 10^{-8}$	$1.5\ 10^{-5}$	10^{8}	$9.1\ 10^{-1}$	$8\ 10^{11}$	$2.3\ 10^{11}$	$5.6\ 10^{8}$

Table 3 Complete set of kinetic parameters for polyethylene at 100°C

The publication of works on the study of degradation process of composite materials by non empiric methods is scarce. Some research has been done considering conventional composites of carbon fibers in a thermoset matrix of bismaleimide [104] and amine crosslinked epoxy [105].

Several studies related to the thermal stability of nanocomposites and especially clay nanocomposites having a polyolefin matrix are available in literature (Zanetti et al, 2004, Dintcheva at al, 2007, Lomakin et al, 2008, Golebiewski et al, 2007, Bertini et al, 2006, Gilman J et al, 1999) [65,68,106,107,108,109], however all of them were performed by applying empiric methods of analysis.

This situation rests valid in the case of photo-oxidation degradation however, it was possible to identify the main issues of the montmorillonite on photo-oxidation kinetics of the clay nanocomposites: Mailhot et al [110] reported that the montmorillonite influences the degradation of polypropylene by slightly speeding up its oxidation rate. Morlat S et al [111] found also an increase of oxidation rate and pointed that in presence of the montmorillonite there is an important reduction and sometimes the complete disparition of the induction period.

Furthermore, they suggested that the presence of the ions Fe^{+2} and Fe^{+3} (impurities of the *MMT*) may play a role in the degradation mechanism of the polypropylene clay nanocomposites by inducing a higher sensitivity toward degradation. Qin H. et al [112,113] noticed same acceleration effect of the degradation when the clay is present and added that photo-oxidation process is barely affected by the dispersion of the montmorillonite in a polypropylene and in a polyethylene matrix. Finally, Bottino et al [114], presented experimental evidence that contradicted this last hypothesis regarding the nanocomposite morphology: they suggested that exfoliation of clay sheets favors access to catalytic sites initially “hided” in the gallery space where metal ions are initially contained. Such discussion is still open.

To our knowledge, no studies applying the *CLM* observing thermo-oxidation or photo-oxidation of nanocomposites have been reported.

The aim of this work is to apply a non-empiric method of analysis to study the thermo-oxidation process of clay nanocomposites with unstabilized polyolefin matrix under low and moderated temperature conditions between 60°C and 100°C. The specific goal is to clarify the consequences of the montmorillonite presence during the thermal oxidation process, and particularly its effects over the oxidation kinetics of polypropylene and polyethylene matrixes. This point will be closely related to the chemical activity (represented by a catalytic effect) showed by the montmorillonite and which might potentially affect the kinetic mechanism of the pure polyolefin.

Furthermore, special attention is given to the elucidation of the effects related to the physical role played by the montmorillonite clay *vis-à-vis* the oxygen diffusion. These oxygen diffusion limitations turn a homogeneous process into a heterogeneous degradation when strong gradients on the distribution of the oxidation products are present.

References

1 Tabtiang A, Venables R. The performance of selected unsaturated coatings for calcium carbonate filler in polypropylene. European Polymer Journal 2000; 36: 137- 148.

2 Chatterjee A., Deopura B.L, High modulus and high strength PP nanocomposite filament. Composites: Part A. 37. 2006: 813–817.

3 Fina A, Abbenhuis H.C.L., Tabuani D. Frache, A., Camino G. Polypropylene metal functionalized POSS nanocomposites: A study by thermogravimetric analysis. Polymer Degradation and Stability 2006; 91: 1064-1070.

4 Fukushima H, Drzal LT, Rook BP, and Rich M.J. Thermal conductivity of exfoliated graphite nanocomposites. Journal of Thermal Analysis and Calorimetry, 2006: 1: 235–238.

5 Horch A, Shahid N,Mistry A, Timmer M.D, Mikos A.G, Barron A . R, Nanoreinforcement of Poly(propylene fumarate)-Based Networks with Surface Modified Alumoxane Nanoparticles for Bone Tissue Engineering. Biomacromolecules 2004, 5, 1990-1998.

6 Segard E, Benmedakhene S, Laksimi A, Lai D. Influence de l'interface fibre/matrice sur le comportement jusqu``a rupture d'un polypropylène renforcé de fibres de verre courtes. Mécanique & Industries. 2005; 6: 479–486.

7 Bocchini S. Morlat-Therias S., Gardette J.L, Camino G. Influence of nanodispersed hydrotalcite on polypropylene photooxidation. European Polymer Journal 2008; 44: 3473-3481.

8 Aloisi G.G, Costantino U, Latterini L., Nocchetti M. , Camino G., Frache A., Preparation and spectroscopic characterization of intercalation products of clay and of clay–polypropylene composites with rhodamine B. Journal of Physics and Chemistry of Solids 2006 ; 67 : 909–914.

9 Jayaraman K, Kumar S. Polymer nanocomposites. Chapter 4: Polypropylene layered silicate nanocomposites. 130-150. Edited by Mai Y-W and Yu Z-Z. Woodhead Publishing Limited and CRC Press LLC Reprinted 2007. Boca Raton.

10 Meniska D, Vaculikl J, Kalendova A, Kristkova M, Simonik J.. Properties of polypropylene nanocomposite prepared by different way of compounding. ANTEC 2003; 2744- 2750.

11 Shina Ray S, Okamoto M. Polymer /layered silicate nanocomposites: a review from preparation to processing. Prog. Polym. Sci. 2003; 28: 1539-1642.

12 Brachet P, Høydal L.T, Hinrichsen E.L, Melum F. Modification of mechanical properties of recycled polypropylene from post-consumer containers. Waste Management 2008; 28: 456–2464.

13 Kadota M, Cakmak M, Hamada H. 1999 - Structural hierarchy developed in co-injection molded polystyrene polypropylene parts. Polymer1999; 40: 3119–3145.

---

14 Richaud E , Farcas F, Divet L, Benneton J.P. Accelerated ageing of polypropylene geotextiles, the effect of temperatures, oxygen pressure and aqueous media on fibers-Methodological aspects. Geotextiles and Geomembranes. 2008; 26 : 71–81.

15 Lotti C, Correa Carlos A., Canevarolo Sebastião V. “Mechanical and Morphological Characterization of Polypropylene Toughened with Olefinic Elastomer” Departamento de Engenharia de Materiais, Universidade Federal de São Carlos, São Carlos - SP, Brazil. Materials Research, Vol. 3, No. 2, 37-44, 2000.

16 Yayla P, Bilgin Y. Squeeze-off polyethylene pressure pipes: Experimental Analysis. Polymer Testing 2007; 26: 132–141.

17 Garcia R.E, Suarez B. M. Clays: Propiedades y usos. 2002. Universidad Complutense. Universidad de Salamanca.Notas de clase .

18 Alexandre M, Dubois P. Polymer-layered silicate nanocomposites: preparation, properties and uses of a new class of materials. Materials Science and Engineering 2000; 28: 1-63.

19 Vaia R, Giannelis E. Polymer Melt Intercalation in Organically-Modified Layered Silicates: Model Predictions and Experiment. Macromolecules 1997; 30: 8000-8009.

20 Garcia D, Picazo O, Merino J.C., Pastor J.M. European Polymer Journal 2003; 39: 945–950.

21 Okada A, Kawasumi M, Usuki A, Kojima Y, Kurauchi T, Kamigaito O. Synthesis and properties of nylon-6/clay hybrids. Polymer based molecular composites. MRS Symposium Proceedings. Pittsburgh 1990; 171: 45–50.

22 Giannelis E. Layered Silicate Nanocomposites. Adv. Mater. Polymer .1996;8: 29- 35

23 Wu C, Zhang M, Rong M, Lehmann B and Friedrich K. Functionalisation of polypropylene by solidphase graft polymerization and its effect on mechanical properties of silica nanocomposites. Plastics, Rubbers and Composites 2004; 33: 71-76.

24 Hambir S, Bulakh H, Jog J.P. Polymer Engineering and Science 2002; 42: 1800-1807.

25 Shina Ray S, Bousmina M. Biodegradable Polymers and their layered silicate nanocomposites: In greening the 21st century material world. Progress in Material Science 2005; 50:962-1079.

26 Usuki A, Hasegawa N, Kato M. Polymer-Clay Nanocomposites. Adv Polym Sci 2005; 179: 135–195.

27 Greeland D.J. Adsorption of poly(vinyl alcohols) by Montmorillonite. J Colloid Sci 1963; 18:647–64.

28 Jeon H.G, Jung H.T, Lee S.W, Hudson S.D. Morphology of polymer silicate Nanocomposites. High density polyethylene and a nitrile. Polym Bull 1998;41:107–13

29 Kawasumi M, Hasegawa N, Usuki A, Okada A. Nematic liquid crystal/clay mineral composites. Mater Sci Engng C. 1998; 6:135–43

30 Gilman J.W, Harris R. Jr. Cyanate ester clay nanocomposites: Synthesis and flammability studies. Evolving and Revolutionary Technologies for the New Millennium. International SAMPE Symposium/Exhibition, 44th. Society for the Advancement of Material and Process Engineering (SAMPE). Long Beach, CA. May 1999: 1408-1423.

31 Doh J.G, Cho I. Synthesis and properties of polystyrene-organoammonium montmorillonite hybrid, Polym. Bull. 1998; 41: 511- 517.

32 Swain S, Isayev A. Effect of ultrasound on HDPE/clay nanocomposites: Rheology, structure and properties. Polymer. 2007; 48: 281-289.

33 Zhu, J.; Morgan, A. B.; Lamellas, F.; Wilkie, C. A. Chem Mater, 2001, 13, 4649.

34 Davis C, Mathias L.J, Gilman J, Schiraldi D.A, Shields J.R, Trulove P, Sutto T, Delong H. Effects of Melt-Processing Conditions on the Quality of Poly(ethylene terephthalate) Montmorillonite Clay Nanocomposites. Journal of Polymer Science: Part B: Polymer Physics, 2002; 40: 2661–2666.

35 Morgan A.B, Gilman J.W. Characterization of Polymer-Layered Silicate (Clay) Nanocomposites by Transmission electron Microscopy and X-Ray Diffraction: A Comparative Study. Journal of Polymer Applied Science. 2003; 87: 1329-1338.

36 Benetti E, Causin V, Marega C, Marigo A, Ferrara G, Ferraro A, Consalvi M, Fantinel F. Morphological and structural characterization of polypropylene based nanocomposites. Polymer 2005; 46: 8275–8285.

37 Liu L, Qi Z, Zhu X. Studies on Nylon 6/Clay Nanocomposites by Melt-Intercalation Process. Journal of Applied Polymer Science. 1999; 71 1133–1138.

38 Reichert P, Hoffmann B, Bock T, Thomann R, Mulhaupt R, Friedrich C. Morphological Stability of Poly(propylene) Nanocomposites. Macromol. Rapid Commun. 2001; 22, 519–523.

39 Cole K, Perrin-Sarazin F, Dorval-Douville G. Infrared Spectroscopic Characterization of Polymer and Clay Platelet Orientation in Blown Films Based on Polypropylene-Clay Nanocomposite. Macromol. Symp. 2005, 230, 1–10.

40 VanderHart D.L, Asano A, Gilman J.W. NMR measurements related to clay dispersion quality and organic- modifier stability in nylon 6/clay nanocomposites. Macromolecules 2001; 34: 3819-3822.

41 Galgali G, Agarwal S, Lele A . Effect of clay orientation on the tensile modulus of polypropylene–nanoclay composites; Polymer. 2004; 45: 6059–6069.

42 Koo C.M, Kim J.H, Wang K.H, Chung I.J. Melt-Extensional Properties and Orientation Behaviors of Polypropylene-Layered Silicate Nanocomposites. Journal of Polymer Science: Part B: Polymer Physics. 2005; 43: 158–167.

43 Ciardelli F, Coiai S, Passaglia E, Pucci A and Ruggeri G. Review Nanocomposites based on polyolefins and functional thermoplastic materials. Polym Int. 2000; 57: 805–836.

---

44 Tidjani A, Wilkie C. Photo-oxidation of polymeric-inorganic nanocomposites: chemical, thermal stability and fire retardancy investigations. Polymer Degradation and Stability.2001 ; 74 :33–37.

45 Choudalakis G, Gotsis A.D. Permeability of polymer/clay nanocomposites: A review. European Polymer Journal. 2009 ; 45 967–984.

46 Compañ Vicente, Del Castillo L.F, Hernandez S.I, Mar Lopez-Gonzalez M, Riande Evaristo. Crystallinity Effect on the gas Transport in Semicrystalline Coextruded Films Based on Linear Low Density Polyethylene. Journal of Polymer Science: Part B: Polymer Physics. 2010.48: 634-642.

47 Fender A, Villanueva M.P, Gimenez E, Lagaron J.M. Characterization of the barrier properties of composites of HDPE and purified cellulose fibers. Cellulose. 2007 ; 14:427–438.

48 Nazarenko S. Meneghetti P, Julmon P, Olson B.G, Qutubuddin S. Gas Barrier of Polystyrene Montmorillonite Clay Nanocomposites: Effect of Mineral Layer Aggregation. Journal of Polymer Science: Part B: Polymer Physics. 2007. 45:1733–1753.

49 Bharadwaj R.K, Mehrabi A. R, Hamilton C, Trujillo C, Murga M,Fan R, Chavira A, Thompson A.K. Structure-property relationships in cross-linked polyester-clay nanocomposites. Polymer. 2002. 43: 3699-3705.

50 Matayabas J, Turner S. In polymer Clay Nanocomposites.2001.Ed. Willey. New York. p:207.

51 Golebiewski J, Galeski A. Thermal stability of nanoclay polypropylene composites by simultaneous DSC and TGA. Composites Science and Technology. 2007; 67: 3442- 3447.

52 Mirzadeh A, Kokabi M. The effect of composition and draw-down ratio on morphology and oxygen permeability of polypropylene nanocomposite blown films.European Polymer Journal. 2007; 43:3757–3765.

53 Stoeffler K, Lafleur P.G, Denault J. The Effect of Clay Dispersion on the Properties of LLDPE/LLDPE-g-MAH/Montmorillonite Nanocomposites. Polymer Engineering Science. 2008 : 2459- 2473.

54 Zhong Y, Janes D, Zheng Y, Hetzer M, De Kee D. Mechanical and Oxygen Barrier Properties of Organoclay-Polyethylene Nanocomposite Films. Polymer Engineering Science. 2007 : 1101- 1107.

55 Cussler EL, Huges SE, Ward WJ, Aris R. Barrier Membranes. Journal of Membrane Scicnce. 1988. 38 : 161- 174.

56 Colin X, Fayolle B, Audoin L, Verdu J. Vieillissement thermo-oxydant des polymères. Un pas vers la modélisation cinétique. Vieillissement et durabilité des matériaux, chapter 3, Lavoiser Tec&Doc, Jun 2003.

57 Verdu J. Vieillissement des plastiques. Edited by Association Française de Normalisation AFNOR .1984. France.

---

58 Fayolle B, Richaud E, Verdu J, Farcas F. Embrittlement of polypropylene fiber during thermal oxidation. J. Mater Sci; 2008; 43: 1026 – 1032.

59 Fayolle B, Colin X, Audouin L, Verdu J. Relating kinetic models to embrittlement in polymer oxidative aging. Polymer Degradation and Performance. American Chemical Society ACS Symposium Series .2009; vol 1004: chapter 12 : 135-146..

60 Jayantha A. Epaarachchi, Philip D. Clausen. An empirical model for fatigue behavior prediction of glass fibre-reinforced plastic composites for various stress ratios and test frequencies. Composites: Part A. 2003; 34:313–326.

61 Christensen R. M. Restrictions on life-prediction methodology in polymers. Mechanics Research Communications. 1982; 9(4): 241-250.

62 Le Huy M, Evrard G. Methodologies for lifetime predictions of rubber using Arrhenius and WLF models. Die Angewandte Makromolekulare Chemie 1998. 261/262: 135–142.

.

63 Celina M, Gillen K.T, Assink R.A. Accelerated aging and lifetime prediction: Review of non-Arrhenius behavior due to two competing processes. Polymer Degradation and Stability. 2005; 90: 395-404.

64 Zanetti M., Camino G, Thomann R, MuÈlhaupt R. Synthesis and thermal behavior of layered silicate / EVA nanocomposites. Polymer. 2001; 42: 4501-4507.

65 Bertini F. Characterization and thermal degradation of polypropylene montmorillonite nanocomposites. Polymer Degradation and Stability. 2006; 91 : 600- 605.

66 Qin H, Zhang S, Zhao C, Feng M, Yang M, Shu Z, Sang S. Thermal stability and flammability of polypropylene/montmorillonite composites. Polym Degrad Stab 2004; 85: 807- 813.

67 Minkova L, Peneva Y. Tashev E. Filippi, S, Pracella, M., Magagnini P. Thermal properties and microhardness of HDPE/clay nanocomposites compatibilized by different functionalized polyethylenes. Polymer Testing 2009; 28: 528–533.

68 Lomakin S, Novokshonova L, Brevnov P, Shchegolikhin A. Thermal properties of polyethylene/montmorillonite nanocomposites prepared by intercalative polymerization. J Mater Sci .2008; 43:1340–1353.

69 Lomakin S, Dubnikova I, Berezina S, Zaikov G. Kinetic study of polypropylene nanocomposite thermo-oxidative degradation. Polym Int . 2005; 54:999–1006.

70 Bourbigot S, Gilman J, Wilkie C. Kinetic analysis of the thermal degradation of polystyrene-montmorillonite nanocomposite. Polymer Degradation and Stability. 2004; 84: 483 – 492.

71 Opfermann J. Kinetic Analysis Using Multivariate Non-Linear Regression. I. Basic concepts. Journal of Thermal Analysis and Calorimetry. 2000; 60:641-658.

72 Fayolle B. Fragilisation des polymères induite par dégradation. Aspects cinétiques. Habilitation à Diriger des Recherches. Arts et Métiers ParisTech. 2009. France.

---

73 Richaud E. Durabilité des géotexiles en polypropylène. PhD Thesis, Ecole Nationale Supérieure d’Arts et Métiers - Centre de Paris, 2006.

74 Gugumus F. Effect of temperature on the lifetime of stabilized and unstabilized PP films. Polym Degrad Stab .1999;63: 41 – 52

75 Richters P. Initiation process in the oxidation of polypropylene. Macromolecules 1970;3:262- 264

76 Gijsman P, Hennekens J, Vincent J. The influence of temperature and catalyst residues on the degradation of unstabilized polypropylene. Polym Degrad Stab 1993;39:271-277

77 Gillen K, Bernstein R, Celina M. Non-Arrhenius behavior for oxidative degradation of chlorosulfonated polyethylene materials. Polymer Degradation and Stability. 2005; 87: 335 - 346

78 Bolland J. L. Kinetic Studies in the Chemistry of Rubber and Related Materials. I. The Thermal Oxidation of Ethyl Linoleate. Proceedings of the Royal Society of London. Series A, Mathematical and Physical Sciences. 1946; vol 186, 1005: 218-236.

79 Bateman L, Gee G. A Kinetic Investigation of the Photochemical Oxidation of Certain Non-Conjugated Olefins. 1948. Proceedings of the Royal Society of London. Series A, Mathematical and Physical Sciences. Vol. 195, No. 1042:376-391.

80 Gillen K, Wise J, Clough R. General solution for the basic Autoxidation Scheme. Polymer Degradation and Stability. 1995; 47: 149-161.

81 Audouin L, Guerguen V, Tcharkhtchi A, Verdu J. “ Closed Loop” Mechanistic schemes for hydrocarbon polymer oxidation. Polym. Chem. 1995; 33:921-927.

82 Verdu S, Verdu J. A New Kinetic Model for polypropylene Thermal Oxidation at Moderate Temperatures. Macromolecules. 1997; 30: 2262-2267.

83 Achimsky L, Audouin L, Verdu J, Rychla L, Rychly J. The effect of oxygen pressure on the rate of polypropylene oxidation determined by chemiluminescence. European Polymer Journal. 1999; 35: 557-563.

84 Colin X, Marais C, Verdu J. A new method for predicting the thermal oxidation of thermoset matrices Application to an amine crosslinked epoxy. Polymer Testing. 2001; 20: 795–803.

85 Rincon-Rubio L.M, Fayolle B, Audouin L, Verdu J. A General solution of the closed-loop model kinetic scheme for the thermal oxidation of polypropylene. 2001. Polymer Degradation and Stability. 2001; 74: 177-188.

86 Achimsky L, Audouin L, Verdu J, Rychla L, Rychly J. On a transition at 80°C in polypropylene oxidation kinetics. Polymer Degradation and Stability. 1997; 58: 283-289.

87 Kamiya Y, Niki E, 1978. Aspects of degradation and stabilization of polymers. Chapter 3. 1978. Elsevier Scientific Publishing Company. Jelling Editor. Asterdam.

88 Howard J. A, Ingol K.U. Absolute rate constants for hydrocarbon autoxidation. VI. Alkyl aromatic and olefinic hydrocarbons. Canadian Journal of Chemistry. 1967; 45: 793 -802.

89 George G, Celina M. Homogeneous and heterogeneous oxidation of polypropylene. Handbook of polymer degradation. 2nd ed. In: Hamid SH, editor. New York: Marcel Dekker; 2000: 277–313.

90 Morlat-Therias S, Mailhot B, Gardette JL, Da Silva C, Haidar B, Vidal A. Photooxidation of ethylene-propylene-diene/montmorillonite Nanocomposites. Polymer Degradation and Stability.2005; 90: 78-85.

91 Philippart JL, Posada F, Gardette JL. Mass spectroscopy analysis of volatile photoproducts in photooxidation of polypropylene. Polymer Degradation and Stability.1995; 49: 285-290.

92 Rivaton A, Gardette JL, Mailhot B, Morlat-Therias S. Basic aspects of polymer degradation. Macromol. Symp. 2005; 225: 129- 146.

93 Colin X, Verdu J. Strategy for studying thermal oxidation of organic matrix composites. Composite Science and technology. 2005; 65: 411-419.

94 Celina M, George G. Heterogeneous and homogeneous kinetic analysis of the thermal oxidation of polypropylene. Polymer degradation and Stability. 1995; 50: 89-99.

95 Zlatkevich L. Chemiluminiscence and oxidation of polypropylene: comments on the hetereogeneous model. Polymer Degradation and Stability. 1995; 50: 83-87.

96 Girois S, Delprat P, Audouin L, Verdu J. Oxidation thickness profiles during photooxidation of non-photostabilized polypropylene. Polymer Degradation and Stab. 1997; 56:169-177.

97 Gugumus F. Thermooxidative degradation of polyolefins in the solid state. Part 2: Homogeneous and heterogeneous aspects of thermal oxidation. Polymer Deg and Stab. 1996; 52 145-157.

98 Fairgrieve S.P, Maccallum J. R. Diffusion-controlled oxidation of polymers: a mathematical model. Polymer degradation and stability. 1985, vol. 11, n^{o}3: 251-265.

99 Kiryushkin S.G, Shlyapnikov Yu.A. Diffusion-controlled polymer oxidation. Polymer Degradation and Stability. 1989; 23:185-192.

100 Guinault Alain. Fabrication de films thermoformables et soudables à hautes propriétés barrières. Conservatoire National des Arts et Métiers. Thèse Doctoral. 2003.

101 Stivala S., Reich L., Kellher P. Kinetics of the thermal oxidation of Isotactic Polypropylene by Infrared Spectroscopy. Makromol. Chem. 1963; 52: 28-42.

102 Cunliffe A.V, David A. Photo-Oxidation of thick polymer samples. Part II: The Influence of oxygen Diffusion on the Natural and Artificial Weathering g of Polyolefins. Polym. Deg. Stab. 1982; 4: 17-37.

---

103 Colin X, Audouin L, Verdu J. Determination of thermal oxidation rate constants by an inverse method. Application to polyethylene. Polymer Degradation and Stability. 2004; 86:309-321.

104 Colin X, Verdu J. Strategy for studying thermal oxidation of organic matrix composites. Composites Science and Technology. 2005; 65: 411–419.

105 Colin X, Marais C, Verdu J. Kinetic modelling of the stabilizing effect of carbon fibres on thermal ageing of thermoset matrix composites. Composites Science and Technology. 2005; 65:117–127.

106 Zanetti M, Bracco P, Costa L. Thermal degradation behaviour of PE/clay nanocomposites. Polymer Degradation and Stability. 2004; 85:657-665.

107 Cussler EL, Huges SE, Ward WJ, Aris R. Barrier Membranes. Journal of Membrane Scicnce. Dintcheva N, La Mantia F. Thermo-Mechanical Degradation of LDPE-Based Nanocomposites. Macromol. Mater. Eng. 2007; 292: 855–862.

108 Golebiewski J, Galeski A. Thermal stability of nanoclay polypropylene composites by simultaneous DSC and TGA. Science and Technology. 2007; 67:3442–3447.

109 Gilman J. Flammability and thermal stability studies of polymer layered-silicate-clay/ nanocomposites. Applied Clay Science. 1999; 15:31–49.

110 Mailhot B, Morlat S, Gardette JL, Boucard S, Duchet J, Gerard JF. Photodegradation of polypropylene nanocomposites. Polymer Degradation and Stability. 2003; 82:163–167.

111 Morlat S, Mailhot B, Gonzales D, Gardette J.L. Photo-oxidation of polypropylene/ montmorillonite nanocomposites. I.Influence of nanoclay and compatibilizing agent. Chem. Mater. 2004: 16(3):377-383.

112 Qin H, Zhao C Zhang S, Chen G, Yang M. Photo-oxidative degradation of polyethylene/montmorillonite nanocomposite. Polymer Degradation and Stability. 2003; 81:497–500.

113 Qin H, Zhang S, Liu H, Xie S, Yang M, Shen D. Photo-oxidative degradation of polypropylene/montmorillonite nanocomposites. Polymer. 2005; 46:3149–3156.

114 Bottino F.A, Di Pasquale G, Fabbri E, Orestano A, Pollicino A. Influence of montmorillonite nano-dispersion on polystyrene photo-oxidation. Polymer Degradation and Stability. 2009; 94 :369–374.

Chapter II

Materials and Methods

Index of Figures

Index of Tables

Résumé Chapitre II

Matériaux et Méthodes expérimentales

Ce chapitre a pour objet de présenter les matériaux de l'étude, les conditions de vieillissement, et les techniques associées au suivi de ce vieillissement.

Le premier nanocomposite étudié dans le chapitre III présente une matrice polypropylène avec un agent de couplage (polypropylène greffé anhydride maléique) alors que le nanocomposite dans le chapitre IV est composé d'une matrice polyéthylène (avec agent de couplage polyéthylène greffé anhydride maléique). Dans les deux cas, on étudiera la matrice seule parallèlement au nanocomposite. La nanocharge est une montmorillonite (*MMT-O*) organiquement modifiée présentant des traces de calcium, sodium et magnésium et 1.13% en poids de fer. Ce dernier élément, on le verra plus tard, est susceptible de jouer un rôle dans les cinétiques d'oxydation du nanocomposite.

Pour l'obtention du nanocomposite, le mélangeage est assuré à l'état fondu avant extrusion. Pour chaque système, les conditions de mise ont été optimisées pour optimiser la dispersion de l'argile dans la matrice.

Dans le cas du nanocoposite *PP* (4.53% d'argile), des films de 75 et 150 µm ont été obtenus par presse à 160°C. Dans le cas du nanocomposite *PE* (6,8% d'argile), des films de 160 µm ont été obtenus par extrusion calandrage.

A l’échelle morphologique, l’état de dispersion de la *MMT –O* a été évaluée par diffraction des rayons *X* (*WAXS*) et par microscopie électronique en transmission (*STEM*).

Avant de réaliser les vieillissements accélérer sous air à 60°C, 80°C et 100°C, les stabilisants des films ont été extraits en soxhlet en présence de solvants. Enfin, l’obtention d’échantillons épais de 1400 µm a été réalisée à partir des films par soudage-pressage à 125°C.

Les outils permettant de suivre le processus d’oxydation ont été :

- La spectrophotométrie infra-rouge en se focalisant sur la bande des carbonyles à 1713 cm^{-1}. La concentration a été déterminée par la loi de Beer-Lambert en prenant un coefficient d’extinction molaire de 300 $l\ mol^{-1}\ cm^{-1}$.
- La micro spectrophotométrie permettant de cartographier une épaisseur d’échantillon, en mode *ATR* dans le cas du nanocomposite *PP* et en transmission dans le cas du nanocomposite *PE*. On notera que la micro spectrophotométrie *ATR* permet d’accéder à des résolutions spatiales de l’ordre de 6 µm.
- Par analyse enthalpie différentielle (*AED*) et par mesure de densité pour caractériser respectivement le taux de cristallinité et le taux de cristallinité apparent respectivement.
- Par chromatographie à exclusion stérique (*CES*) pour suivre la diminution de masses molaires induit par le processus de coupure de chaine.
- Par mesure de perméabilité à l’oxygène (perméamètre) pour accéder au coefficient de diffusion.

Chapter II

Materials and Methods

This chapter shall describe the materials used during this study and the experimental and simulation procedures performed in order to characterize changes occurred during the thermo oxidation process under low and moderated temperatures.

1. Materials

Three kinds of raw materials were used during this work: a polymeric matrix, a montmorillonitic nanofiller, and a coupling agent. Furthermore, through a composition process these materials were mixed with the purpose of obtaining two kinds of clay nanoreinforced polyolefin composites.

1.1. Material Selection

- Polymer matrix

Two polymers belonging to the polyolefin family were selected due to their wide use in industry, especially for packaging applications:

- ✓ Polypropylene: Propilco 01R25 propylene-ethylene copolymer supplied by Propilco. Melt flow index (*MFI)* 0.8 g/10min at 190°C and 2.16kg.

✓ Low density polyethylene: LDPE DOW® 1321 supplied by DOW Chemicals. Melt flow index (*MFI)* 0.22 g/10min at 190°C and 2.16kg.

These materials played the role of a matrix in which nanoclay was incorporated in order to create two sorts of nanocomposites: polypropylene and polyethylene nanocomposite.

- Nano filler

The nanoclay used as filler was Nanofil® SE 3000 supplied by Süd Chemie AG: it is an organically modified montmorillonite with di-tallow di-methyl quaternary ammonium salt. Its specific weight is 1800 kg cm^{-3}. A histogram of the size distribution was obtained as a result of the granulometric analysis performed by laser diffraction in an isopropyl alcohol suspension. (Figure 11). The average particle size (D_{50}) before blending was 8.16 µm. The complete distribution is shown in Table 4.

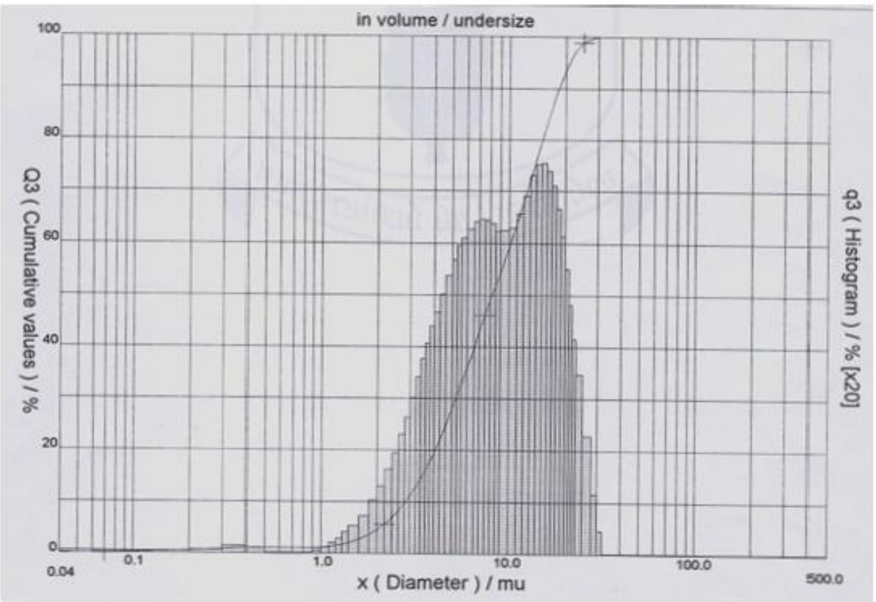

Figure 11. Histogram of the clay size distribution.

D_{10}	2.85µm
D_{50}	8.16µm
D_{90}	18.44µm
D_p (average diameter)	9.58µm

Table 4. Size distribution of the clay *MMT-O*.

A test of inductively coupled plasma mass spectroscopy (*ICP-MS*) was performed in a Vista-Pro ICP analyzer in order to identify traces of elements at present in the clay [115]. Silicium and aluminum represented the vast majority of found components since they are constitutive elements of the clay (Table 5). Traces of calcium, sodium and magnesium ions were also detected even after the organic modification. Finally, among other detected elements the iron quantity was quite significant: 11312 ppm, which is equivalent to 1.1312%w of Fe in the clay. This fact may represent catalytic characteristics of the clay when present in a system during a degradation process.

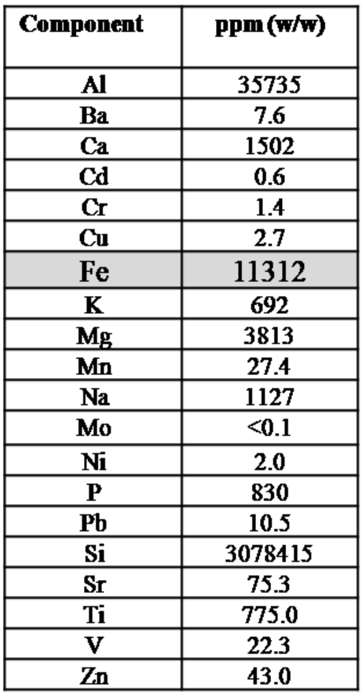

Component	ppm (w/w)
Al	35735
Ba	7.6
Ca	1502
Cd	0.6
Cr	1.4
Cu	2.7
Fe	11312
K	692
Mg	3813
Mn	27.4
Na	1127
Mo	<0.1
Ni	2.0
P	830
Pb	10.5
Si	3078415
Sr	75.3
Ti	775.0
V	22.3
Zn	43.0

Table 5. Quantification of element traces in the organically modified clay

- Coupling Agent

The coupling agent was chosen in function of the composite matrix: for the polypropylene nanocomposite a coupling agent with a polypropylene matrix was selected while for the *LDPE* nanocomposite a coupling agent with a *LDPE* matrix was chosen.

In the polypropylene system the coupling agent used was Polybond® 3200 provided by Cromptom, which has 1%w of maleic anhydride grafted propylene and a melt flow index (*MFI)* equal to 115g/10min. In the *LDPE* system the coupling agent used was OREVAC ® 18370 which is a maleic anhydride polyethylene grafted at 0.25% w/w. It has a relative density of 0.21 and a *MFI* of 2 g/10min.

1.2. Preparation of nanocomposites and testing samples

The composition of the nanocomposite materials was done using the melt state method. For each system the processing conditions were fixed to optimize the clay dispersion on the matrix.

- Polypropylene/coupling agent/montmorillonite

The proportion of *MMT-O* and coupling agent was 4.62%w and 28.5%w, respectively. The remaining 66.88%w represents the proportion of the matrix.

The blending of materials was done with an internal Brabender Plasti-Corder PLE 331 mixer at 200 °C and 90 rpm for 20 minutes. To achieve optimum dispersion, the clay and the coupling agent were incorporated, mixed for 2 minutes, followed by the adding of the polymer matrix. The mixing processing conditions were optimized according to an experimental design. The screw speed varied in order to maximize the exfoliation index which was determined from dynamic shearing tests in the linear viscoelastic domain [116]. The final quantity of montmorillonite present in the clay polypropylene composite was determined by Thermo Gravimetric Analysis (*TGA*) by subtracting the residue of *PP* from *NC.* In average, the quantity of organically modified clay present in the polypropylene matrix was equal to 4.53%w.

The films were then press-molded at 160°C. Pure *PP* and polypropylene nanocomposite films were obtained under the same conditions to ensure a similar preoxidation state. Films with two different thicknesses were obtained: 75 µm and 150µm.

- Polyethylene/coupling agent/montmorillonite

Nanocomposite material was obtained through two steps: a concentrated material was first obtained by mixing 21%w of montmorillonite with 42%w of coupling agent and 37%w of matrix with a TSK 20/400 co-rotating extruder (20 mm diameter, 790mm larger). The pellets were subsequently blended with matrix material with a Brabender Plasti-Corder PLE 331 single screw extruder (19 mm diameter, 25:1) at 30 rpm and under a temperature profile between 170 and 200°C. As a result 160-µm thick casting films were obtained having a final composition of 5.64%w of montmorillonite, 24%w of coupling agent, and 70.36%w *LDPE.*
The final quantity of montmorillonite present in the composite was determined by Thermal Gravimetric Analysis (*TGA*) subtracting the residue of the *PE* from polyethylene clay nanocomposite *PENC*. The average quantity of clay contained in the *PENC* was 6.8%w.
Finally, films about 1400µm-thick were obtained by pressing and molding together several 60-µm thick films at 125°C for 2 minutes.

2. Methods of Characterization

With the aim to study changes of characteristics induced by the clay presence during thermo-oxidation process a dual methodology combining experimental and simulation approaches was used.

2.1. Experimental Methods

In order to study thermal oxidation of unstabilized samples in air atmosphere at 60°C, 80°C and 100°C, stabilizers were extracted with a Soxhlet extractor at 60°C:

- For the polypropylene and its nanocomposites, extraction was done by using a mix of hexane/methanol/chloroform in a proportion of 4/1/1 [117] for 30 hours.
- In the case of the polyethylene and its nanocomposite, acetone was used as solvent and the extraction time was 24 hours. This procedure was performed three times (total time of 72 hours) to assure removal of all thermal stabilizers.

In order to determine the coupling agent influence on the nanocomposite endlife time a study of its thermal degradation kinetics was developed at 60°C, 80°C and 100°C (in the PP case). It was established that by the time the coupling agent carbonyl concentration starts to increase the matrix and the nanocomposite materials have completely finished their degradation process (very brittle and broken samples). Based on these results the coupling agent was not considered as a limiting factor of the nanocomposite lifetime.

Characterization was performed on four different levels: molecular, morphologic, macroscopic and property-scale.

2.1.1. Molecular Scale

2.1.1.1. Fourier Transform InfraRed (*FTIR*)

Aiming to follow the changes induced by oxidation process over time, infrared micro-spectrometry measurements in transmittance were performed. Measurements of the growing of carbonyl bands (*CO*) during thermal oxidation were done with a Brucker IFS 128 spectrometer in transmission mode, with a resolution of 4 cm^{-1} between 400 and 4000 cm^{-1}. Concentration of the carbonyl group was determined from the peak absorbance at 1713 cm^{-1}, characteristic for carboxylic acids [118,119]. For the polypropylene and its composite, absorbance of carbonyl band was calculated between 1700 and 1750 cm^{-1} with a baseline at 1860cm^{-1}. For polyethylene and its composite, the integration limits were 1700 and 1722cm^{-1} using a baseline at 1800cm^{-1}.

According to the Beer-Lambert law, the carbonyl concentration is given by

$$[CO]_{av} = \frac{DO_{co}}{\varepsilon_{1713}\, t} \qquad (1)$$

where $[CO]_{av}$ is the average carbonyl concentration expressed in mol kg^{-1}, DO_{co} is the 1713 cm^{-1} peak absorbance, t is the sample thickness (in cm) and $\varepsilon_{1713} = 300$ l mol^{-1} cm^{-1} is the molar absorptivity.

In the case of the polypropylene and its nanocomposite, the highest average carbonyl concentration studied was fixed to $[CO]_{av}$ = 0.3 mol l^{-1} since samples are highly brittle beyond such value [120]. For polyethylene and its nanocomposite the limit was about $[CO]_{av}$ = 0.4 - 0.5 mol l^{-1}.

2.1.1.2. Micro *ATR/FTIR* Imaging

In order to follow the evolution of the oxidation process over time, infrared micro-spectrometry measurements in transmittance mode are often performed [58,121]. However, its spatial resolution of about 25 to 30 µm does not permit the measurement of thin oxidation layers whose individual thickness is of the order or even lower than the resolution mentioned above, like in the polypropylene and its nanocomposite cases. To enhance lateral resolution, some experimental alternatives appeared such as the use of synchrotron radiation as a source for *FTIR* measurements [122]. By reducing the resolution thanks to the use of high refractive index *ATR* crystals, attenuated total reflectance infrared spectrometry, *ATR-FTIR*, permitted us to follow the extent of oxidation in aged carbon-filled rubbers and polyethylene samples [123,124]. Several recent publications have used this last approach [125,126,127]. Here, we applied this last experimental micro-*ATR-FTIR* approach to assess the oxidation profiles and the thickness of the oxidized layer by using a Perkin-Elmer SpotLight 300 *FTIR* Microscope with Spectrum 100 in *ATR* mode imaging showing spatial resolution of 6 µm.

The oxidation profiles of the samples were measured with a Perkin-Elmer Spectrum SpotLight 300 *ATR-FTIR* microscope. The high refractive index of the germanium crystal (approximately 4) and an effective sample-crystal contact are the physical basis that permits a 6µm spatial resolution [128]. To acquire an image, both the crystal and the attached sample are moved around the surface of the plate whilst the infrared bean scanned different parts of the sample. Spectra were recorded in reflection mode every 1.56 µm which corresponds to the size of the image sample grid. Micro *ATR-FTIR* spectra were collected using two scans per pixel in a wavenumber range between 4000 and 750 cm^{-1}. Samples were coated with MECAPREX MA2 epoxy resin to improve sample handling and prevent the brittle oxidized layer from being torn off. Finally, the samples were polished under water with a 1200 and 2400 polishing paper. Sample preparation is finished by polishing the surface with a Leica EMTXP micro polishing machine using a diamond milling tool. This way sample surface quality is metallographic and parallel to sample base.

Multiple micro *ATR-FTIR* spectra were made in the transverse direction of the resin-*film*-resin samples. To obtain the oxidation profiles, the integration of the absorption values at 1713 cm^{-1} was done along the sample thickness. The measured profiles were corrected using a base line between 1600 and 1850 cm^{-1} and then treated to convert their values from absorbance to concentration units. The relative optic densities were calculated as the ratio between the corrected optic density values on the sample thickness and the corrected absorbance value on the sample surface.

Despite the optimal lateral resolution of the micro *ATR–FTIR* images, the spectra were qualitative.

2.1.1.3. Modulus Profiling

This technique consists in scanning across sample thickness making penetrations with a paraboloidally- shaped tip [129]. Surface deformation data is collected by a computer and then converted into inverted tensile compliance values which globally correspond to elastic modulus of the material. The spatial resolution of this technique is about 50µm [130]. Samples used in this tests needed similar surface preparation that those required for the *ATR*/ *FTIR* imaging test (Section 2.1.1.2).

2.1.1.4. Gel permeation Chromatography (*GPC*)

Determining of the molar mass of the polyethylene and its nanocomposite was done by *GPC* analyses in a 1,2,4-trichlorobenzene (*TBC*) solution at 145°C with a refractive index detector (*RI*). In the case of the nanocomposites, a pre-filtration of the sample was needed in order to preserve the *GPC* columns.

2.1.2. Morphologic Scale

2.1.2.1. Wide Angle X- Ray Diffraction (*WAXS*)

XRD measurements were performed in a Philips X'pert MRD diffractometer employing punctual CuKα radiation at 40mA and 40KV within the scanning angle of 2Θ from 1.5 to 20°. The montmorillonitic clay was first tested in order to characterize the angle 2Θ where its main cleavage plain $\langle 001 \rangle$ was reflected. The nanocomposites were also analyzed to the measure space between clay sheets and to collect information regarding the degree of exfoliation achieved by the clay into the matrix.

2.1.2.2. Scanning Transmission Electronic Microscopy (*STEM*)

In the case of the clay polypropylene nanocomposite, cross sections of films were thinned down below 100nm with a JEOL EM9100IS ion slicer. For the clay nanoreinforced polyethylene, thin cross sections about 50nm were obtained by cryo-ultramicrotomy.

STEM images were obtained by using a JEOL 7400F SEM equipped with a *STEM* accessory at 30 kV for the clay polypropylene and 26kV for the clay polyethylene samples using a sensor to capture retro diffused signals. Several areas were scanned to ensure that the analysis was sample representative.

2.1.2.3. Differential Scanning Calorimetry (*DSC*)

Calorimetric tests were performed in a TA Instruments Differential Scanning Calorimeter Q1000. Thermal analysis consisted in a temperature ramp of 10°C/min going from 30°C to 175°C (after erasing thermal history of the sample). In order to have regularity of sample geometry, tested films were cut with a hole puncher, and their weigh oscillated between 5 and 10 mg.

2.1.2.4. Volumic Mass

Measurements were done with a Mettler Toledo balance at 22°C in water. Polyethylene and clay nanoreinforced film samples were first weighted in air (dry) and once again when completely submerged in water. Density δ can be calculated as follows:

$$\delta = \frac{A}{A-B}\left(\delta_0 - \delta_L\right) + \delta_L \qquad (2)$$

where, A is the weight of the sample in air, B is the weight of the sample in water, δ_0 is the density of water, and δ_L is the density of air (0.0012 gcm^{-3}) [131].

2.1.3. Macroscopic Scale

2.1.3.1. Oxygen Diffusion

For polypropylene and its clay nanoreinforced material, oxygen permeability measurements were performed in collaboration with The Andes University (Colombia) under standard temperature and humidity conditions (23°C, 50 % humidity) with an OX-TRAN Model 2/21 MOCON permeameter, having 5.067 cm^2 of active area.

For polyethylene and polyethylene clay nanocomposite films, permeability measurements were done with a permeameter Systech 8000 having an active area equal to 57.75 cm^2. In order to study the effects caused by the presence of the clay in the system on the oxygen diffusion process several measurements were performed at 7°C, 23°C and 50°C.

Additionally, permeability measurements were done for polyethylene and the nanocomposite films presenting different times of thermal exposition which also allowed measurements of the effects of thermal degradation on the oxygen permeability properties (at 23°C) .

2.2. Simulation Approach

A simulation of thermo–oxidation process was done by using the *CLM* which predicts not only the kinetics curves (for thin samples) at 60°C, 80°C and 100°C, but also the oxidation diffusion limitation effects (at 100°C) manifested as oxidation profiles in the thickness of the samples.

Finally, long term properties of a high conversion degree nanocomposite were explored. The mechanical behavior associated to a pseudo-elastic modulus along the sample thickness was compared to simulated profiles calculated by using a homogenization method.

References

115 Jarvis K.E, Williams J. Laser ablation inductively coupled plasma mass spectrometry (LA-IP-MS): a rapid technique for the direct, quantitative determination of major, trace and rare-earth elements in geological samples. Chemical Geology. 1993; 106: 251-262.

116 Gutiérrez G, Régnier G, Medina J. Exfoliation index as viscoelastic tool to characterize the structure of clay nano-reinforced polypropylenes. Macromolecules Symposyum World Polymer Congress, Rio de Janeiro, Brazil: Wiley-VCH Verlag Gmbh & Co. 2006; 245-246.

117 Zahradnickova A, Sedlar J, Dastych D. Peroxy acids in photo-oxidized polypropylene. Polym Deg Stab. 1991; 32: 155- 176.

118 Gugumus F. Thermooxidative degradation of polyolefins in the solid state: Part 1. Experimental kinetics of functional group formation. Polym Deg Stab.1996: 131-144.

119 Delprat P, Deteurtre X, Gardette JL.Photooxidation of unstabilized and HALS-stabilized polyphasic ethylene-propylene polymers. Polym Deg Stab. 1995; 50: 1-12.

120 Fayolle B, Audouin L, Verdu J, Initial Steps and Embrittlement in the thermal oxidation of stabilized polypropylene films. Polym Deg Stab 2002; 75: 123-129.

121 Cerruti P, Laurinzo P, Malinconio M, Carfagna C. Thermal oxidative stability and effect of water on gas transport and mechanical properties in PA6-EVOH films. J Poly Sci Part B.2007; 45: 840-849.

122 Dumas P, Carr GL, Williams GP. Enhancing the lateral resolution in infrared microspectometry by using synchrotron radiation: applications and perspectives. Analysis 2000; 28, No.1:68-74.

123 Do T, Celina M, Fredericks P. Attenuated total reflectance infrared microspectroscopy of aged carbon –filled rubbers. Polym Deg Stab. 2002; 77: 417-422.

124 Küpper L, Gulmine JV, Janissek PR, Heise HM. Attenuated total reflection infrared spectroscopy for micro-domain analysis of polyethylene samples after accelerated ageing within watering chambers. Vibr Spec. 2004; 34: 63-72.

125 Dhoot G, Auras R, Rubino M, Dolan K, Soto-Valdez H. Determination of eugenol diffusion through LLDPE using FTIR-ATR flow cell and HPLC techniques. Polymer 2009; 50: 1470- 1482.

126 Flemming O, Chan A, Kazarian S. High-pressure CO_2-enhanced polymer interdiffusion and dissolution studied whit in situ FTIR-ATR spectroscopic imaging. Polymer 2006; 47: 4649-4648.

127 Zhou X, Zhang P, Jiang X, Rao G. Influence of maleic anhydride grafted polypropylene on the miscibility of polypropylene/polyamide-6 blends using ATR-FTIR mapping. Vibr Spec 2009; 40:17-21.

---

128 PerkinElmer Ltd. ATR Imaging Accessory User’s Guide. 2006.

129 Kenneth T, Gillen Gillen KT, Clough RL. Polymer Aging Insights Available from Modulus Profiling Data.Polymer Engineering and Science. 1989; 29- 35.

130 Celina M, Wise J, Ottesen DK, Gillen KT, Clough RL. Oxidation profiles of thermally aged nitrile rubber. Polymer Degradation and Stability. 1998; 60: 493 – 504.

131 Mettler-Toledo GmbH. Operating Instructions. 2001.

Chapter III

Clay Nanoreinforced Polypropylene

Index of Figures

Index of Tables

Résumé Chapitre III

Nanocomposite à matrice polypropylène

Dans ce chapitre, on se propose d'étudier l'oxydation du nanocomposite à matrice polypropylène. Parallèlement au nanocomposite et à titre comparatif, l'oxydation de la matrice seule est étudiée dans les mêmes conditions de vieillissement. L'objectif final consiste en la construction d'un modèle cinétique décrivant l'oxydation de deux matériaux, ce modèle étant basé sur un mécanisme d'oxydation du polypropylène.

Après une caractérisation des deux matériaux d'un point de vue physico-chimique, on présente la caractérisation par diffraction des rayons *X* (*WAXS*) et microscopie en transmission (*STEM*) du nanocomposite. Il apparait que l'état de dispersion est de type intercalé/exfolié. Enfin les propriétés de perméabilité des deux matériaux sont comparées avant vieillissement : la présence de *MMT-O* conduit à réduire de 45% les valeurs de perméabilité.

La deuxième partie récapitule l'ensemble des résultats expérimentaux quant au comportement des deux matériaux au cours de leur oxydation à 60°C, 80°C et 100°C. Apres une brève description des modifications induites par l'oxydation (spectrophotométrie infra-rouge), on compare les cinétiques d'oxydation pour mettre en évidence un léger mais significatif influence de la *MMT-O*. En effet, le nanocomposite présente une période d'induction légèrement plus faible indiquant un effet accélérateur de la *MMT-O* sur la cinétique d'oxydation comparativement à la matrice seule. Cette accélération peut être attribuée à un effet catalytique induit par les particules métalliques présentent dans la *MMT-O*.

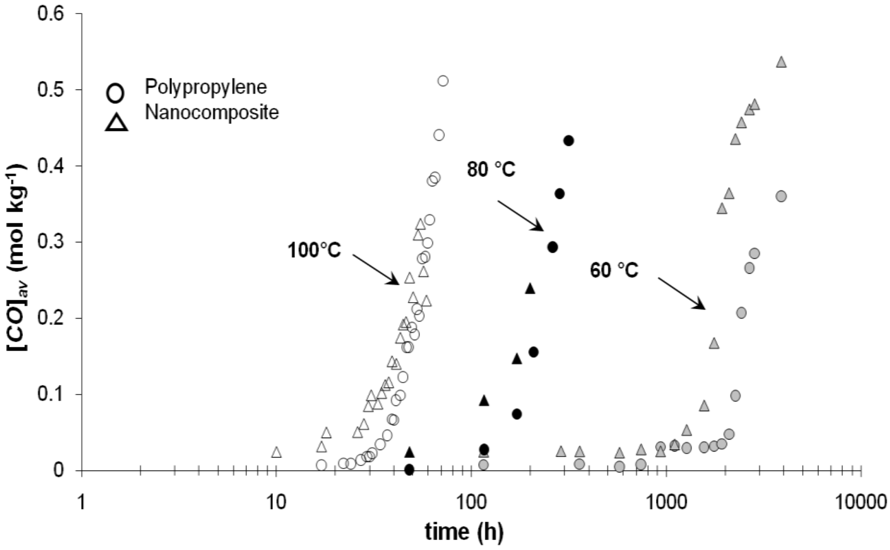

Cinétique d'oxydation du polypropylène et de son composite pour des expositions thermiques à 60°C, 80°C et 100°C.

D'une façon complémentaire à la cinétique d'oxydation, des gradients de produits d'oxydation sont mis en évidence dans l'épaisseur de films de 75 µm par microspectrophotométrie *ATR*. Cette nouvelle technique présentant une résolution spatiale de 6 µm nous permet alors de mesurer ces gradients s'étalant sur 17 µm pour la matrice seule et de 10 µm pour le nanocomposite. Ce résultat inédit permet d'expliquer que la vitesse d'oxydation en pseudo-régime stationnaire des films de 75 µm de nanocomposite est plus faible comparativement à la vitesse des films de matrice seule.

L'ensemble des résultats expérimentaux nous servent comme base afin d'évaluer une modélisation cinétique intégrant le couplage avec la diffusion d'oxygène. Les paramètres de cette modélisation liés à la présence de la MMT sont identifiés par méthode inverse.

Pour modéliser la cinétique d'oxydation du nanocomposite sous forme de film de 75 µm, il est nécessaire de considérer une double influence de la charge sur le processus d'oxydation. D'une part la *MMT-O* peut modifier le mécanisme d'oxydation (effet catalytique lié aux particules métalliques présentes dans la *MMT-O*) et d'autre part la *MMT-O* peut modifier les propriétés physiques et en particulier la valeur du coefficient de diffusion d'oxygène. Une éventuelle diminution de ce dernier va conduire à limiter la couche oxydée sur des épaisseurs plus fines depuis la surface. Pour discuter de ces deux possibilités, on propose donc de modéliser et de tester ces deux hypothèses en utilisant un modèle couplant réaction (d'oxydation) et diffusion (d'oxygène).

Notre modèle cinétique est basé sur le modèle d'oxydation en boucle fermée appliqué au polypropylène. Ce modèle intègre classiquement sept réactions élémentaires dont les constantes de réactions (k_i) ont été proposées dans la thèse d'E. Richaud :

$$POOH \rightarrow 2P^\bullet + H_2O + P=O \qquad (k_{1u})$$

$$2POOH \rightarrow P^\bullet + PO_2^\bullet + H_2O + P=O \qquad (k_{1b})$$

$$P^\bullet + O_2 \rightarrow PO_2^\bullet \qquad (k_2)$$

$$PO_2^\bullet + PH \rightarrow POOH + P^\bullet \qquad (k_3)$$

$$P^\bullet + P^\bullet \rightarrow Inactive\ \ products \qquad (k_4)$$

$$P^\bullet + PO_2^\bullet \rightarrow Inactive\ \ products \qquad (k_5)$$

$$PO^{\bullet}{}_2 + PO^{\bullet}{}_2 \rightarrow Inactive\ \ products \qquad (k_6)$$

La résolution du système d'équations différentielles donne accès alors à l'évolution de toutes les espèces dans le temps et dans l'épaisseur en y ajoutant la loi de Fick liée à la diffusion de l'oxygène :

$$\frac{d[O_2]}{dt} = D_{O_2}\left(\frac{\partial^2[O_2]}{\partial^2 x^2}\right) - k_2[P^{\bullet}][O_2] + k_6[PO_2^{\bullet}]^2 \qquad (1)$$

La concentration en carbonyle est alors égale à :

$$\frac{d[CO]}{dt} = \left[k_{1u}[POOH] + k_{1b}[POOH]^2\right] * [1 - X_c - MMT] * \rho_{PP}{}^{-1} \qquad (2)$$

Avec X_c le taux de cristallinité et *MMT*-O la fraction volumique de charge.

A partir de ce modèle, nous avons simulé, l'ensemble des données expérimentales, à savoir la cinétique de carbonyle et les gradients d'oxydation du nanocomposite (*NC*) et de la matrice seule (*PP*) (voir figure ci-dessous), et ceci, en ne modifiant que les paramètres suivants :

	$[POOH]_0$ (mol kg^{-1})	**MMT-O**	**D_{O_2} à 100°C** (m^2s^{-1})
PP	$1.2\ 10^{-4}$	0	$2.0\ 10^{-12}$
NC	$2.4\ 10^{-4}$	0.1	$1.2\ 10^{-12}$

Paramètres introduits pour la modélisation cinétique du nanocomposite.

Il apparait donc que la présence de *MMT-O* conduit à accélérer l'oxydation se traduisant par une augmentation de la concentration en hydroperoxyde à l'état initial ($[POOH]_0$) regroupant l'ensemble des espèces amorçant l'oxydation et donc les espèces liées aux particules métalliques présentes dans la *MMT-O*, et à diminuer le coefficient de diffusion de l'oxygène (effet barrière).

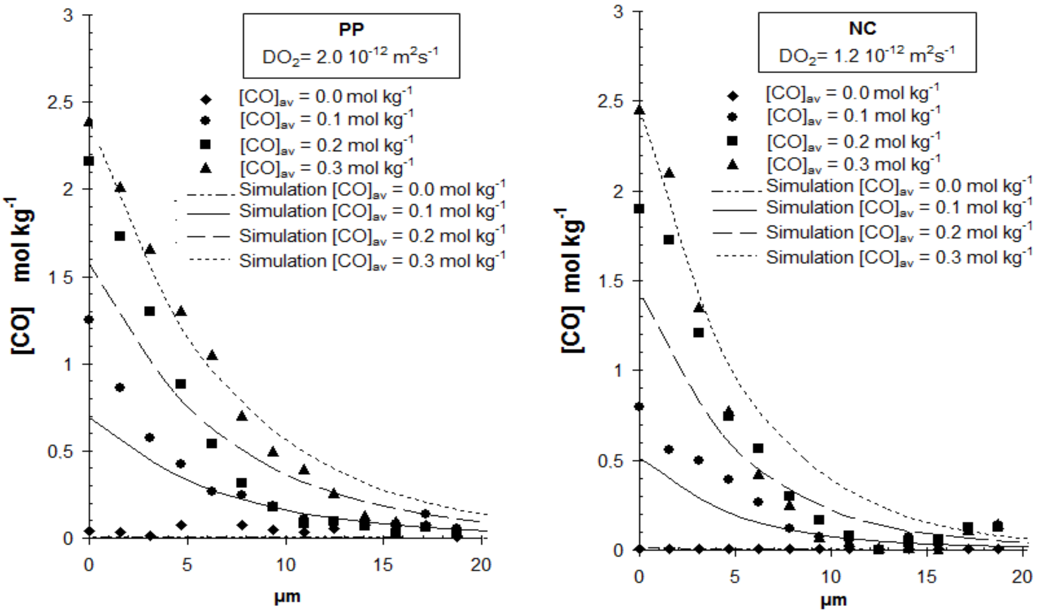

a) **b)**

Comparaison des profils d'oxydation pour des concentration moyennes de carbonyle $[CO]_{av}$ égal à 0.0, 0.1, 0.2, 0.3 et 0.4 mol kg^{-1} mesurés expérimentalement avec les profiles obtenus par la simulation pour a)le pur polypropylène ayant D_{O2PP}: 2.0 10 $^{-12}m^2s^{-1}$ et b) pour son composite *NC avec* D_{O2NC}: 1.2 10^{-12} m^2s^{-1}.

Chapter III

Clay Nanoreinforced Polypropylene

A small number of studies regarding the thermo-oxidation aging kinetics of clay nanofilled *PP* are available, all of them developed at temperatures higher than 250°C, far above the use temperature interval for the use of *PP*. From our knowledge, no studies on the thermo-oxidation mechanisms and kinetics in solid state at moderate temperatures are available in the literature. Scarceness of information regards not only experimental results of the kinetic behavior of polypropylene clay nanocomposites, but also which concerns to a possible application of a general strategy or an analytical methodology for studying degradation of these materials.

Our purpose is to study in an experimental and a theoretical way the thermal oxidation of unstabilized clay polypropylene nanocomposites at moderated temperatures. In order to perform the kinetic modelling of the oxidation process and make predictions of lifetime the Closed Loop Model (*CLM*) was used.

This chapter presents experimental results obtained from studying the kinetic behavior at 60°C, 80°C and 100°C of both unstabilized nanoreinforced and pure polypropylene. Moreover, simulations of the nanocomposite thermal oxidation by applying a kinetic modeling are also included. Finally, *CLM* was used as well in order to explore the influence of the oxygen diffusion coefficient changes on oxidation profiles when oxidation is diffusion controlled. Those lasts results were compared to the data experimentally obtained by micro-*ATR-FTIR* tests.

Finally, just to mention that results obtained from the issue we deal with in Chapter III, gave origin to a paper entitled “Thermal oxidation of clay nano-reinforce polypropylene” recently published in the international journal Polymer Degradation and Stability. The complete reference is: Gutiérrez G, Fayolle B, Réginer G, Medina J. Polymer Degradation and Stability. 2010; 95: 1708 – 1715.

1. Initial Materials Characterization

1.1. Molecular Scale

1.1.1. Fourier Transform Infra Red (*FTIR*)

Five regions may be distinguished in polypropylene spectra: 450–800cm^{-1},900-1300cm^{-1}, 1620-1780cm^{-1},2825 –2970 cm^{-1} and 3200-3650cm^{-1} that respectively correspond to the aliphatic region, the finger print of material, the carbonyl group, the alkanes zone and the hydroxyl group(Figure 12).

An extra peak at 1740 cm^{-1} appears in the spectra when clay is present in the system, due to the presence of saturated aliphatic esters and γ-lactones (1735 – 1750 cm^{-1}) resulting from the coupling agent presence.

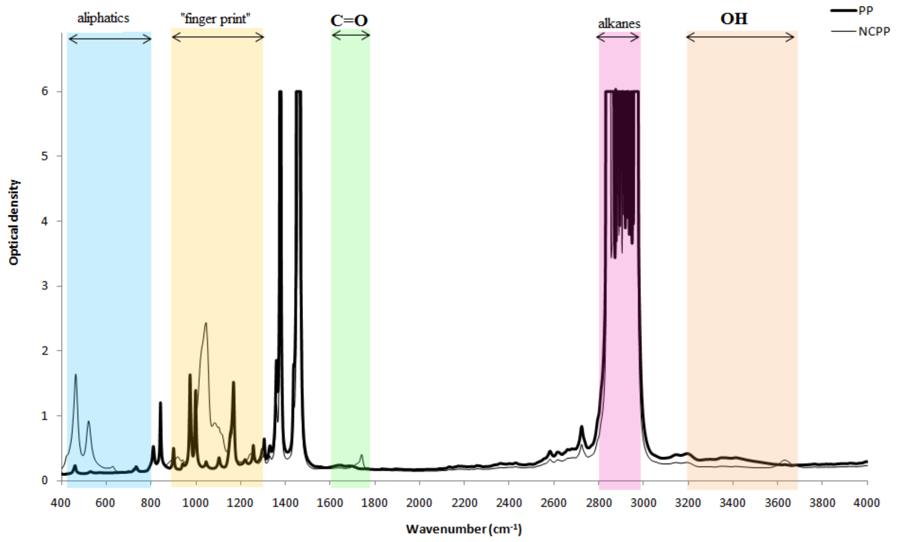

Figure 12 ***FTIR*** **spectra for pure polypropylene and its nanocomposite,** ***NC***

1.2. Morphologic Scale

1.2.1. Wide Angle X- Ray Diffraction (*WAXS*)

WAXS analyses were performed to characterize morphology of the nanocomposite. First of all, to assess if the proportion of ethylene in the composite was relevant, presence of the beta phase peaks corresponding to ethylene crystalline structures was verified. Characteristic peaks of the polypropylene crystalline phase are shown in Table 6.

Phase	Miller Index	Cupper Kα 2θ (°)
α	(110)	14.0
β	(300)	16.0
α	(040)	16.8
α	(130)	18.4
α	(111)	21.2
	(131)	21.7
	(041)	21.8

Table 6 Miller Index for polypropylene crystalline phase.

Only the characteristic alpha phase peaks corresponding to crystalline *PP* were present at 14.04° (Miller index 110) and 16.9° (Miller index 040). There was no peak at 16° corresponding to beta phase, meaning that the quantity of beta phase present in the composite was under the sensitivity limit (Figure 13). A volumic crystallinity close to 0.5 was measured for both materials.

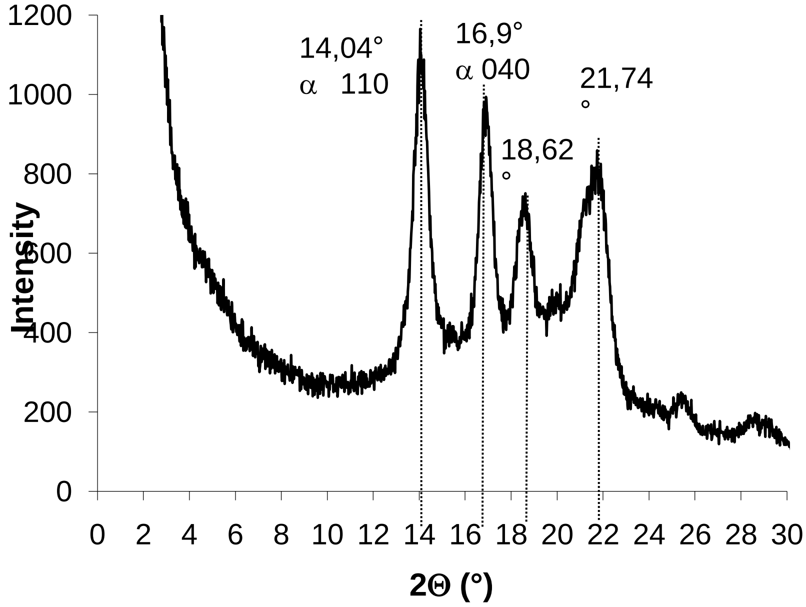

Figure 13 Characteristic peaks of the polypropylene crystalline phase.

A second 2θ angle scanning was performed in order to characterize the morphological state in the clay nanocomposite material by measuring the clay sheets interlayer spacing before and after the material blending. The spacing variation between clay layers allowed the gathering of information on filler dispersion through the polymeric matrix. As it is shown in Figure 14, measured nanoclay basal distance was $d_0 = 2.7$ nm and the distance measured after processing was *d* = 3.1nm. The difference found between initial and final interlayer distances suggests an intercalated/exfoliated morphology [132].

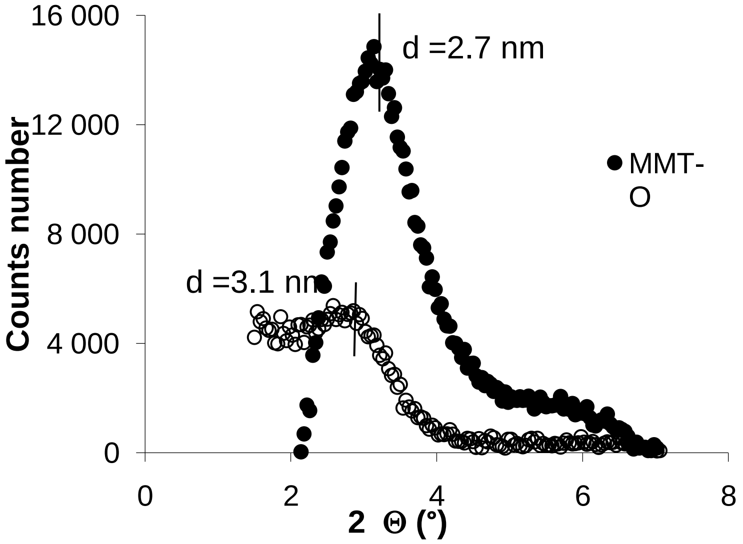

Figure 14 Differences of count number in *WAXS* tests between pure polypropylene and composite samples.

1.2.2. Scanning Transmission Electronic Microscopy (*STEM*)

To qualitatively confirm this affirmation, a *STEM* study was performed. Figure 15 shows a *STEM* image at 120,000X magnification: the dispersion degree of the clay was characteristic of intercalation with some signs of exfoliation. Aggregates composed of 8 clay sheets, in average, are clearly distinguishable at 500,000X magnification (Figure 16).

Based on both *WAXS* and *STEM* results it is possible to conclude that the nanocomposite has an intercalated/exfoliated morphology, which corresponds to the most common mixture state reached in materials prepared by the melt intercalation method [35]. Fully exfoliated morphology could be reached when the nanocomposite is obtained by *in situ* intercalative polymerization or by intercalation of polymer or pre-polymer from solution methods [133].

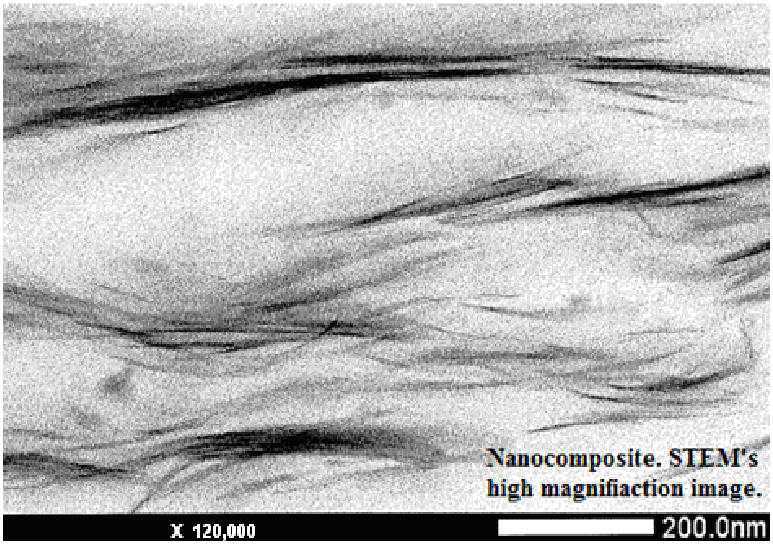

Figure 15 High magnification *STEM* image of a film cross section: nanoclay dispersion. 120,000 X photograph.

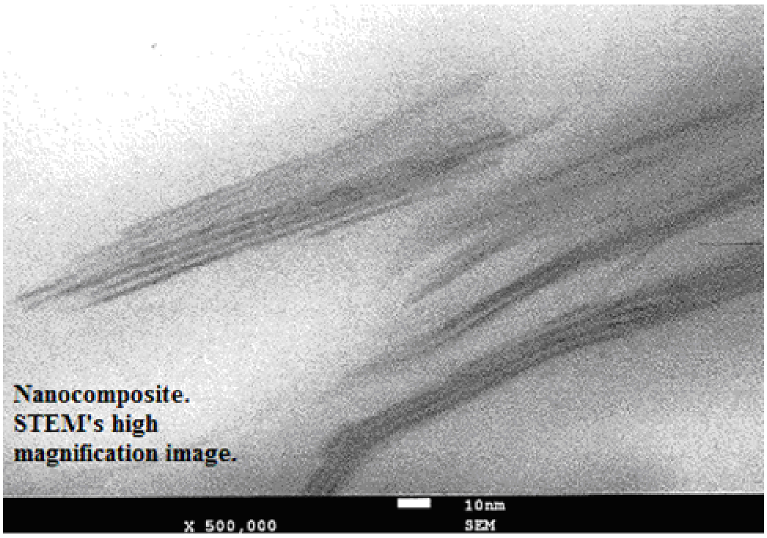

Figure 16 High magnification *STEM* image of a film cross section: nanoclay dispersion. 500,000 X photograph.

1.3. Macroscopic Scale

1.3.1. Oxygen Diffusion

We were able to measure the oxygen permeability twice for the pure polypropylene and three times for the nanocomposite, only at room temperature. The mean values were 2.28 10^{-17} $m^2s^{-1}Pa^{-1}$ and 1.17 10^{-17} $m^2s^{-1}Pa^{-1}$ respectively. It was observed a small difference but it was not statistically significant according to the number of tests. Same kinds of results were recently published for a clay nanoreinforced polypropylene system which had oxygen permeability improvements between 10 and 40% [51]. Then, due to the small difference between oxygen permeability of pure PP and nanoreinforced PP, the measurement dispersion and the unknown influence of temperature, it was preferred to use an inverse method to determine oxygen diffusion coefficient at 100°C. This issue is widely discussed in the sections corresponding to oxidation controlled by diffusion (Section 3.3).

2. Experimental Characterization of the Aging Behavior

2.1. Characterization of the Oxidation Process

Quantification of the oxidation products was done by tracking the carbonyl peak at 1713 cm^{-1} attributed mainly to carboxylic acids. Figure 17a and 17b correspond to *IR* spectra of the polypropylene and the nanocomposite in the carbonyl region for various oxidation times at 100°C. In the nanocomposite spectra, the peak at 1740 cm^{-1} grows harmonically with the peaks at 1713 cm^{-1} and 1773 cm^{-1} which belong to the pure polypropylene matrix.

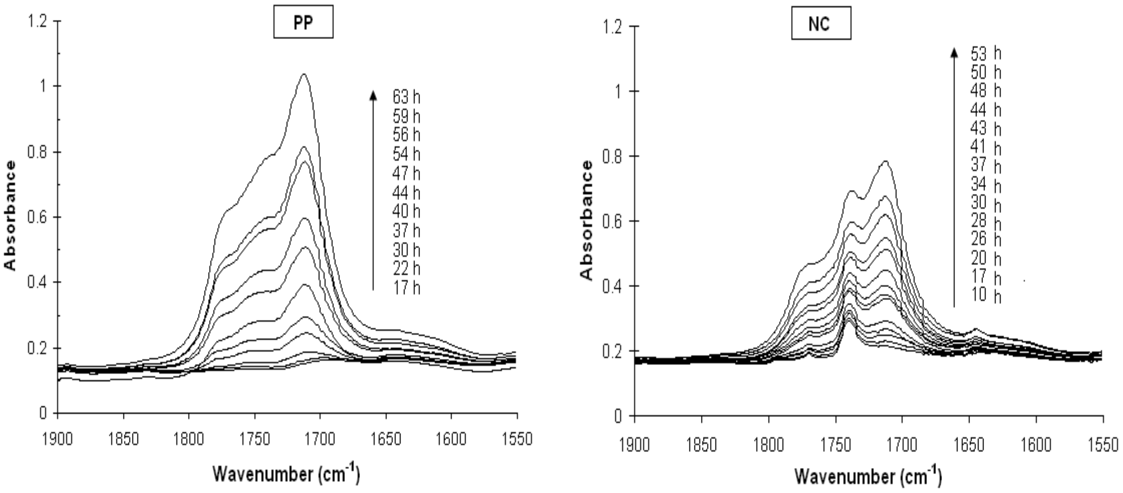

Figure 17 Changes with time of the 1713 cm^{-1}peak for *PP* and *NC* at *T*=100°C

The thermo-oxidation kinetics was studied at 60°C, 80°C and 100 °C by following the carbonyl average concentration ($[CO]_{av}$) as a function of time for the polypropylene and the nanocomposite (Figure 18).

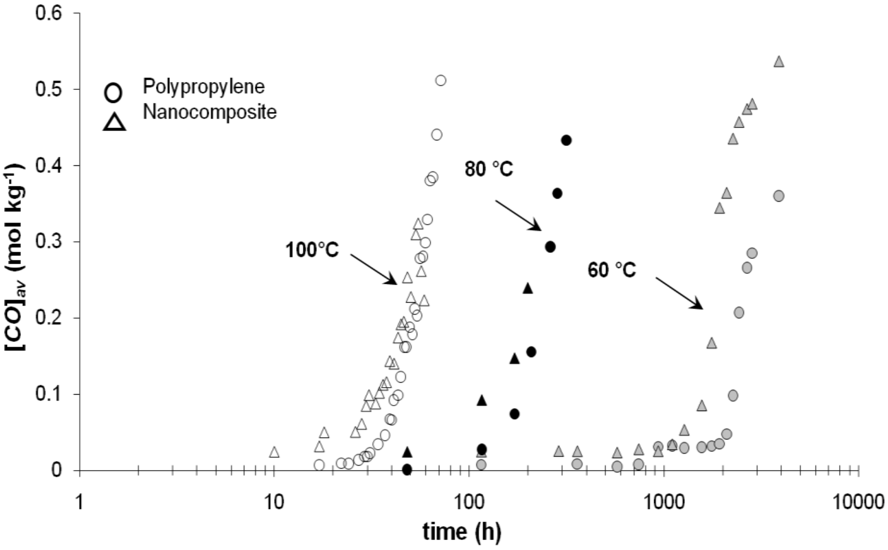

Figure 18 Kinetics of pure polypropylene and its nanocomposite at 60°C, 80°C and 100°C.

First, one observes that the resulting curves have the typical shape for a given temperature regardless of polymer identity: all curves display an induction stage followed by a short period during which oxidation is strongly auto accelerated and a steady state in which the oxidation rate is almost constant. The induction time (t_i) and the oxidation rate (r_s) are commonly used to characterize the oxidation process. The t_i value was experimentally determined as the point at which the straight-line corresponding to the steady state crossed the t-axis.

Induction time values for both polymers at the three defined temperatures are included in Table 7. It appears that the induction time values obtained for the nanocomposite are lower for all exposure temperatures, indicating that the nanocomposite is slightly more easily oxidized. The potential causes of this behavior are discussed below.

T (°C)	**t_i *PP*** (h)	**t_i *NC*** (h)
100	33	25
80	220	150
60	2010	1410

Table 7 Oxidation induction times for the polypropylene and the nanocomposite films.

In this first approach, it was necessary to assess the significance of the induction time difference between both polymers. For this purpose, we plotted in an Arrhenius diagram the induction times of polypropylene and the nanocomposite with compiled literature data (Figure 19) [76,134,135,136,137,138,139,140,141,142,143,144,145,146,147,148].

From this coarse grain point of view, it clearly appears that this difference observed in Table 7 between pure and nanocomposites is not very significant since all induction period values are situated in the scatter of points corresponding to induction period values reported in the literature. As a result, the nanocomposite can be considered as a pure polypropylene for its oxidation behavior according to this approach. Lastly, we concluded also that the nanofiller has no influence on the activation energy, its average value being close to 116 kJ mol^{-1}.

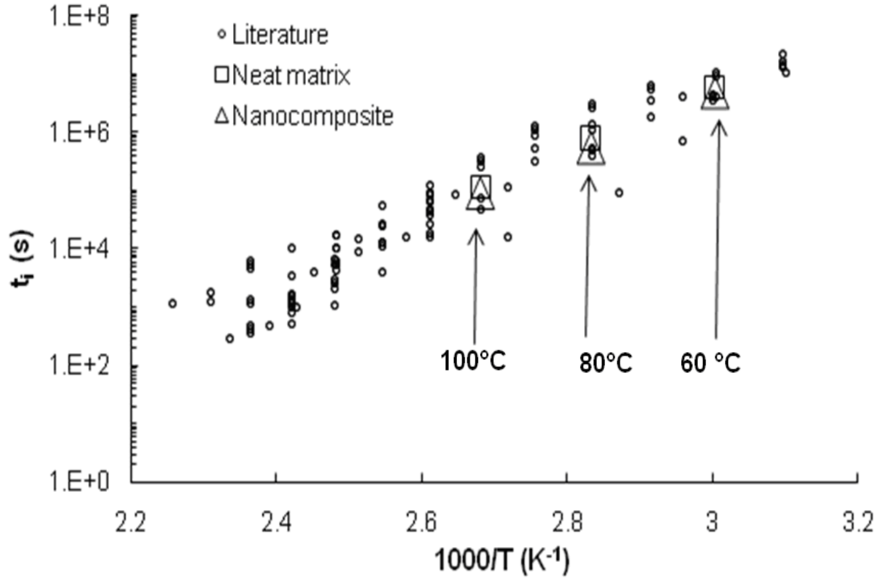

Figure 19 Arrhenius dependence for induction time (*t*$_i$) at 60°C, 80°C and 100°C for the pure polypropylene and the nanocomposite.

However, the fact that smaller induction times were systematically found for the nanoreinforced materials led us to investigate possible causes to explain the difference between both polymers under study. To explore this divergence more precisely, the carbonyl concentration was plotted as a function of time in a linear scale for an exposure temperature of 100°C (Figure 20). It is noteworthy that if the nanocomposite exhibits a lower induction period (ti_{NC}) as we have seen before, the nanocomposite also exhibits a lower oxidation rate in the steady state (r_{SPP}=1.18 10^{-2} mol $kg^{-1}h^{-1}$, r_{SNC}=1.01 10^{-2} mol $kg^{-1}h^{-1}$, $\Delta r_S \approx$ 10%).

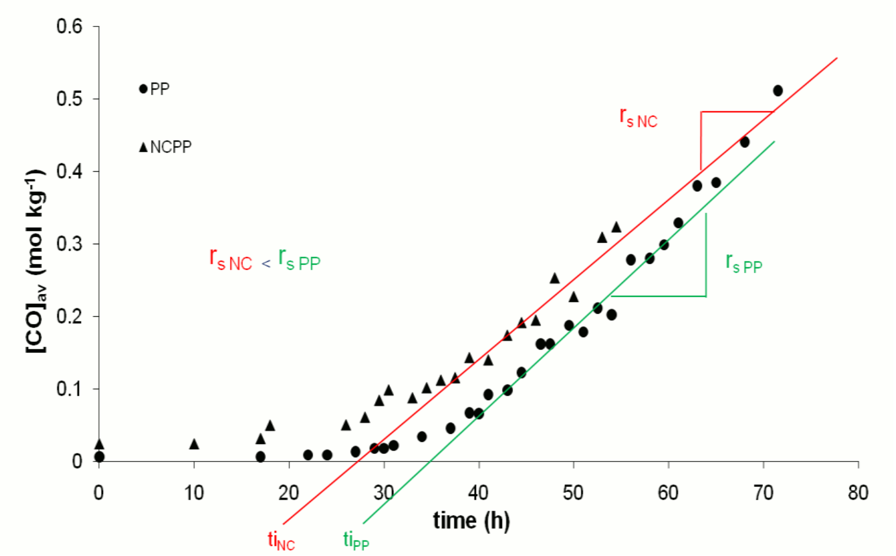

Figure 20 Experimental kinetics of polypropylene (*PP*) and its clay nanocomposite (*NC*) at 100°C.

2.2. Oxidation Profiles

Oxidation profiles were assessed by micro *ATR/FTIR* imaging (see Chapter II, section 2.1.1.2 to find a description of the test). Figures 21a and 21b respectively show carbonyl profiles for the pure and the nanocomposite.

On the y axis were plotted the relative absorbances that are the ratio between the absorbance on each point at 1713cm^{-1} and the absorbance on the surface of the sample at 1713cm^{-1}. Such values were corrected by multiplying each absorbance value by the ratio between the absorbance value on the sample surface for $[CO]_{av}$ = 0.3 mol kg^{-1} obtained from the simulation and the experimental absorbance value on the sample surface at $[CO]_{av}$ = 0.3 mol kg^{-1}. The simulation values were previously corrected by adding the carbonyl concentration measured in transmission mode at time zero before to stat the aging process.

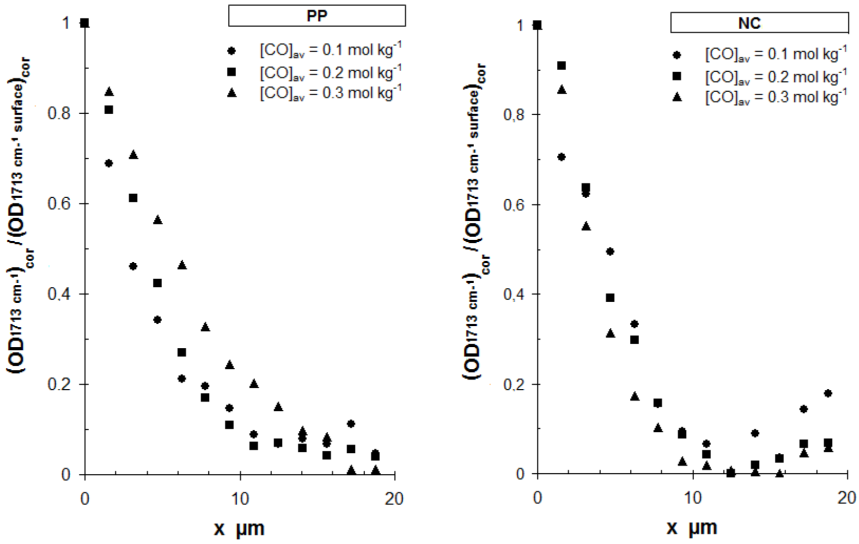

a) **b)**

Figure 21 Relative optic density (*OD*) at 1713 cm^{-1} of the experimental oxidation profiles at $[CO]_{av}$ = 0.1, 0.2 and 0.3 mol kg^{-1} for a) pure polypropylene b) nanocomposite.

It clearly appears that for both materials (Figure 21) the thicknesses of the oxidized layer is close to 15 µm, which means that the oxidation is heterogeneous after the end of the induction period and that the oxidation kinetics are oxygen diffusion limited. From our knowledge, it is the first time that an oxidation profile for *PP* was measured with such accuracy.

By comparing Figures 21a and 21b, it appeared that for the same $[CO]_{av}$ = 0.3 mol.kg^{-1} for instance, the nanocomposite showed a thickness of oxidized layer (*TOL*) close to 10 µm whereas pure *PP TOL* is about 17 µm. Such a difference could be related to the oxygen diffusion. To explore the influence of the oxygen diffusion coefficient on the shape of the oxidation profiles, and especially on the thickness of the oxidation layer we used an analytical approached which is discussed on section 3.3.

3. Simulation Approach

To model oxidation behavior of the unstabilized clay-reinforced material it is necessary to consider the montmorillonite dual influence on the oxidation phenomena: first, the montmorillonite could modify the oxidation mechanism. Second, montmorillonite may affect material physical properties, in particular, the oxygen diffusion coefficient and the reaction-diffusion coupling. Both chemical and physical influences of montmorillonite were studied in this work. Section 3.1 presents the kinetic model used to simulate the oxidation behavior of the unstabilized nanocomposite. In section 3.2, the parameters used when modeling are presented and compared to experimental and theoretical results. Section 3.3 is dedicated to discussion of the influence of oxygen diffusion coefficient variations on oxidation profiles as a function of sample thickness.

3.1. Kinetic Modeling

The Closed Loop Model (*CLM*) presented in Chapter I as a non empirical approach was used to model oxidation kinetics [73]. This model is derived from a standard mechanistic scheme in which oxidation process results from a chain reaction initiated by hydroperoxides decomposition. Alkyl ($P^{\bullet}$) and peroxyl ($PO_2^{\bullet}$) radicals are the chain carriers. The three possible terminations between these radicals were taken into account. The predictive power of this model is now well established [73,85,104].

For the general case where termination may occur by bimolecular reactions, the closed-loop mechanistic scheme involves seven elementary reactions:

Initiation

$POOH \rightarrow 2P^{\bullet} + H_2O + P = O$ Unimolecular (Ia)

$2POOH \rightarrow P^{\bullet} + PO_2^{\bullet} + H_2O + P = O$ Bimolecular (Ib)

Propagation

$P^{\bullet} + O_2 \rightarrow PO_2^{\bullet}$ (II)

$PO_2^{\bullet} + PH \rightarrow POOH + P^{\bullet}$ (III)

Termination

$P^{\bullet} + P^{\bullet} \rightarrow Inactive\ products$ (IV)

$P^{\bullet} + PO_2^{\bullet} \rightarrow Inactive\ products$ (V)

$PO^{\bullet}{}_2 + PO^{\bullet}{}_2 \rightarrow Inactive\ products$ (VI)

A set of ordinary differential equations was derived from this scheme; it expresses the concentration changes of the involved reactive species. Equations 1, 2 and 3 correspond to the alkyl radical ($P^{\bullet}$), peroxyl radical ($PO_2^{\bullet}$), and hydroperoxide ($POOH$) concentrations respectively, and k_{1u}, k_{1b}, k_2, k_3, k_4, k_5, and k_6 are the rate constants for reactions I to VI.

$$\frac{d\left[P^{\bullet}\right]}{dt} = 2k_{1u}\left[POOH\right] + k_{1b}\left[POOH\right]^{2} \\ - k_{2}\left[P^{\bullet}\right]\left[O_{2}\right] + k_{3}\left[PO_{2}^{\bullet}\right]\left[PH\right] - 2k_{4}\left[P^{\bullet}\right]^{2} - k_{5}\left[P^{\bullet}\right]\left[PO_{2}^{\bullet}\right] \tag{1}$$

$$\frac{d\left[PO_{2}^{\bullet}\right]}{dt} = k_{1b}\left[POOH\right]^{2} + k_{2}\left[P^{\bullet}\right]\left[O_{2}\right] - k_{3}\left[PO_{2}^{\bullet}\right]\left[PH\right] - k_{5}\left[P^{\bullet}\right]\left[PO_{2}^{\bullet}\right] - 2k_{6}\left[PO_{2}^{\bullet}\right] \tag{2}$$

$$\frac{d\left[POOH\right]}{dt} = -k_{1u}\left[POOH\right] - 2k_{1b}\left[POOH\right]^{2} + k_{3}\left[PO_{2}^{\bullet}\right]\left[PH\right] \tag{3}$$

The initial and boundary conditions input to solve the system of differential equation were $\left[PO_{2}^{\bullet}\right] = 0, \left[P^{\bullet}\right] = 0$, $\left[POOH\right] = \left[POOH\right]_{0}$, $\left[PH\right] = \left[PH\right]_{0}$, $\left[O_{2}\right] = \left[O_{2}\right]_{s}$, where $\left[PH\right]_{0}$ *and* $\left[O_{2}\right]_{s}$ are the initial concentrations of the $\left[PH\right]$ *and* $\left[O_{2}\right]$ species respectively.

The oxygen diffusion effect could also be included in the *CLM* by adding the oxygen diffusion term (Eq. 4). Do_2 is the coefficient of oxygen diffusion in the polymer. This coefficient is lower in the nanocomposite than in the pure matrix.

$$\frac{d\left[O_{2}\right]}{dt} = D_{O_{2}}\left(\frac{\partial^{2}\left[O_{2}\right]}{\partial^{2}x^{2}}\right) - k_{2}\left[P^{\bullet}\right]\left[O_{2}\right] + k_{6}\left[PO_{2}^{\bullet}\right]^{2} \tag{4}$$

The *CLM* input was completed by adding an extra condition related to the oxygen diffusion: at any time, $\left[O_{2}\right] = \left[O_{2}\right]_{s}$ for $x = -\frac{L}{2}$ and $x = \frac{L}{2}$, the origin of depth coordinates being taken in the middle of the sample thickness.

Assuming that the source of carbonyl group (*CO*) is the decomposition of hydroperoxides, carbonyl concentration $[CO]_{av}$ was written as:

$$\frac{d[CO]_{av}}{dt} = \left[k_{1u}[POOH] + k_{1b}[POOH]^2\right] * \left[1 - X_c - MMT\right] * \rho_{PP}{}^{-1} \qquad (5)$$

where X_c is the crystallinity ratio of the sample expressed in volume fraction (X_c = 0.5) and *MMT-O* is the volume fraction of montmorillonite equal to 0.08 in our case. Since oxidation occurs only in the amorphous phase, the X_c and *MMT-O* terms were included in Equation 5 as correction factors related to the amorphous phase fraction present in the polymer in which oxidation occurs. The kinetic parameters values for pure polypropylene reported by Richaud [73] are shown in Table 8.

Constants	**Pre-exponential factor (s^{-1} or $mol^{-1}s^{-1}$)**	**E_a ($kJ\ mol^{-1}$)**
k_{1u} (s^{-1})	$1.19\ 10^{11}$	135
k_{1b} ($l\ mol^{-1}\ s^{-1}$)	$5.42\ 10^{7}$	84
k_2 ($l\ mol^{-1}\ s^{-1}$)	$5.38\ 10^{7}$	5
k_3 ($l\ mol^{-1}\ s^{-1}$)	$9.80\ 10^{7}$	60
k_4 ($l\ mol^{-1}\ s^{-1}$)	$9.74\ 10^{9}$	0
k_5 ($l\ mol^{-1}\ s^{-1}$)	$2.66\ 10^{9}$	0
k_6 ($l\ mol^{-1}\ s^{-1}$)	$7.94\ 10^{11}$	60

Table 8 Kinetic constants of the closed loop model for the polypropylene and its nanocomposite.

3.2. Carbonyl build-up simulation

The initial hydroperoxide concentration $[POOH]_0$ can be considered as the initial $POOH$ concentration kinetically equivalent to the concentration of all the radical sources initially present in the material. Its value is generally lower than the sensitivity threshold of available titration methods. It appears thus as an adjustable parameter of the kinetic model. To illustrate the sensitivity of the model to changes of this parameter, simulated carbonyl growth curves are included in Figure 22 adjusting $[POOH]_0$ values for both pure and reinforced polypropylene to fit experimental carbonyl growth curves at 100°C in Figure 18.

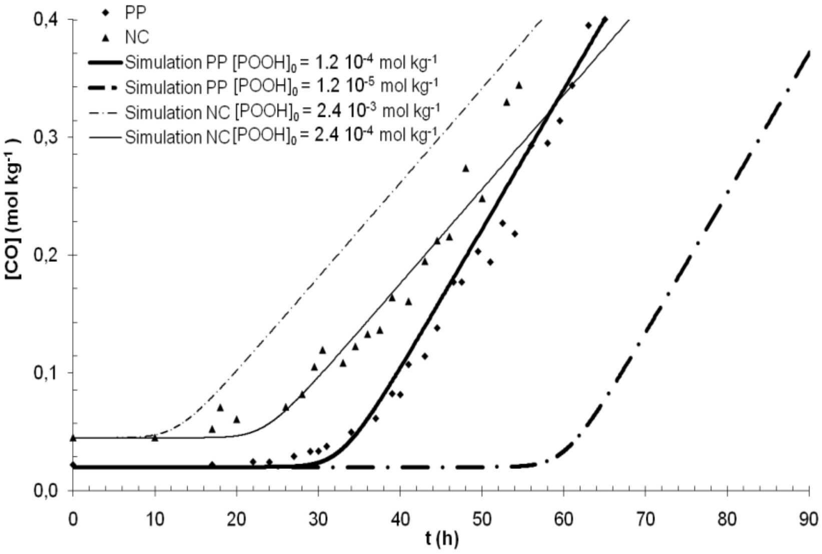

Figure 22 Comparison between experimental data and simulation kinetic curves at 100°C and $[POOH]_0$ influence on kinetic curves: $[POOH]_{0NC}$: 2.4 10^{-3} and 2.4 10^{-4} mol kg^{-1}, $[POOH]_{0PP}$: 1.2 10^{-4} and 1.2 10^{-5} mol kg^{-1}.

After optimization, we selected for the pure and reinforced polypropylene $[POOH]_{0\ PP} = 1.2\ 10^{-4}$ mol kg^{-1}, and $[POOH]_{0\ NC} = 2.4\ 10^{-4}$ mol kg^{-1} respectively to achieve a good agreement between the experimental and simulated CO values at the three studied temperatures (Figure

23, Table 9). These results can be interpreted as follows: montmorillonite exerts a direct (catalytic effect by metallic impurities) or indirect (thermomechanic history during processing) small influence on nanocomposite preoxidation, leading to the reduction of the induction time. A similar effect has been observed from the presence of residual Ziegler-Natta catalyst Titanium [149].As a result, the initial hydroperoxide concentration is slightly higher in the nanocomposite than in the pure polymer, which explains the observed difference in the oxidation behavior. It is noteworthy that a slight catalytic effect of montmorillonite on *PP* photooxidation was already reported in the case of intercalated and exfoliated samples [90,110].

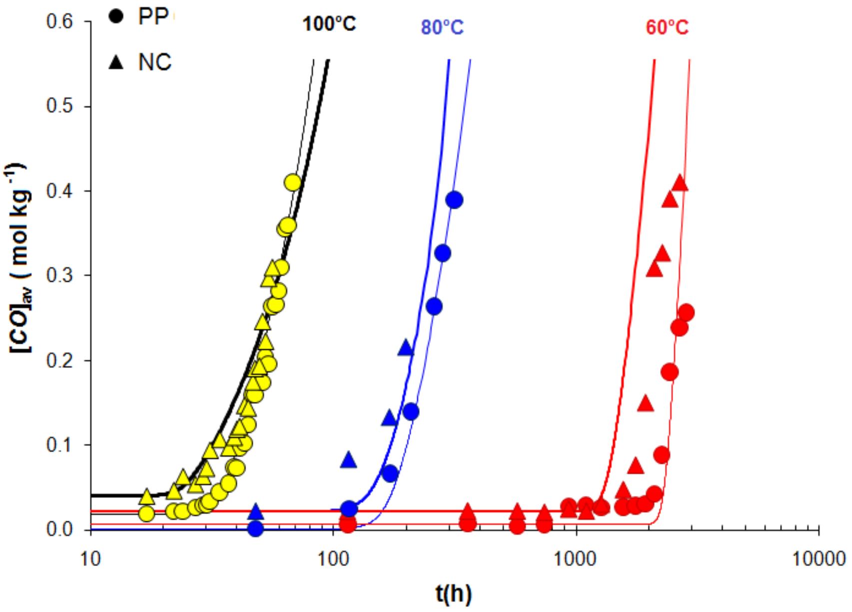

Figure 23 Thermo degradation kinetics foe the PP and the NC: Experimental and simulation results at 60°C, 80°C and 100°C.

The steady state behavior was well simulated without parameter modifications (Figure 23). The disparity between *PP* and the nanocomposite is only due to the difference in the amorphous phase concentration (see Equation 5). It is recalled that in a closed-loop process, the steady state behavior is independent of the initiation rate. Experimental observations were thus in good agreement with theoretical predictions.

	$[PH]_0$ (mol kg^{-1})	**$[POOH]_0$** (mol kg^{-1})	**X_c**	***MMT***
PP	20	1.2 10^{-4}	0.5	0
NC	20	2.4 10^{-4}	0.5	0.1

Table 9 Material parameters used in the closed loop model.

3.3. Oxidation Controlled by Diffusion

When the oxidation process is controlled by oxygen diffusion, oxidation rate and oxygen diffusion competition lead to an oxidation profile formation. In other words, oxidation is likely confined to a superficial layer when film thickness is higher than 20 µm as predicted by Rincon LM [73]. According to the measured oxidation profiles (Figure 21a and 21b), there is a difference between the thickness of the pure polypropylene and the nanocomposite oxidized layer. In that case, it should be possible to describe the oxidation behavior of both materials using as fitting variable the oxygen diffusion coefficient, which is different for each material. Since permeation tests displayed relatively high incertitude, it seemed interesting to determine oxygen diffusion coefficients of pure and nanoreinforced polypropylene from the kinetic model, using an inverse method.

The values of the oxygen solubility and the oxygen diffusion coefficients reported in the literature and extrapolated at 100°C and those determined by inverse method (used as input parameters of the *CLM*) are showed in Table 10.

For the sorption coefficient a unique common value was fixed for both the pure polypropylene and the nanocomposite. Since S_{O2} is a thermodynamic parameter only depending on the oxygen – amorphous phase chemical interactions the clay presence should not change this relationship. Furthermore, as the S_{O2} activation energy is very small (4.13 kJmol^{-1}), S_{O2} was set as 1.1 10^{-7} mol l^{-1} Pa^{-1} for the three studied temperatures. This value was the same used to perform all the simulations when oxidation process is not controlled by oxygen diffusion (Section 3.2).

	T (°C)	**S_{O2} (mol l^{-1} Pa^{-1})**	**$D_{O2\ PP}$ (m^{2}s^{-1})**	**$D_{O2\ NC}$ (m^{2}s^{-1})**
Literature Ea (kJmol^{-1})		4.13	43.4	-
Extrapolation	100	1.4 10^{-8}	9.3 10^{-10}	-
Inverse method	100	1.1 10^{-7}	2.0 10^{-12}	1.2 10^{-12}

Table 10. Oxygen permeability properties for the pure polypropylene and the nanocomposite at 100°C.

Figure 24 illustrates the influence of oxygen diffusion coefficient value on the oxidation profile shape at 100°C and a $[CO]_{av}$ equal to 0.3 mol kg^{-1} for the pure polypropylene. Several oxygen diffusion coefficient values Do_2 ranging from 2 10^{-13}m^{2}s^{-1} and 2.0 10^{-11} m^{2}s^{-1} were used in simulation. It is noticeable that for such D_{O2} values, the profile shape radically changes: high D_{O2} generates wide profiles, but for smaller values of D_{O2} the obtained oxidation profiles are narrowed. It is observable that the kinetic model is sensitive enough to catch D_{O2} small changes and their influence on the shape of the oxidation profiles. This way it was possible to identify the oxygen coefficient value for each of both materials: Do_2 = 2.0 10^{-12} m^2s^{-1} and 1.2 10^{-12} m^2s^{-1} for the polypropylene and the nanocomposite respectively (Table 10, inverse method).

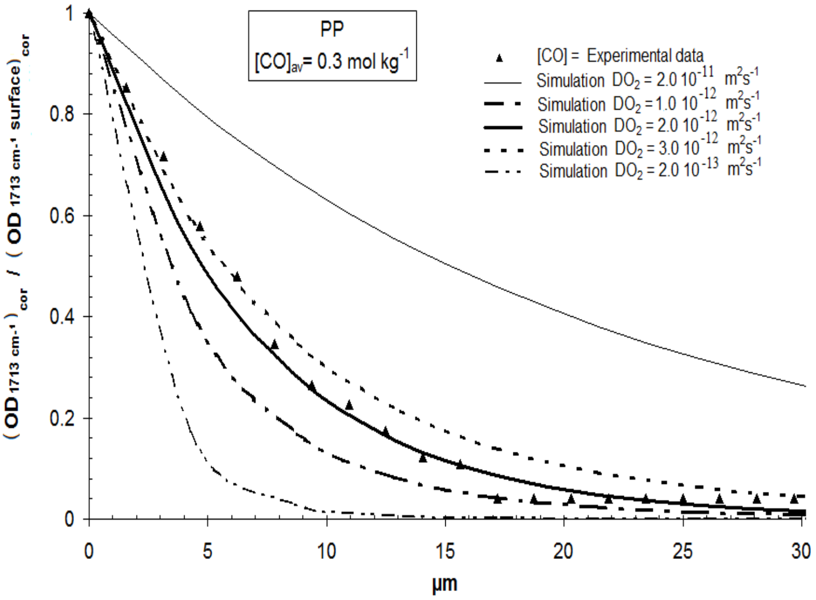

Figure 24. Influence of the oxygen diffusion coefficient *Do_2* variation on the simulated carbonyl distribution across 150μm-thick *PP* films at *$[CO]_{av}$* = 0.3 mol kg^{-1}.

The difference between D_{O2} extrapolated and determined by inverse method values (Table 10) is probably due to measurement incertitude and to the oxygen diffusion process non – Arrhenian behavior at higher temperatures.

Figure 25 shows the theoretical and experimental oxidation profiles in mol.kg^{-1} for three different exposure times corresponding to the average concentration in the all thickness of the film $[CO]_{av}$ = 0.1, 0.2, and 0.3 mol.kg^{-1}. The latter concentrations were measured in transmission mode using the Beer Lambert-law, it means that on the y- axis of the Figure 25a and 25b were represented the values of the integration of $[CO]_{av}$ along the 150 µm-sample thickness. Experimental values were treated using a single adjusting factor which equals the experimental absorbance in the sample thickness to the simulated $[CO]_{av}$ on the sample surface for an average carbonyl concentration of $[CO]_{av} = 0.3$ mol kg^{-1}. Figures 25a and 25b display respectively the last 20 µm (from the surface) of a pure and nanocomposite polypropylene cross-sections.

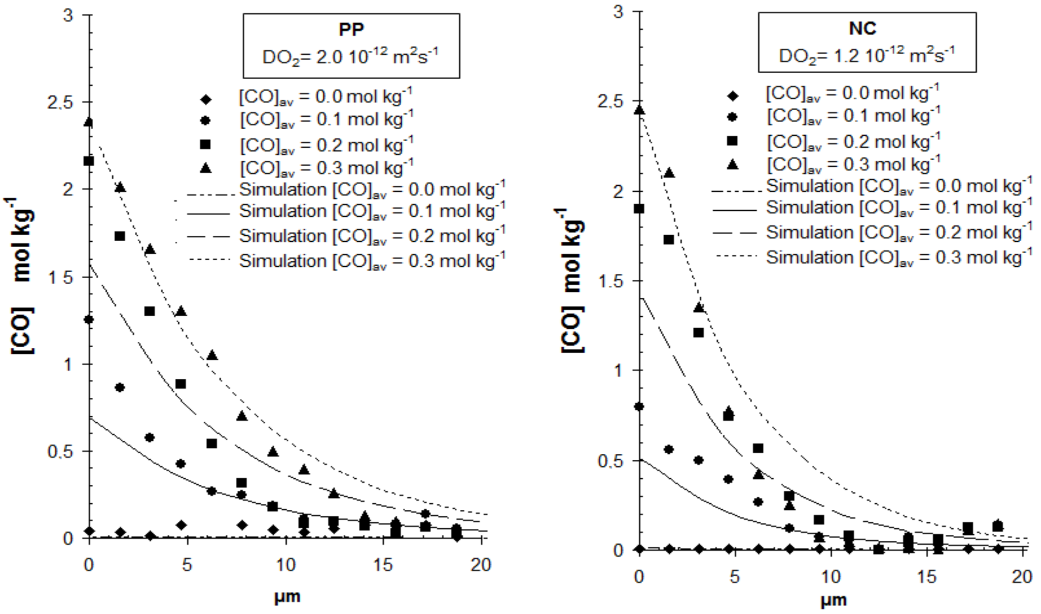

Figure 25. Theoretical and experimental oxidation profiles in pure and reinforced polypropylene films for $[CO]_{av}$ equal to 0.1, 0.2, 0.3 mol kg^{-1}: a) pure polypropylene, simulated with D_{O_2PP}: 2.0 10 $^{-12}$ m^{2}s^{-1}. b) Nanocomposite, simulated with D_{O_2NC}: 1.2 10^{-12} m^{2}s^{-1}.

As shown in Figure 25a good agreement between simulation and experimental data was obtained by using for pure polypropylene, D_{O_2PP}: 2.0 10^{-12} m^{2}s^{-1} and for nanocomposite D_{O_2NC}: 1.2 10^{-12} m^{2}s^{-1}. A little noise was found in the profile simulation of the nanocomposite, this is attributed to mixing effects related to the clay dispersion in the matrix and to the quality of the sample surface when *ATR* testing was performed.

Since the *TOL* was 17µm for the *PP* and 10µm for the nanocomposite, it is important to point out that the *TOL* results from the competition between the oxidation rate and O_2 diffusion (see kinetic model where the differential equations included oxidation and Fick O_2 diffusion). However, there is no theoretical reason to assume that nanofillers increase oxidation rate since this latter is linked to the propagation (k_3) and termination (k_6) steps of oxidation mechanism and the amorphous phase content. This may be why nanofiller acts only as “defects” leading to decrease induction period (increase of $[POOH]_0$ in the modelling). Furthermore, in Figure 22, the experimental oxidation rate corresponding to the slope of $[CO]_{av}$ build-up after the induction period measured on thin films (75 µm), shows a decrease in the case of *NC* compare to *PP* which is explained by the decrease of the amorphous phase content. At last, from the modelling point of view, an oxidation rate increase (by increasing k_3 for instance) does not permit a good description of the oxidation profiles. As a result, the simulated profile curves are unique for a good fit of all experimental data (carbonyl build-up and profiles).

Conclusions

Thermal oxidation of pure polypropylene and the clay nanoreinforced polypropylene has been studied experimentally and simulated with a kinetic model. The first objective of this study was to determine possible effects of montmorillonite on the oxidation kinetic behavior of polypropylene at moderate temperatures. Slight differences between induction times of polypropylene and nanocomposite were found. They can be attributed to a presumed catalytic effect of montmorillonite impurities on *PP* oxidation or simply to a difference in thermomechanical histories between *PP* and the nanocomposite. From a modelling point of view, this effect can be taken into account by increasing the initial hydroperoxide concentration $[POOH]_0$. As a result, montmorillonite could be considered as a filler which leads an oxidation rate increase only during the induction period.

The second objective was to study the physical effect of montmorillonite in polypropylene and its effects on oxidation profiles. By using the *ATR-FTIR* microscope, evidence was obtained that oxidized layer thickness is close to 17 µm for the pure polypropylene and 10 µm for the clay nanocomposite for an exposure at 100°C. This difference has been attributed to the decrease of the oxygen diffusion coefficient when montmorillonite was present. This hypothesis has been examined by simulating carbonyl profiles: a good agreement between experimental profiles and simulated ones was obtained by using an oxygen diffusion coefficient value (D_{O2}) for the nanocomposite 40% smaller that for pure polypropylene.

References

132 Aloisi G, Costantino U, Latterini L, Nocchetti N, Camino G, Frache A. Preparation and spectroscopic characterization of intercalation products of clay and of clay–polypropylene composites with rhodamine B. J Phy Chem Sol 2006; 67: 909–914.

133 Boucard S, Duchet J, Gérard JF, Prele P, Gonzales S. Processing of polypropylene – clay hybrids. Macromolecule Symposium 2003; 194: 241-246.

134 Roginsky V.A, In developments in polymer degradation -5. Applied Science Publishers; 1984: Chap. 6, 193-225.

135 Meltzer T.H, Kelley J.J, Goldey R.N. J. Appl. Polym. Sci. 3; 1960: 84-89

136 Iring M, Laszlo-Hedvig S, Barabas K, Kelen T, Tudos F, Eur. Polym. J. 1978 ; 14: 439-442.

137 Tudos F, Iring M, Kelen T, Int. Conf. On Adv. In The Stab. And Contr. Degrad. of Polym, 1, 1984; 86-98.

138 Hansen R.H, Russell C.A, De Benedictis T, Martin N.M, Pascale J.V, J. Polym. Sci., A2; 1964: 587.

139 Chien J.C, Boss C.R; J. Polym. Sci;1967; 5: 3091.

140 Hawkins W.L, Matreyek W, Winslow F.H, J. Polym. Sci, 1959; 41: 1-11.

141 Schwarz T, Steiner G, Koppelmann J, J. Appl. Polym. Sci., 1989; 38: 1-7.

142 Al-Malaika S, Scott G, Huczkowski P, Polym. Deg. Stab, 1984; 7: 95-107.

143 Billingham N.C Makromol, Chem,, Macromol, Symp, 1989; 28: 145-163.

144 Billingham N.C, Prentice P, Walker T.J, J. Polym. Sci, 1976; 57: 287-297

145 Boss C.R, Chien J.C, J. Polym. Sci. Part A1, 1966 ;4 : 1543-1551.

146 Mettler-Toledo GmbH. Operating Instructions. 2001.

147 Al-Malaika S. Polym. Deg. Stab. 1991; 34 : 1-36.

148 Billingham N.C, Calvert P.D, In Developments In Polymer Stabilisation - 3, Chap. 5: 97.

149 Goss B, Nakatani H, George GA, Terano M. Polym Degrad Stab 2003;82:119-126.

Chapter IV

Thermal Degradation of Clay Nanoreinforced Polyethylene

Index of Figures

Index of Tables

Résumé Chapitre IV

Nanocomposite à matrice polyéthylène

D’une façon identique à la démarche adoptée dans le cas du nanocomposite à matrice polypropylène, ce chapitre traite de l’oxydation de nanocomposite à matrice polyéthylène et de la matrice seule. L’objectif est ici de mettre en évidence l’influence de la *MMT-O* sur la cinétique d’oxydation à partir d’échantillon mince (160 µm) assurant que l’oxydation n’est pas contrôlée par la diffusion d’oxygène et à partir d’échantillon épais de 1400 µm pour mettre en évidence un gradient d’oxydation. On suit ici non seulement les modifications chimiques (apparition de carbonyle, coupure de chaine) mais aussi les conséquences de ces modifications sur la morphologie cristalline et les variations de propriétés de transport de l’oxygène. Enfin, dans le cas des échantillons épais, les variations de propriétés mécaniques en termes de module seront examinées.

Dans une première partie, on traite de la caractérisation de l’état de dispersion de la *MMT-O* dans le nanocomposite. Cette caractérisation a été effectuée par diffraction des rayons *X* (*WAXS*) et par microscopie électronique en transmission (*STEM*). Il apparait que l’état de dispersion est de type intercalé. Les propriétés de transport de l’oxygène sont évaluées par perméamétrie à différentes températures afin de déterminer le coefficient de diffusion de l’oxygène aux températures de vieillissement accéléré (60°C, 80°C, 100°C). La présence de la *MMT-O* au sein du polyéthylène n’entraine pas une diminution significative de ce dernier coefficient.

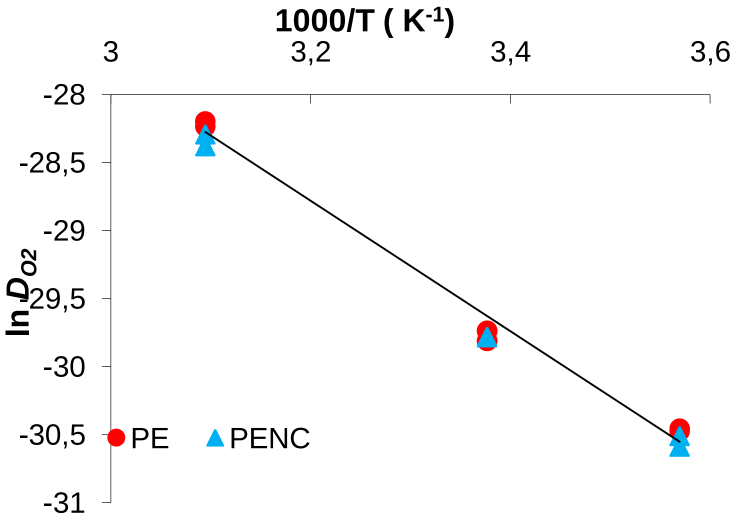

Comportement arrhénien du coefficient de diffusion de l'oxygène du *PE* and du *PENC* dans un intervalle de température entre 280 et 323 K

Conformément à notre méthodologie, cette deuxième partie traite de l'influence de la présence de *MMT-O* sur l'oxydation du polyéthylène. Pour s'affranchir du phénomène de diffusion d'oxygène, on se limite ici au cas des échantillons minces (160 µm). On met en évidence les cinétiques d'oxydation au travers de l'évolution de la concentration en carbonyle au cours de vieillissements accélérés à 60°C, 80°C et 100°C. Le temps d'induction (t_i) correspondant à l'apparition significative de carbonyle par *FTIR* diminue avec la présence de *MMT-O* dans le polyéthylène alors que la vitesse d'oxydation (r_s) déterminer en régime pseudo-stationnaire augmente avec la présence de *MMT-O*, comme il est résumé dans le tableau suivant :

T (°C)	$t_{i\ PE}$ (h)	$t_{i\ PENC}$ (h)	r_s *PE* (mol l^{-1} h^{-1})	r_s *PENC* (mol l^{-1} h^{-1})
60	3000	1900	1.0 10^{-4}	9.0 10^{-4}
80	490	250	6.0 10^{-4}	24.0 10^{-4}
100	120	60	25.5 10^{-4}	71.5 10^{-4}

Temps d'induction (t_i), vitesse d'oxydation (r_s) du *PE* et *PENC* à 60°C, 80°C et 100°C.

Ces variations significatives de temps d'induction et de vitesse d'oxydation sont cependant à relativiser lorsqu'on prend le soin de reporter ces valeurs dans une compilation issue de la littérature traitant de l'oxydation de polyéthylènes. Toujours est-il qu'il est raisonnable d'attribuer ces variations à un phénomène de réactions catalytiques entre des éléments métalliques initialement présents dans la *MMT-O* et les hydroperoxydes (POOH) provenant de l'oxydation de la matrice. Pour prendre en compte ce phénomène, on se propose de rajouter aux mécanismes réactionnels de l'oxydation du polyéthylène un amorçage supplémentaire :

$$POOH + M^{n+} \rightarrow PO^{\bullet} + M^{(n+1)+} + HO^{-} \qquad (1)$$

$$POOH + M^{(n+1)} \rightarrow POO^{\bullet} + M^{n+} + H^{+} \qquad (2)$$

$$POOH + POOH \rightarrow PO^{\bullet} + POO^{\bullet} + H_2O \qquad (3)$$

La modélisation cinétique de l'oxydation du nanocomposite est alors possible en introduisant une nouvelle constante cinétique k_{1m} (et son énergie d'activation associée) dont la valeur est déterminée par méthode inverse à partir des cinétiques d'apparition des carbonyles. Une étude paramétrique nous permet de confirmer que seul un amorçage tel qu'il écrit à l'équation (3) permet de décrire l'ensemble de comportement du nanocomposite vis-à-vis de l'oxydation.

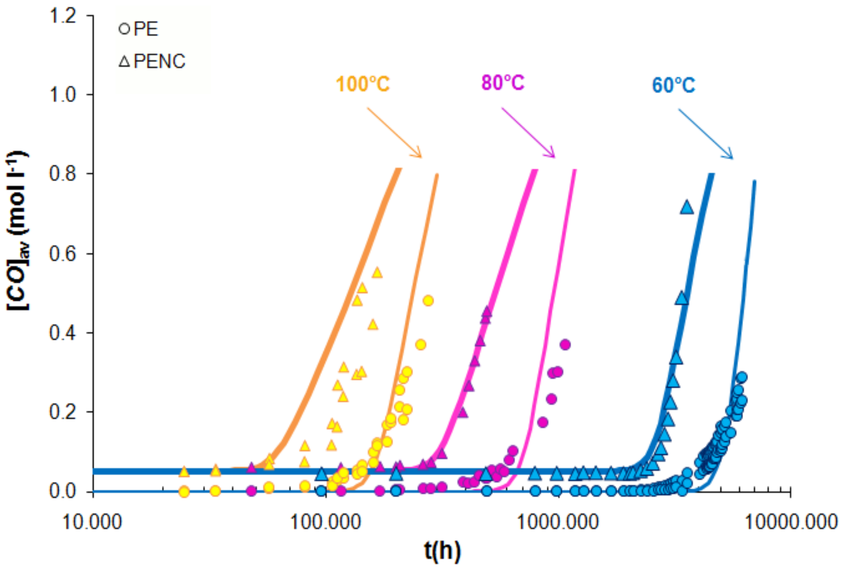

Cinétique d'oxydation expérimental et simulée du *PE* et du *PENC* à *PE* 60°C, 80°C et 100°C.

Au cours de l'exposition à 100°C sous air, des mesures de molaires par chromatographie à exclusion stérique ont permis de mettre en évidence la cinétique de coupure de chaine. Les cinétiques de coupure de chaine confirment celles obtenues par *FTIR*. Ceci indique que le processus de coupure de chaine n'est pas en lui-même modifié par la *MMT-O*. On obtient un bon accord entre le modèle cinétique et ces résultats expérimentaux pour un rendement en coupure de chaine estimé à 0.35 que ce soit pour le nanocomposite ou la matrice seule.

Les évolutions de taux de cristallinité ont été suivies par *AED* et par densité (exposition à 100°C sous air). Les deux techniques mettent en évidence une augmentation de taux de cristallinité. Cependant l'augmentation observée par *AED* apparait plus faible que celle observé par mesure de densité. Outre le phénomène de chimicristallisation correspondant à l'incorporation de chaines (initialement dans la partie amorphe) dans la partie cristalline (ou dans la mésophase), l'augmentation de densité peut être aussi attribuée au phénomène d'incorporation d'atomes d'oxygène dans la phase amorphe. Afin de prendre en compte ce dernier phénomène, une correction du taux de cristallinité apparent par densité est proposée. Grace à cette correction, il est alors possible de donner deux bornes pour le taux de cristallinité au cours de l'oxydation : une borne supérieure correspondant au taux de cristallinité apparent déduit des valeurs de densité corrigées et une borne inférieure correspondant au taux de cristallinité déduit des mesures d'*AED*.

A partir de ces données et de la cinétique de coupure de chaine, on identifie le rendement de chimicristallisation (y) correspondant au nombre de motif monomère incorporant la phase cristalline pour chaque acte de coupure de chaine ::

$$\frac{dx_C}{dt} = y * M_m * \frac{ds}{dt} \qquad (4)$$

Avec s le nombre de coupure de chaine et M_m la masse molaire du monomère (14 g mol^{-1} dans le cas du *PE*). A partir des mesures de densité corrigé donnant le taux de cristallinité apparent , y est de l'ordre de 70 alors que y est proche de 30 en se basant sur les valeurs de taux de cristallinité *AED*. Cette différence peut être attribuée au grossissement de l'interphase se situant entre la phase cristalline et la phase amorphe (voir ci-dessous).

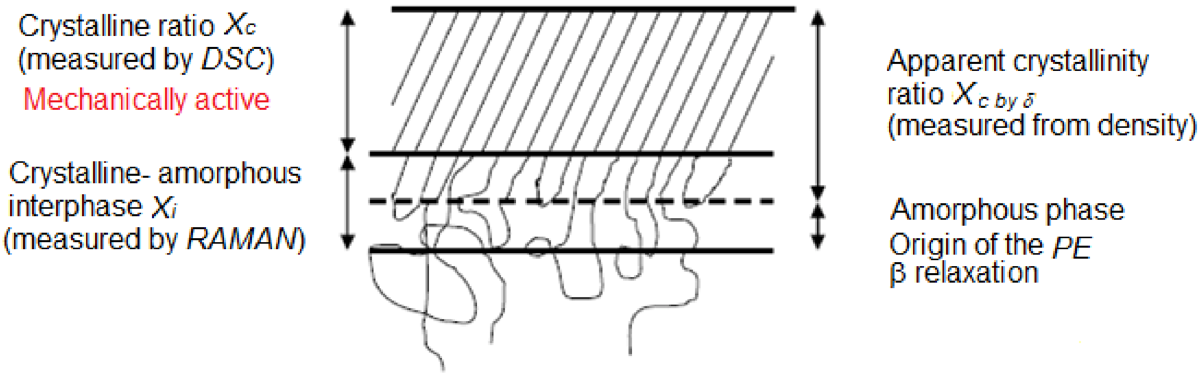

Cette dernière relation nous permet alors de modéliser l'augmentation du taux de cristallinité pour les deux techniques de mesure de taux de cristallinité :

$$\frac{dx_C}{dt} = y * M_m * \begin{bmatrix} \gamma_s * k_{1u}[POOH] + k_{1b}[POOH]^2 \\ \qquad + k_{1m}[POOH]^2 + k_{62}[POOP]_{cage} \end{bmatrix} * [1 - MMT - X_c] \tag{5}$$

Une dernière étape consiste à prédire les propriétés de transports au cours du vieillissement en considérant que les variations de perméabilité et diffusion sont gouvernées par les variations de cristallinité (taux de cristallinité apparent) suivant les relations suivantes :

$$P(X_c, T) = P_{am} * \exp(-A(T) * X_c)) \tag{6}$$

$$D(X_c, T) = D_{am} * \exp(-A(T) * X_c)) \tag{7}$$

P_{am} et D_{am} étant respectivement la perméabilité et la diffusion de l'oxygène de la phase amorphe.

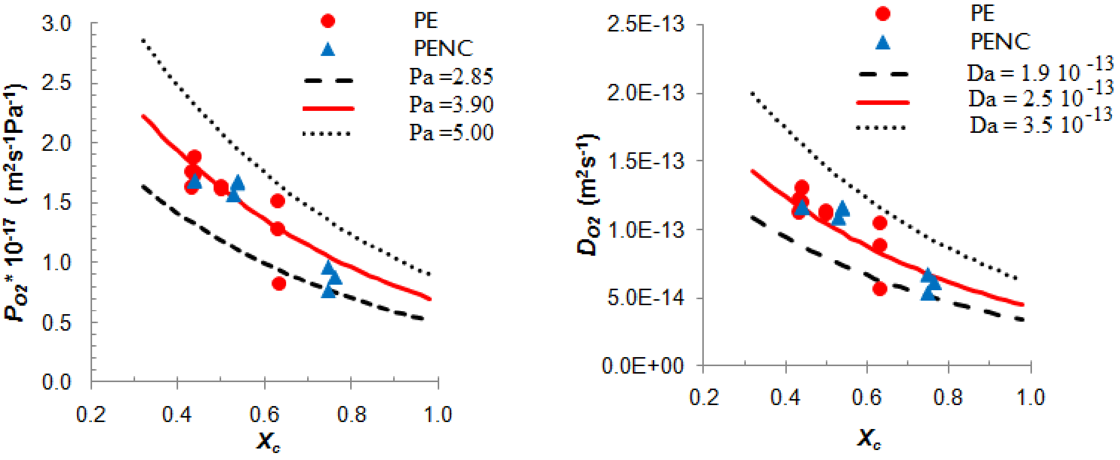

a) **b)**

Prédiction (à 23°C) des variations de a) la perméabilité à l'oxygène et b) le coefficient de diffusion de l'oxygène en fonction des changements du taux de cristallinité (X_c) dans le temps pur le *PE* et le *PENC* après d'une exposition thermique à 100°C.

Dans une deuxième partie, on s'intéresse au cas où l'oxydation est contrôlée par la diffusion d'oxygène. Les échantillons de nanocomposite et de matrice seule présentent alors une forte épaisseur (1400 µm). Pour mettre en évidence les gradients d'oxydation, on utilise ici la cartographie infrarouge en mode réflexion (*ATR*) et en mode transmission. Concernant le nanocomposite en mode Transmission, il apparait des gradients d'oxydation sur 520 µm alors que l'oxydation apparait comme homogène pour un même degré de conversion globale pour la matrice seule. Cette différence est confirmée par les mesures en mode réflexion (*ATR*). Il est donc clair que l'oxydation est fortement contrôlée par la diffusion d'oxygène dans le cas du nanocomposite.

Pour simuler le phénomène d'oxydation contrôlée par la diffusion d'oxygène, on inclut au système d'équation différentielle une équation prenant en compte d'une part la consommation d'oxygène par l'oxydation et d'autre part l'apport d'oxygène depuis la surface par la diffusion :

$$\frac{d[O_2]}{dt} = D_{O_2}\left(\frac{\partial^2[O_2]}{\partial^2 x^2}\right) - k_2[P^\bullet][O_2] + k_6[PO_2^\bullet]^2 \qquad (8)$$

On obtient un bon accord entre les gradients d'oxydation expérimentaux et les simulations pour les deux matériaux. Ceci confirme que l'apparition de forts gradients d'oxydation dans le cas du nanocomposite est liée au fait que la *MMT-O* accélère le processus d'oxydation et non pas au simple effet barrière de la *MMT-O* dans le polyéthylène.

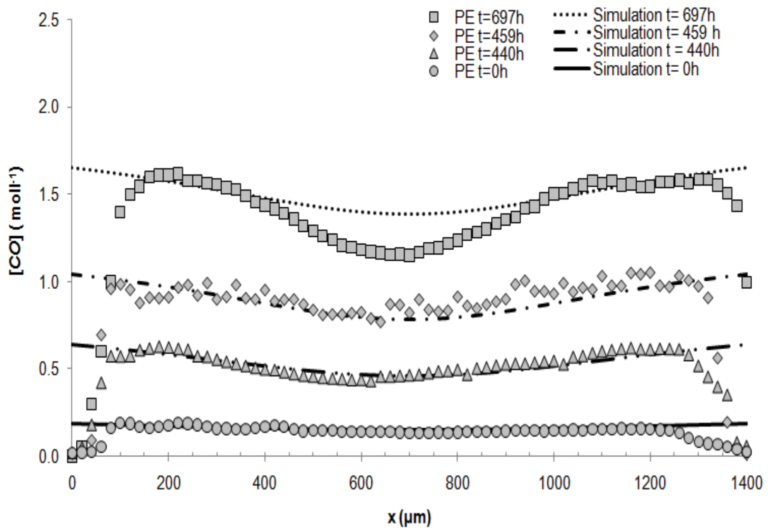

Profiles d’oxydation expérimentales et simulés pour le pure *PE* après d’une exposition à 100°C.

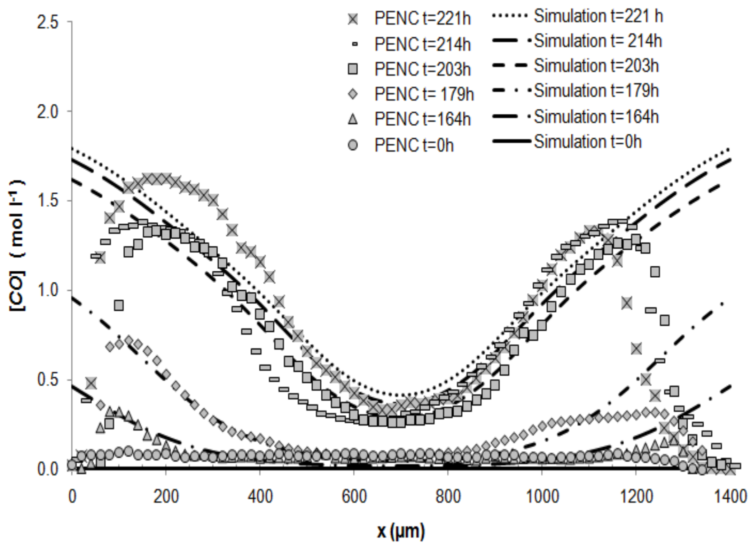

Profiles d’oxydation expérimentales et simulés pour le *PENC* après d’une exposition à 100°C.

Enfin le modèle cinétique est utilisé pour simuler les gradients de taux de cristallinité (*AED*) en couplant le modèle oxydation contrôlée par la diffusion et le modèle de chimicristallisation détaillée dans la première partie. En se basant sur un modèle reliant taux de cristallinité et module élastique, des profils de module dans l’épaisseur sont alors simulés et comparés à des résultats expérimentaux. L’accord raisonnable confirme alors notre approche.

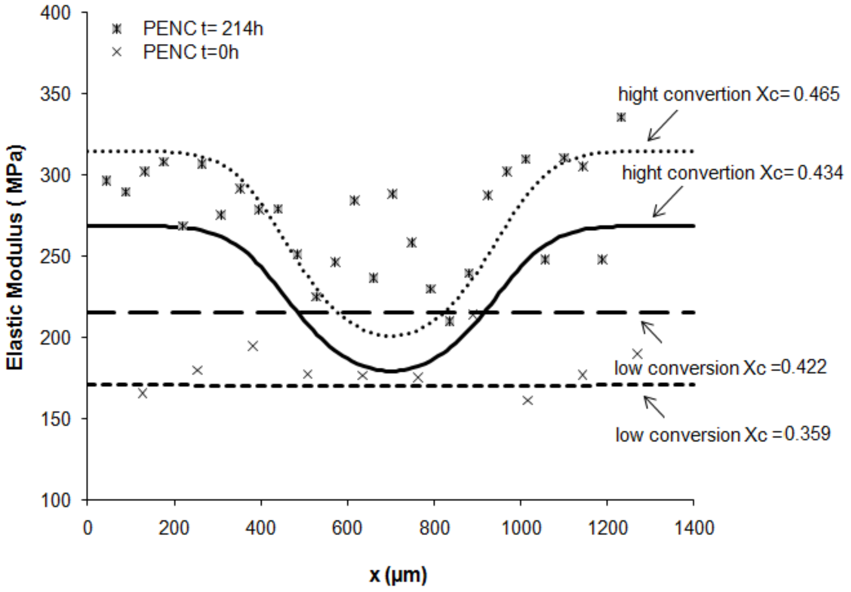

Profiles de module élastique expérimentales et simulés pour *PENC* non vieilli et pour *PENC* très dégradé après d'une exposition à 100°C

Chapter IV

Thermal Degradation of Clay Nanoreinforced Polyethylene

Thermo-oxidative degradation is a succession of several processes that lead to material embrittlement and fail. Polymer materials suffer gradual structural changes that go unnoticed until a critical state is attained. The initiator link of polymer degradation chain is the radicalary mechanism which generates alkyl and peroxyl radical species and progressively increases the carbonyl group (CO) concentration. Even at low conversion rates and slight network damage, degradation process entails an important action of chain scission (s) associated to a reduction of molar mass M_w: this result in the chemicrystallization of smaller polymer chains (X_c).

The purpose of this work is to explore the thermal degradation process of unstabilized clay nanoreinforced polyethylene at different morphologic scales. In order to obtain a complete description of the clay action in those different levels, individual steps were assembled. A better comprehension of effects caused by the clay insertion in the matrix degradation was attained by studying both homogeneous and heterogeneous oxidation process and applying a flexible and non empirical methodology.

Firstly, a material characterization was performed. Next, changes of molar mass, density, crystallinity ratio and oxygen permeability during homogeneous oxidation were studied. Finally, all these parts were put together when the heterogeneous oxidation was examined. As a result predictions of oxidation products distribution (oxidation profiles), crystallinity and elastic properties profiles were obtained when oxidation was coupled to the oxygen diffusion phenomena (Figure 26).

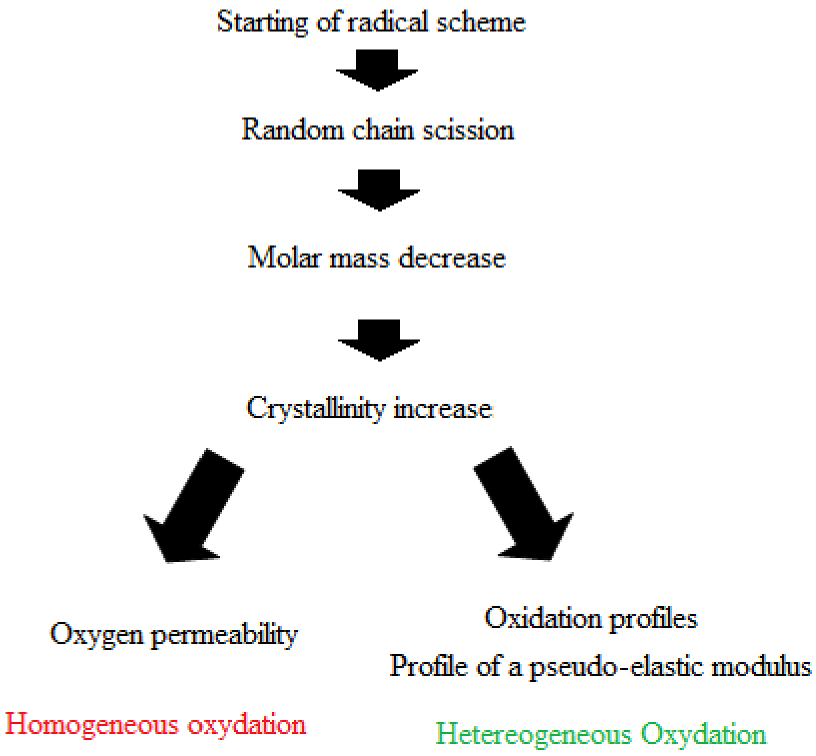

Figure 26 Methodology used studying thermal degradation of PE and PENC.

1. Initial Characterization

1.1 Fourier Transform Infra Red (*FTIR*)

Presence of montmorillonite modifies the polyethylene spectra by adding peaks. Figure 27 presents the *FTIR* spectra of the pure polyethylene (*PE*), organically modified clay (*MMT-O*) and those corresponding to the clay nanoreinforced polyethylene (*PENC*).

Five regions may be distinguished in the *MMT-O* spectra [150]: R1 (462-517 cm^{-1}): due to Al-O bonds. R2 (864-974 cm^{-1}): corresponding to asymmetric vibrations of the epoxy group C-O-C. R3 (1000-1150 cm^{-1}): coming from four Si-O bond vibrations [39]. R4 (1721-1798 cm^{-1}): this region is characteristic of the carbonyl group (C=O), specifically for carboxylic acids resulting from hydrolysis reactions of the clay organic modification [110]. R5 (3581-3729 cm^{-1}): characteristic region of the hydroxyl group (O-H), alcohols and phenols compounds.

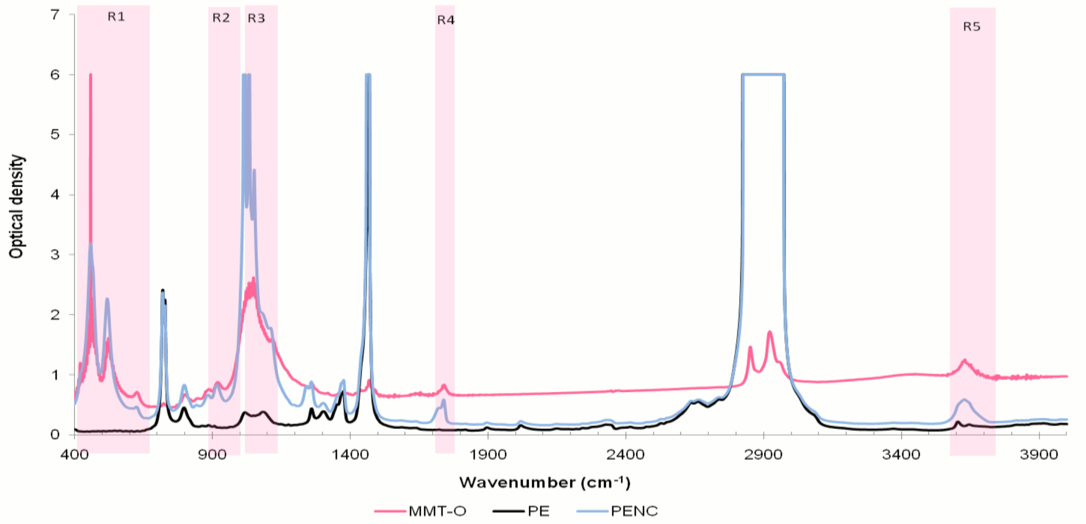

Figure 27 ***FTIR*** **characteristic spectra of** ***PE*****,** ***MMT-O*** **and** ***PENC*****.**

1.2 Wide Angle X- Ray Diffraction (*WAXS)*

Characterization of the clay nanocomposite morphology is often performed by combining two complementary techniques such as transmission electronic microscopy and *X*- ray diffraction [35]. The latter permits determining the distance between crystalline structures by the principle of constructive interference. In this case, the basal distance d_0 was of 2.7nm and the separation between clay sheets in the composite was equal to 3.09 nm (Figure 28). These results indicate that the mixing induce to an intercalation/exfoliation morphology. However, the best method to check this hypothesis is to observe directly the composite dispersion and distribution at a nanometer scale by using transmission electronic microscopy (see below).

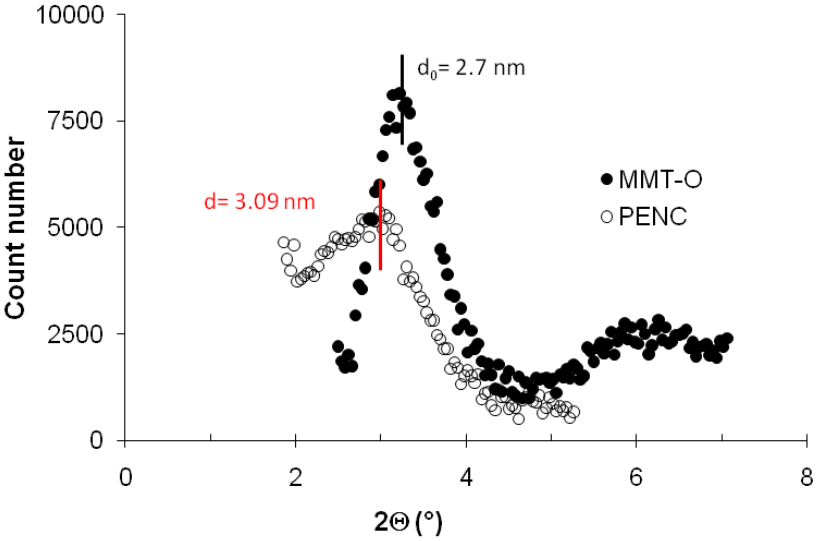

Figure 28 WAXS results for the clay basal space (*d_0*) and the distance between clay sheets in the nanocomposite (*d*).

1.3 Scanning Transmission Electronic Microscopy (*STEM*)

Samples for *STEM* tests required careful preparation. In order to obtain very thin layers of about 50nm, nanocomposite films were cryo- ultramicrotomed. Figure 29 shows a general view of the nanocomposite morphology: there was no a homogeneous dispersion of the clay in the matrix, on the contrary several clay clusters (dark regions) could be identified. High magnification images permitted to discover some individual clay sheets dispersed more or less randomly as well as several clay layers forming small stacks of 150-400nm and reaching a thickness of 60nm thick (Figures 30 and 31).

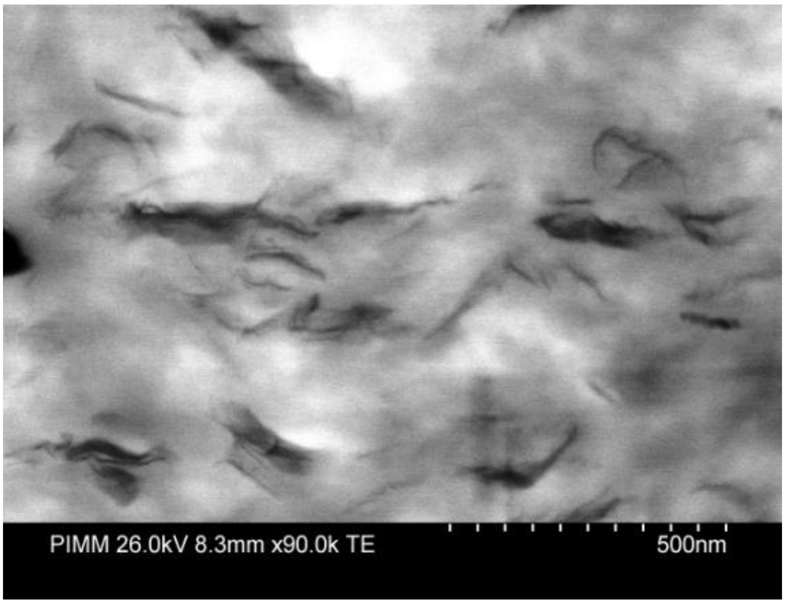

Figure 29 Low magnification *STEM* image of a film section: nanoclay dispersion. 90,000X photograph.

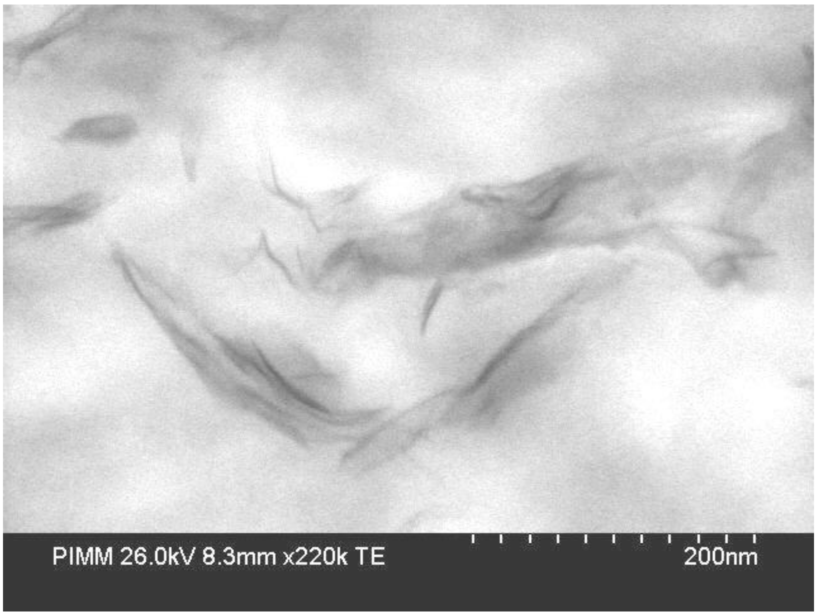

Figure 30 High magnification *STEM* image of a film section: nanoclay dispersion. 220,000X photograph.

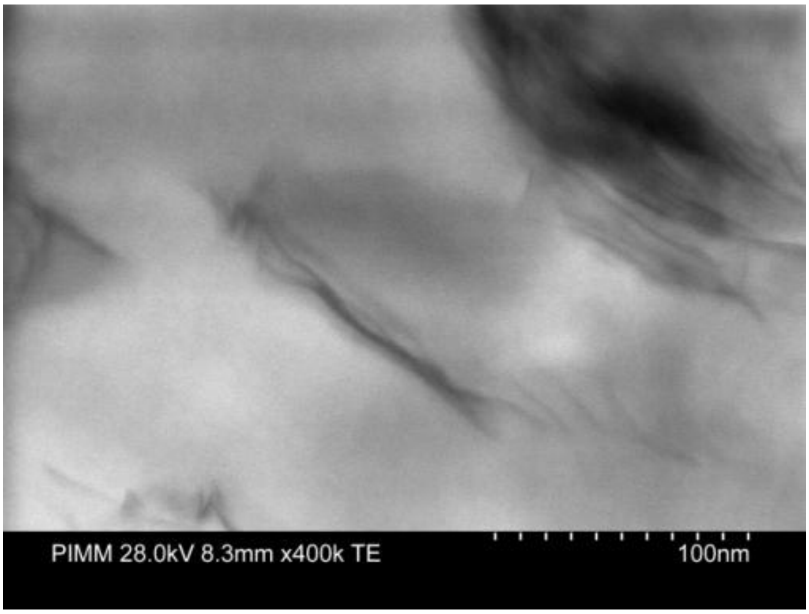

Figure 31 High magnification *STEM* image of a film section: nanoclay dispersion. 400,000X photograph.

Figure 32 displays a highly-magnified pile end revealing stack thickness of above 20.5nm and clay-clay distances ranging between 1.4 and 3.23 nm. The average *MMT-O* aspect ratio calculated based on all collected *STEM* images was 14.8.

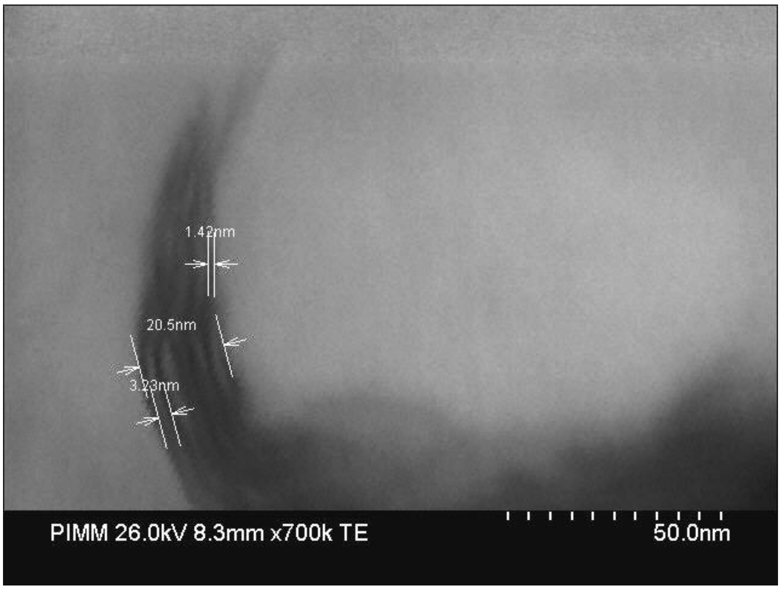

Figure 32 Very high magnification *STEM* image of a film section: nanoclay dispersion. 700,000X photograph.

As a conclusion, it can be said that the intercalate morphology was the dominant state and small quantity of polymer chains migrated into the clay gallery leading to a small splitting of clay layers.

1.4 Oxygen Diffusion

1.4.1. Effect of Temperature

Oxygen permeability tests were performed using 180- 280µm – thick films at 7°C, 23°C and 50°C. During testing, oxygen transmission rate (*OTR*) was tracked under isothermal conditions until it reached a stationary state value. After the stabilization of the *OTR*, the test was stopped. Experimentally, permeability values (P_{O2}) were calculated to the ratio between the final *OTR* value and the sample thickness.

Figure 33 presents the permeability results for both *PE* and *PENC* materials at the three studied temperatures. Contrary to literature data - where permeability decreases between 27% and 47% are reported for polyethylene /clay nanocomposites [53, 151,152]- it was found a maximal permeability decrease of 10% was found when clay was present in the system (*PENC*). These results indicated that no improvements on material oxygen barrier properties related to the clay were present in the system.

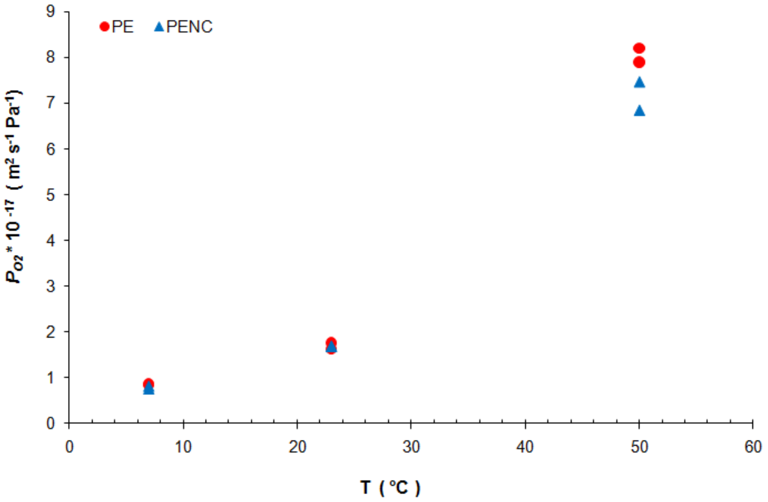

Figure 33 Oxygen permeability variations with temperature at 7°C, 23°C and 50°C for *PE* and *PENC.*

Oxygen diffusion coefficients (D_{O2}) were also obtained for *PE* and *PENC* at 7°C, 23°C and 50°C applying Henry's law (Equation 1), where P_{O2} is the oxygen permeability and S_{O2} is the oxygen sorption coefficient.

$$D_{O2} = \frac{P_{O2}}{S_{O2}} \qquad (1)$$

As in the polypropylene case (Chapter III), for the polyethylene system it was assumed that no variation of S_{O2} is induced by the clay presence and $S_{O2PE} = S_{O2PENC} = S_{O2}$. Furthermore, it was experimentally explored the changes of such coefficient with the exposure temperature at 7°C, 23°C and 50°C: the S_{O2} activation energy for the pure polyethylene was 20 kJ mol^{-1} and for the *PENC* was 14 kJ mol^{-1}. Based on this slight difference between both materials, it was assumed that the sorption coefficient does not change with the temperature. The value of S_{O2} was the same for both *PE* and *PENC* for exposure temperatures between 7°C and 100°C, such value fixed at 6.45 10-6 mol l^{-1}Pa^{-1} correspond to the average of S_{O2} measured value for *PE* and *PENC* at the three studied temperatures.

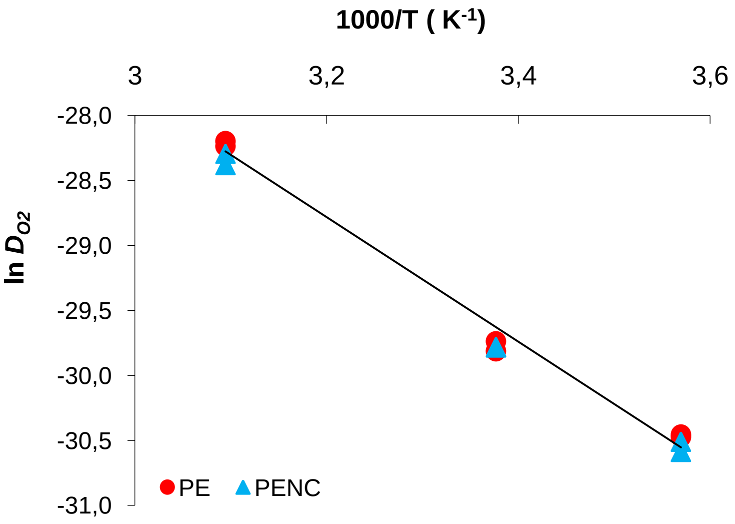

Figure 34 Arrhenius behavior of the oxygen diffusion coefficient of *PE* and *PENC* between 280 and 323 K.

Finally, based on the Arrhenius linear behavior of $D_{O2,}$ values of these coefficients for *PE* and *PENC* at 100°C may be calculated and used as first approach values when oxygen diffusion is coupled with oxidation (heterogeneous degradation, section 3 of this chapter). According to Figure 34, $E_{a\ DO2PE}$ = 39.84 kJ mol^{-1}, $E_{a\ DO2PENC}$ = 38.99 kJ mol^{-1}, $D_{O2\ \mathrm{0PE}}$= 1.45 10^{-6} and $D_{O2\ \mathrm{0PENC}}$= 9.59 10^{-7}. The extrapolated values of $D_{O2\ \mathrm{PE\ 100°C}}$ and $D_{O2\ \mathrm{PENC\ 100°C}}$ were 2.86 10^{-12}m^{2}s^{-1} and 2.51 10^{-12} m^{2}s^{-1} respectively.

1.4.2. Effect of the Filler

Figure 35 displays the behavior of the ratio between composite and pure matrix permeabilities in function of the clay aspect ratio. Nielsen's model - in which very thin impermeable rectangular layers are homogeneously dispersed perpendicularly to the flux of permeant - does not describe our system since it does not correspond exactly to the dilute regimen characteristics [45] (Chapter I, section 1.7.1.2, equation 6). Even if the clay quantity is lower than 10%v its aspect ratio equal to 14.8 (determined from *STEM* photographs) is quite small. Inversely, the behavior exhibited by our system corresponded to the first part of the curve delineated by the Cussler model (randomly oriented circular layers having a gas permeability driven by the tortuosity factor and pore constrictions). The aspect ratio predicted by the Cussler model for the nanocomposite permeabilities measured in our system is about 7. This value is closer to the aspect ratio values ranged between 5.5 and 10.6 reported in the literature for a $LLDPE / LLDPE - g - MAH$ / montmorillonite composites fabricated by the melt state method [53].

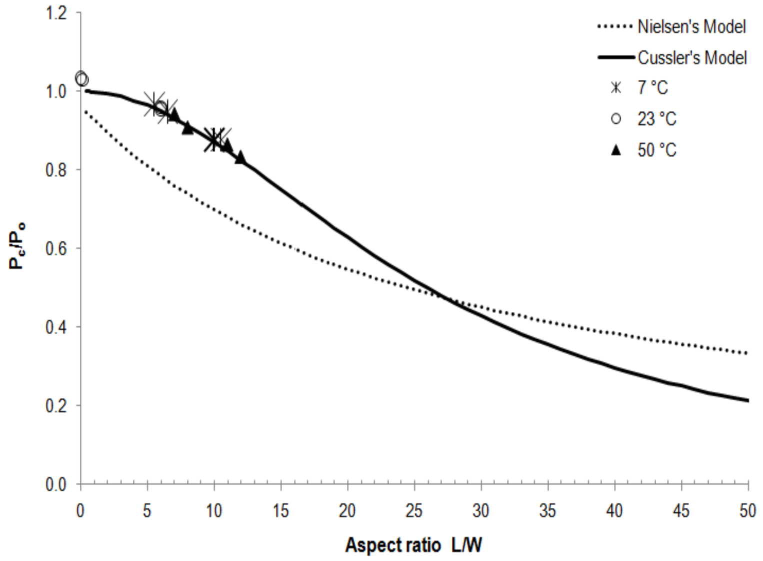

Figure 35 Models used to describe improvements of oxygen permeation in clay/ polymer nanocomposites.

These results confirmed *STEM* and *WAXS* results from which was deduced that the clay in our system did not reach an exfoliated configuration: during the composition step clay layers neither split nor crushed, consequently there was no effective dispersion and the length of the sheets remained almost unchanged. Moreover, polymer chains did not massively enter into the interlayer spaces allowing clay layers to remain together forming stacks that will not contribute effectively with improving the matrix oxygen permeability. This behavior corresponds well to the results obtained from oxygen permeability measurements between 7°C and 50°C.

2. Homogeneous Thermo-oxidation – Thin Films

This section deals with the thermal oxidation of pure polyethylene *PE* and clay polyethylene nanocomposite *PENC* when oxygen diffusion limitations are not present and degradation process can be considered homogeneous. Several aspects were studied in order to get a better comprehension and a complete perspective of changes and modifications happening during degradation at molecular (sections 2.1.1 to 2.2.1), morphologic (section 2.2.2) and macroscopic scales (sections 2.2.3 to 3.3).

2.1. Oxidation Kinetics

The thermo-oxidation kinetics was studied by following changes of the carbonyl average concentration ($[CO]_{av}$) with time by *FTIR* measurements. Using 160 – 180µm thick films a homogeneous degradation process could be expected considering the thickness of the films [81].

2.1.1. Carbonyl building up

Oxidation curves of *PE* and *PENC* at 60°C, 80°C and 100°C represented as the changes of carbonyl average concentration $[CO]_{av}$ with time are presented in Figure 36. All curves have a similar aspect: in a first moment no significant increase of $[CO]_{av}$ is detected. After certain time (t_i) an auto acceleration region is observed where average carbonyl concentration rapidly increases at almost constant rate. At the three studied temperatures, a decrease of the induction time (t_i) can be witnessed when clay is present in the system. Furthermore, the oxidation rate (r_s) of the nanocomposite was at least three times faster than the oxidation rate corresponding to the pure matrix exposed under the same conditions. Induction time and oxidation rate values are reported in Table 11 at 60°C, 80°C and 100°C for *PE* and *PENC*.

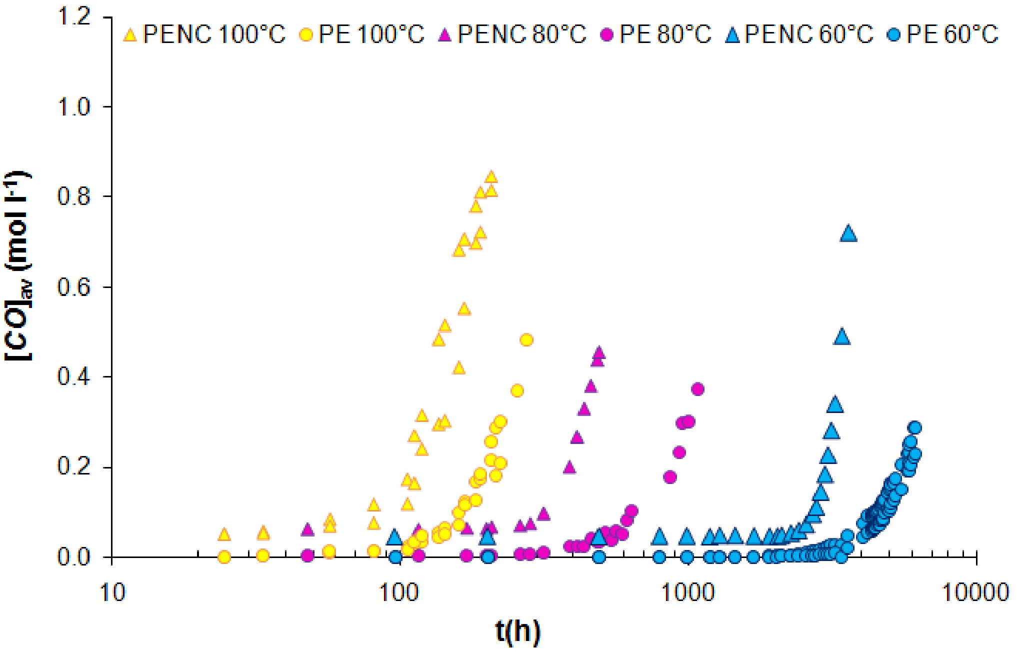

Figure 36 Experimental kinetics of pure polyethylene *PE* and its nanocomposite *PENC* (6.8%w clay) at 60°C, 80°C and 100°C.

T (°C)	$t_{i\ PE}$ (h)	$t_{i\ PENC}$ (h)	r_s *PE* (mol l^{-1} h^{-1})	r_s *PENC* (mol l^{-1} h^{-1})
60	3000	1900	1.0 10^{-4}	9.0 10^{-4}
80	490	250	6.0 10^{-4}	24.0 10^{-4}
100	120	60	25.5 10^{-4}	71.5 10^{-4}

Table 11 Induction times (t_i) and oxidation rate (r_s) of *PE* and *PENC* at 60°C, 80°C and 100°C.

Figure 37 illustrates the non – Arrhenian behavior of the induction time for pure *PE* and composite *PENC* at the three studied temperatures. It can be seen that experimental results correspond well with available literature data for polyethylene thermal degradation [140,153, 154,155,156,157,158,159,160] . Finally, our results confirmed that induction time values follow a non Arrhenian behavior.

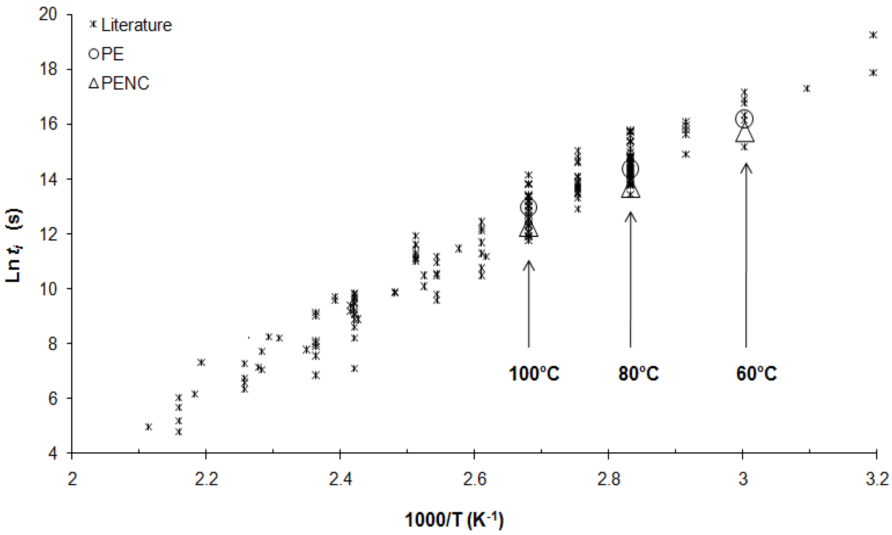

Figure 37 Non -Arrhenius behavior of the induction time (t_i) at 60°C, 80°C and 100°C for the pure polyethylene *PE* and the nanocomposite *PENC*.

Furthermore, values of degradation rate in logarithm scale (Ln r_s) versus 1000/T for both materials at the three temperatures were graphically confronted to those reported in literature (Figure 38). It can be seen that even if r_s values for the nanocomposite corresponded to a general behavior showed in literature for pure *PE*, it remained faster than $r_{s\ PE}$ since the latter presented a slower degradation rate than reported in the literature for pure *PE*.

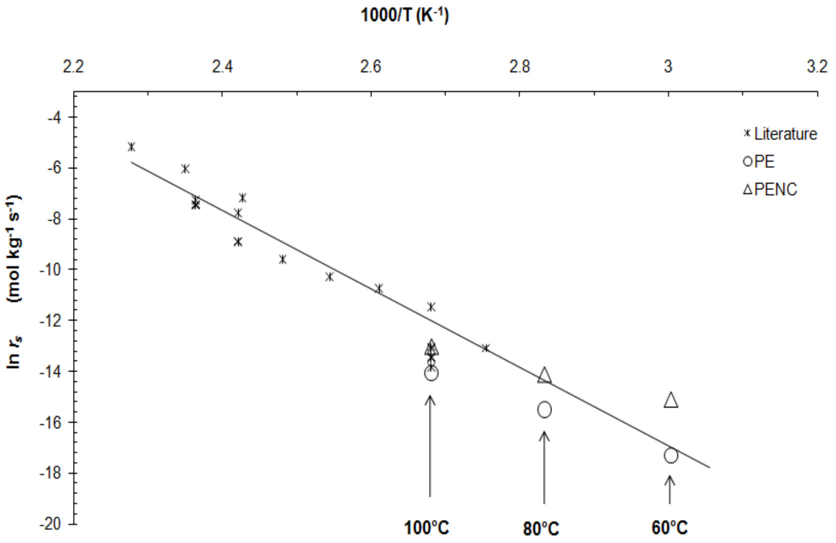

Figure 38 Comparison of ln r_s versus 1000/T for *PE* and *PENC* with literature data for polyethylene.

Based on these results, the catalytic effect of the montmorillonite was proven: it not only reduces the induction time but simultaneously speeds up the oxidation rate. Hence, a catalytic effect must be included in the kinetic mechanism in order to integrate degradation features that the montmorillonite confers to the system. This catalytic effect can be represented either by taking a different initial concentration of hydroperoxyde ($[POOH]_{0\ \text{matrix}} \neq [POOH]_{0\ \text{composite}}$) or by adding a catalytic reaction.

Contrary to the polypropylene case (Chapter III) - where *MMT-O* played a catalytic role represented from a simulation point of view by a difference between the initial hydroperoxide concentration ($[POOH]_{0\ \mathrm{PP}} \neq [POOH]_{0\ \mathrm{NCPP}}$) - montmorillonite induces supplementary changes in the polyethylene system. This additional difficulty related to an important decrease of the induction time is coupled to the degradation rate speeding up. In the polyethylene case it resulted impossible to simultaneously describe both effects by only varying $[POOH]_0$.

The optimized value of $[POOH]_{0\ PE} = [POOH]_{0\ PENC} = [POOH]_0$ was equal to 1.0 10^{-4} mol l^{-1}. Figure 39 presents a parametric study of the $[POOH]_0$ using extreme values of the estimated interval for the $[POOH]_0$ values proposed by Rincon et al [85], changes corresponding to values one decade below and one decade above of the optimized $[POOH]_0$. A very slight effect was induced by $[POOH]_0$ changes, meaning that $[POOH]_0$ is not a key factor in the system and an additional fitting parameter is needed when the clay is present in the system.

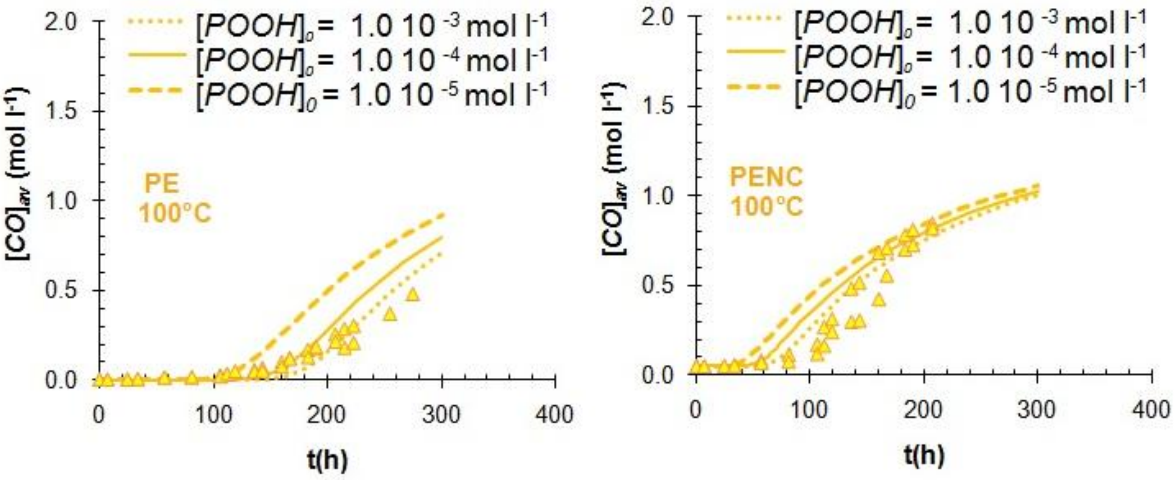

Figure 39 Parametric study of $[POOH]_0$ on the oxidation kinetics of the pure *PE* and the nanocomposite *PENC* at 100°C.

In order to describe the kinetic behavior of both *PE* and *PENC*, the optimized value of $[POOH]_0$ was fixed as a common parameter for both materials and a catalytic reaction induced by the iron particles [161] contained in the clay was included (Equation 4):

$$POOH + M^{n+} \rightarrow PO^{\bullet} + M^{(n+1)+} + HO^{-} \quad (2)$$

$$POOH + M^{(n+1)} \rightarrow POO^{\bullet} + M^{n+} + H^{+} \quad (3)$$

$$POOH + POOH \rightarrow PO^{\bullet} + POO^{\bullet} + H_2O \quad (4)$$

2.1.2. Kinetic Modelling

The kinetic scheme used in this work in order to model the thermal degradation of the pure and clay nanoreinforced polyethylene was the Closed Loop Model (*CLM*) [162,163]. Among the basic chemical reactions of the *CLM* [81] unimolecular and bimolecular initiation, propagation and termination), the reaction related to a catalytic initiation (Im) induced by the montmorillonite was included. The rate constants k_{1u}, k_{1b}, k_2, k_3, $k_{4,}$ k_5, $k_{61,}$ $k_{62,}$ and k_{61}correspond to reactions I to VI. The kinetic constant of the initiation reaction Im is k_{1m} : it was set to zero for the pure polyethylene.

Initiation reactions

$$POOH \rightarrow 2P^{\bullet} \qquad k_{1u} \qquad (Ia)$$

$$2POOH \rightarrow P^{\bullet} + PO_2^{\bullet} \qquad k_{1b} \qquad (Ib)$$

$$2POOH \rightarrow P^{\bullet} + PO_2^{\bullet} \qquad k_{1m} \qquad (Im)$$

Propagation reactions

$P^{\bullet} + O_2 \rightarrow PO_2^{\bullet}$ k_2 (II)

$PO_2^{\bullet} + PH \rightarrow POOH + P^{\bullet}$ k_3 (III)

$P^{\bullet} + P^{\bullet} \rightarrow Inactive \quad products$ k_4 (IV)

$P^{\bullet} + PO_2^{\bullet} \rightarrow Inactive \quad products$ k_5 (V)

Termination reactions

$PO_2^{\bullet} + PO_2^{\bullet} \rightarrow \left[PO^{\bullet\bullet}OP\right]_{cage} + O_2$ k_{60} (VI-0)

$\left[PO^{\bullet\bullet}OP\right]_{cage} \rightarrow POOP$ k_{61} (VI-1)

$\left[PO^{\bullet\bullet}OP\right]_{cage} \rightarrow P = O + P - OH$ k_{62} (VI-2)

$\left[PO^{\bullet\bullet}OP\right]_{cage} \rightarrow 2P^{\bullet}$ k_{63} (VI-3)

In order to describe the production and accumulation of hydroperoxyde group $\left[POOH\right]$, $\left[POOP\right]_{cage}$, alkyl $\left[P^{\bullet}\right]$, peroxyl $\left[PO_2^{\bullet}\right]$ radicals and the consumption of subtract $\left[PH\right]$ a set of differential equations was derived from the proposed kinetic scheme:

$$\frac{d\left[PH\right]}{dt} = -2k_{1u}\left[POOH\right] - k_{1b}\left[POOH\right] - k_{1m}\left[POOH\right]^2 - k_3\left[PO_2^{\bullet}\right]\left[PH\right] \tag{5}$$

$$\begin{aligned} \frac{d\left[P^{\bullet}\right]}{dt} = {} & 2k_{1u}\left[POOH\right] + k_{1b}\left[POOH\right]^2 + k_{1m}\left[POOH\right] \\ & - k_2C_s\left[P^{\bullet}\right] + k_3\left[PO_2^{\bullet}\right]\left[PH\right] - 2k_4\left[P^{\bullet}\right]^2 - k_5\left[P^{\bullet}\right]\left[PO_2^{\bullet}\right] + 2k_{63}\left[PO_2^{\bullet}\right]^2 \end{aligned} \tag{6}$$

$$\begin{aligned} \frac{d\left[PO_2^{\bullet}\right]}{dt} = {} & k_{1b}\left[POOH\right]^2 + k_{1m}\left[POOH\right]^2 \\ & + k_2C_s\left[P^{\bullet}\right] - k_3\left[PO_2^{\bullet}\right]\left[PH\right] - k_5\left[P^{\bullet}\right]\left[PO_2^{\bullet}\right] - 2k_{60}\left[PO_2^{\bullet}\right]^2 \end{aligned} \tag{7}$$

$$\frac{d[POOH]}{dt} = -k_{1u}[POOH] - 2k_{1b}[POOH]^2 + k_3[PO_2^{\bullet}][PH] - 2k_{1m}[POOH]^2 \quad (8)$$

$$\frac{d[POOP]_{cage}}{dt} = k_{60}[PO_2^{\bullet}]^2 - (k_{61} + k_{62} + k_{63})[POOP]_{cage} \quad (9)$$

The initial values used to solve this system were:

$[PH] = [PH]_0$ $[PO_2^{\bullet}]_0 = [P^{\bullet}]_0 = 0$

$[POOH] = [POOH]_0$, $[O_2] = [O_2]_s$

$[PH]_0$ and $[O_2]_s$ are the initial concentrations of the $[PH]$ *and* $[O_2]$ species respectively.

The link between simulation and experimental results was done by using the average carbonyl concentration $[CO]_{av}$, which was the variable experimentally tracked on time. Analytically, $[CO]_{av}$ may be calculated from the decomposition of hydroperoxides by using the expression[164]:

$$\frac{d[CO]_{av}}{dt} = \left[k_{1u}[POOH] + k_{1b}[POOH]^2 + k_{1m}[POOH]^2\right]\left[1 - MMT - X_c\right] \quad (10)$$

Since crystalline ratio is considered as an inert phase to the oxidation process, the correction term $1 - MMT - X_c$ correction was included in equation 10. In this first part of the study (homogenous degradation), crystalline ratio was considered constant .In section 3 - dedicated to the study of heterogeneous features of oxidation - the crystalline ratio was considered as a variable quantity and was included in the differential system (*CLM*) in order to describe its changes with time .

Figure 40 presents a superposition of experimental and simulation curves of the *PE* and *PENC* thermal degradation kinetics. For the three temperatures the hydroperoxyde initial concentration was set to 1.0 mol l^{-1} and the catalytic reaction was characterized by the rate constant k_{1m}. In all cases simulations described the general behavior of both materials: they draw the inflection point associated to the induction time as well as the auto accelerated part of the curves.

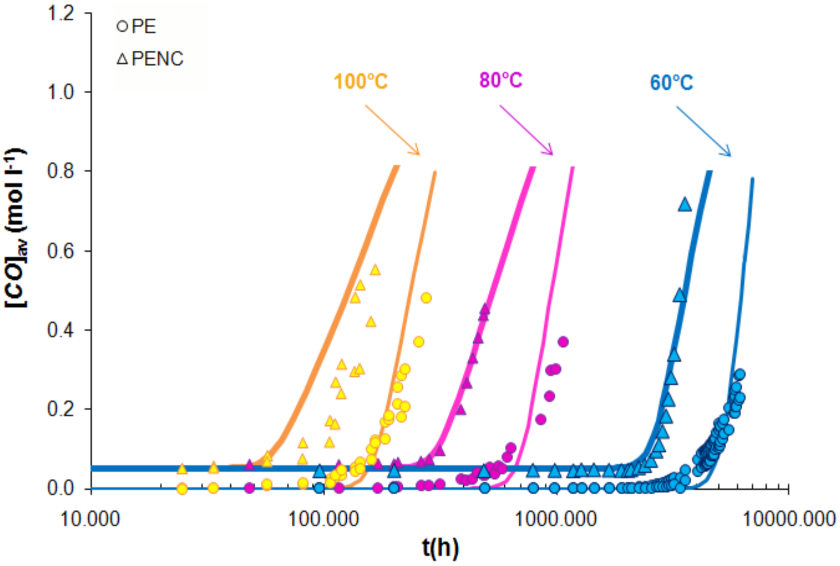

Figure 40 Superposition of experimental and simulated curves at 60°C, 80°C and 100°C for *PE* and *PENC*.

A verification of the model sensibility regarding k_{1m} was performed through a parametric analysis at 60°C, 80°C and 100°C varying from one magnitude order the optimized k_{1m} value (Figure 41). It can be observed that small changes of the k_{1m} parameter affect the shape of the simulated curve.

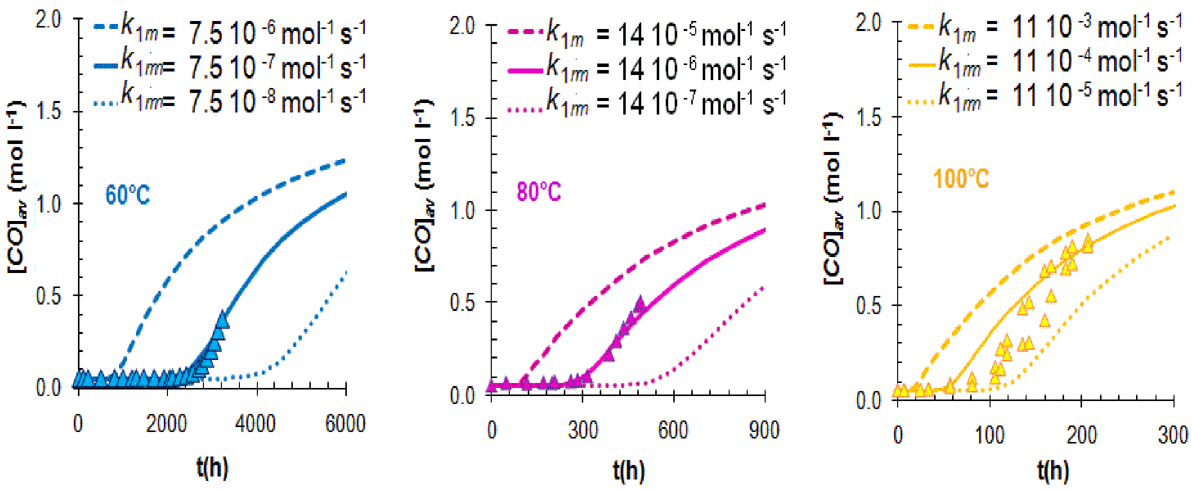

Figure 41 Parametric analysis of k_{1m} at 60°C, 80°C and 100°C.

Assuming that k_{1m} keeps an Arrhenius behavior similarly to all the used kinetic parameters, the associated activation energy ($E_{a\ k1m}$) and its pre-exponential factor (k_{m0}) were calculated. The value of $k_{1m0} = 1.49\ 10^{14}$ l $\text{mol}^{-1}\text{s}^{-1}$ and $E_{a\ k1m}$ *was* 130 kJ mol^{-1}. This fact confirmed the initial assumption made in order to deal with the catalytic action induced by iron particles contained in the montmorillonite, in which two consecutive unimolecular reactions were needed (Chapter I, Equations I_{m1} and I_{m2}). These partial reactions were included in the kinetic model by using their equivalent pseudo-bimolecular catalytic global reaction (Chapter I, Equation I_m) which only takes place during the initiation stage. Since $E_{a\ k1m}$ is slower that the activation energy associated to two unimolecular initiation reactions (I_{m1} and I_{m2} with $E_{a\ 1m1} + E_{a\ 1m2} \approx 280$ kJ mol^{-1}) it can be said that Im reduced the initiation process activation energy.

In order to explore the catalytic power associated to iron particles present in the clay, its relative degradation rate was compared with respect to those of the unimolecular and bimolecular initiations (Figure 42). Degradation rates were calculated as:

$$r_{s\ \mathrm{unimolecular}} = k_{1u}\,[POOH] \tag{11}$$

$$r_{s\ \mathrm{bimolecular}} = k_{1b}\,[POOH]\,[POOH] \tag{12}$$

$$r_{s\ \mathrm{metallic}} = k_{1m}\,[POOH]\,[POOH] \tag{13}$$

where, k_{1m} is associated to the active Fe^{+2} and Fe^{+3} particles released from the clay gallery into the matrix during the nanocomposite composition.

Firstly, it was observed that bimolecular initiation rate was dominant between 60°C and 80°C. Starting at 80°C the metallic catalysis gains importance and induces a faster degradation rate compared to those related to unimolecular and bimolecular initiation. Lastly, it can be seen that under each thermal condition the composite induction time (Table 11) globally corresponds to the time when the slowest initiation reaction attains a stationary rate.

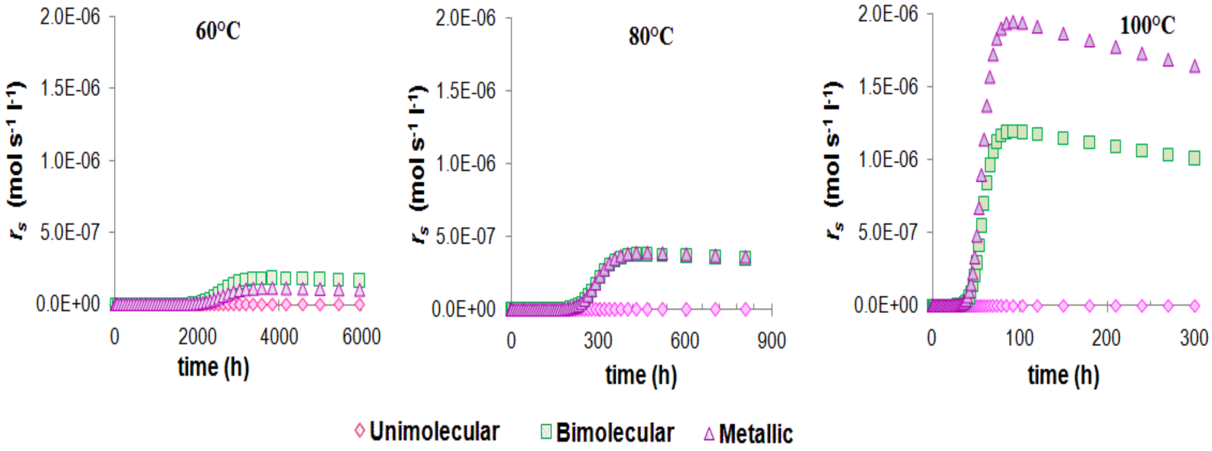

Figure 42 Relative degradation rate of the unimolecular, bimolecular and metallic initiation reactions in the nanocomposite with 6.8%w clay at 60°C, 80°C and 100°C.

The pre-exponential factor and the activation energy values for the kinetic constant set of the pure polyethylene were reported by Khelidj N [163]. The values of k_{1u}, k_{1b}, *and* k_2 initially found by an inverse method [104,163] were corrected according to our experimental data. Those set of kinetic parameters calculated at 60°C, 80°C and 100°C were completed by adding the catalytic reaction (Im) and its correspondent speed constant k_{1m} determined by an inverse method. The parameter values used in the *CLM* to model the thermal degradation of the pure polyethylene and its clay nanocomposite at any temperature are shown in Tables 12 and 13.

	$[PH]_0$ (mol l^{-1})	$[POOH]_0$ (mol l^{-1})	***MMT-O*** (%w)
PE	60	$1.0\ 10^{-4}$	0
PENC	60	$1.0\ 10^{-4}$	0.068

Table 12 Initial concentrations of subtract, hydroperoxyl and clay used for the simulation of *PE* and *PENC* thermal behavior.

Constants	**Pre-exponential factor (s^{-1} or mol^{-1}s^{-1})**	**E_a (kJ mol^{-1})**
k_{1u} (s^{-1})	$8.0\ 10^{10}$	140
k_{1b} (l mol^{-1} s^{-1})	$2.9\ 10^{10}$	108
k_{1m} (l mol^{-1} s^{-1})	$1.5\ 10^{14}$	130
k_2 (l mol^{-1} s^{-1})	$1.0\ 10^{8}$	0
k_3 (l mol^{-1} s^{-1})	$3.0\ 10^{10}$	73
k_4 (l mol^{-1} s^{-1})	$8.0\ 10^{11}$	0
k_5 (l mol^{-1} s^{-1})	$1.5\ 10^{12}$	5.9
k_{60} (l mol^{-1} s^{-1})	$4.9\ 10^{19}$	80
k_{61} (l mol^{-1} s^{-1})	$2.0\ 10^{6}$	0
k_{62} (l mol^{-1} s^{-1})	$1.2\ 10^{6}$	5
k_{63} (l mol^{-1} s^{-1})	$8.0\ 10^{12}$	50

Table 13 Kinetic constants for *PE* and *PENC* .

2.2. Process of Chemical Ageing

2.2.1. Molecular Scale

2.2.1.1. Molar Mass

Radical oxidation chain includes several chemical acts amongst which random chain scission and dehydrogenation are the main reactions taking part during the initiation and the termination steps [104]. Occurring in the amorphous phase, chain scission leads to randomly create lower mass polymer chains. Even if those structural changes are hardly detectable by titration or spectroscopy methods at low conversion degrees (< 1% monomer units consumed) they induce sudden macroscopic material embrittlement and fail [165]. Some authors have reported measurements of molar mass during degradation for unstabilized polyethylene [166] and polypropylene [120] presenting in all cases experimental evidence of molar mass decreases with time during pho-oxidation and thermo-oxidation process [167]. Such tendency corresponds to the observed molar mass general behavior for the pure polyethylene and for the composite *PENC* at 100°C (Figure 43).

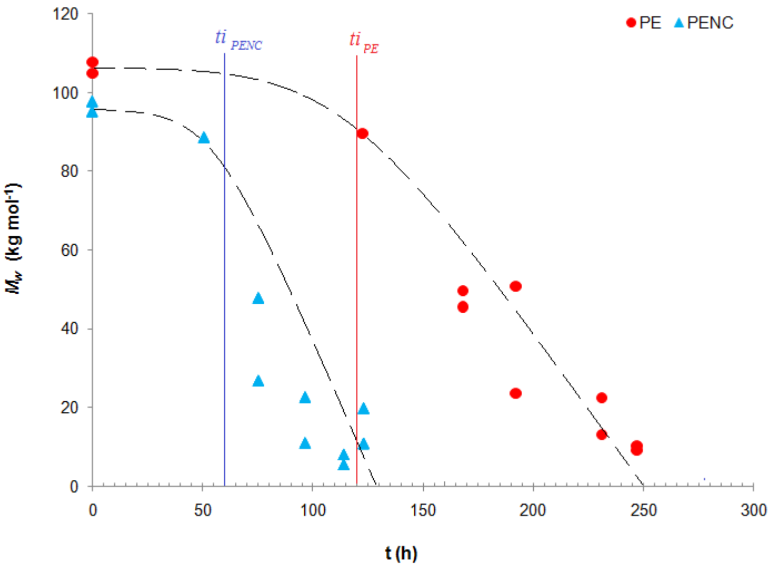

Figure 43 Molar mass M_w versus exposure time for *PE* and *PENC* samples at 100°C.

As expected, the behavior of the molar mass was similar for both materials: it decreases with time as oxidation process proceeds. It can be noticed that molar mass values are slightly slower for the nanocomposite compared to pure *PE* at the same *CO* concentration. Molar mass values vary from 106.3 kg mol^{-1} for the pure polyethylene and from 96.5 kg mol^{-1} for the nanocomposite. This discrepancy can be explained by the GPC sample preparation: for the *PENC* a pre - filtering step were the longest polymer chains can be removed is needed. According to Figure 43, average molar weight mass values reached a common value of 10 kg mol^{-1} after 247 hours and 123 hours for *PE* and *PENC*, respectively. This value of 10 kg mol^{-1} was lower than those corresponding to the polyethylene critical molar mass for embrittlement [168].

Additionally, the polydispersity index calculated as the molar mass in weight (M_w) divided by the molar mass in number (M_n) decreases with time and exhibits unimodal distribution which is distinctive of a homogeneous chain scission process [58,120,165,169] (Figure 44).

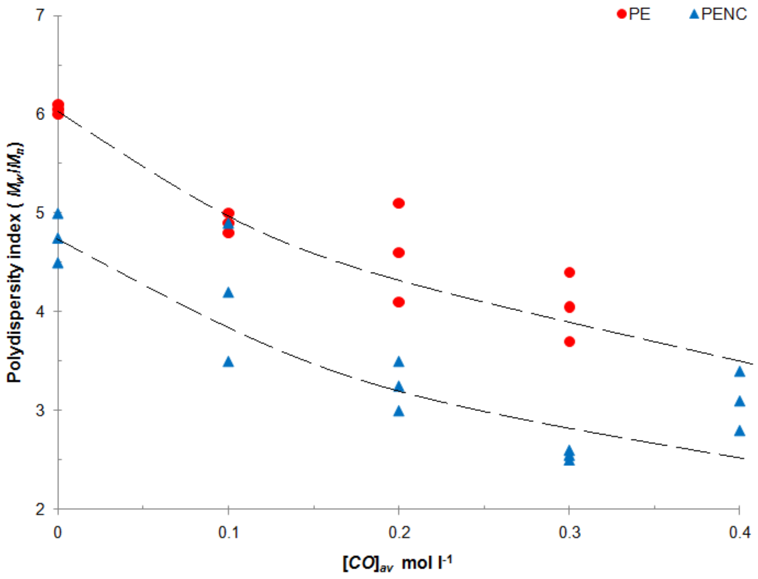

Figure 44 Polydispersity index changes with time represented by the carbonyl concentration of *PE* and *PENC* at 100°C.

2.2.1.2. Chain Scission

Since oxidation process can be considered as homogeneous, the number of associated chain scissions number (*s*) may be determined by using molar mass changes with time :

$$s = 2\left(\frac{1}{M_w} - \frac{1}{M_{w_0}}\right) \tag{14}$$

where, M_{w0} is the polymer molar mass at time zero, M_w is the polymer molar mass at a time t and s has units of mol kg^{-1}.

Assuming that random chain scission is predominant in polyethylene [170] and that the main scission process is due to β-scission of alkoxyl radicals, each reaction involving PO° radicals produce chain scissions [72]. Figure 45 presents the changes of chain scission number per unit with time for *PE* and *PENC*. Calculated chain scission values for the pure *PE* and the *PENC* displayed similar behavior: chain scission became suddenly important after about 60 hours for the *PENC* and 120 hours for the pure *PE* which corresponds to the end of their induction time at 100°C. This fact confirmed the prevalence of the chain scission process compared to cross linking process during the initiation and termination steps.

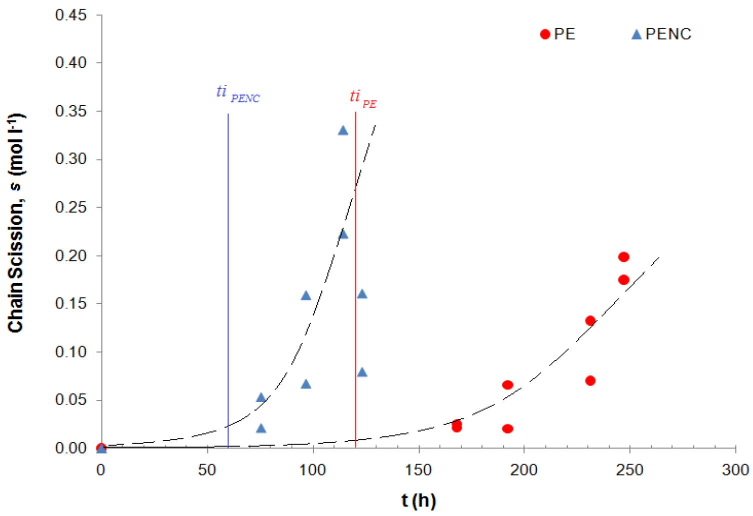

Figure 45 Changes of chain scission number per mass (*s*) with exposure time at 100°C for *PE* and *PENC*.

As a conclusion, it can be said that the chain scission process happens in the same way in the pure polyethylene and in the matrix of the nanocomposite. Clay does not affect the homogeneity of the molecular process of random chain scission since the rate of chain scission was experimentally determined as 0.5 for both materials (Figure 46).

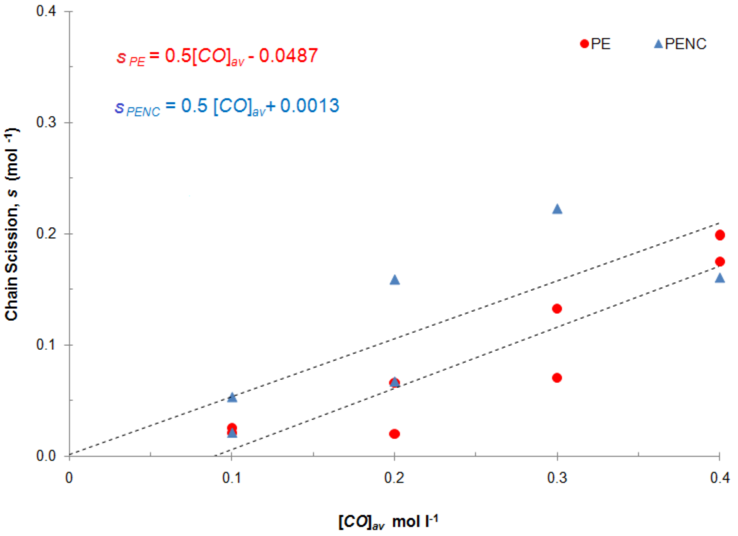

Figure 46 Changes of the chain scission number per mass with the carbonyl concentration for the pure *PE* and its composite *PENC* exposed at 100°C.

2.2.1.3. Prediction of the chain scission with time

Using the proposed kinetic model - particularly the initiation and termination reactions where the chain scission process was dominant (reactions I_{1u}, I_{1b} and VI-2) - the chain scission number per mass can be predicted as:

$$\frac{ds}{dt} = \begin{bmatrix} \gamma_s k_{1u}[POOH] + k_{1b}[POOH]^2 \\ \qquad + k_{1m}[POOH]^2 + k_{62}[POOP]_{cage} \end{bmatrix} [1 - MMT - X_c] \tag{15}$$

where, γ_s corresponding to the chain scission efficiency factor equal to 0.35 was assessed by an inverse method(see more related details in section 2.2.2.5).

Figure 47 presents the predicted behavior of the chain scission number per mass for the pure *PE* and the nanocomposite *PENC* for an exposition at 100°C.

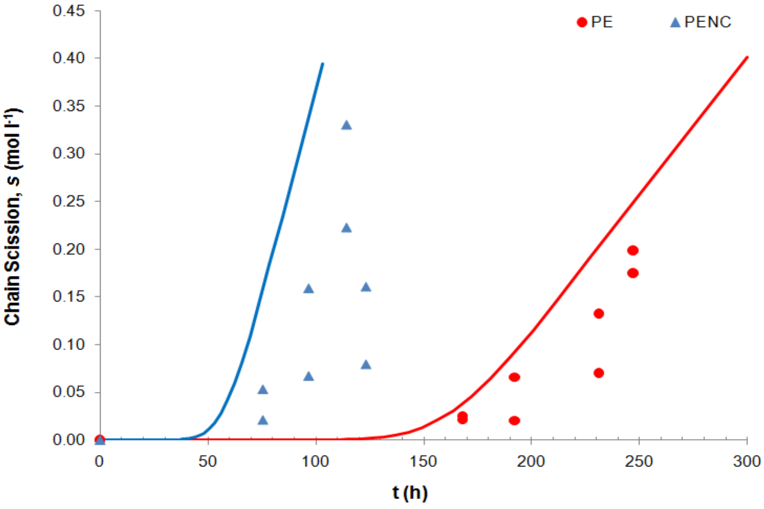

Figure 47 Prediction of the chain scission (*s*) changes for *PE* and *PENC* at 100°C.

As a result of the simulations for the pure *PE* and the nanocomposite *PENC* was obtained a general description of the chain scission process with time: the same shape of *s* function was obtained, but the moment in which *s* starts to rapidly increase was under estimated and *s* begins earlier than expected. This effect was less important for pure *PE* than it for *PENC*.

2.2.2. Morphological Scale

It is well known that in semi-crystalline polymers having their amorphous phase in rubbery state, oxidation process leads to a crystallinity increase [165]. These crystallinity changes are often called “chemicrystallization phenomenon”: smaller chains formed from the chain scission process taking place in the amorphous matrix, migrate to the crystalline phase to integrate lamellas through a secondary crystallization process [171,172,173]. As a result, the crystalline fraction increases over exposure time [165]. In the polyethylene case, experimental evidence obtained from Raman Low- frequency Acoustical Model (*LAM*) [174] and Small Angle X-ray diffraction (*SAXS*) [175,176] demonstrate that such crystallinity increase is associated to a lamella thickening.

Our aim here is to study the influence of *MMT-O* on the chemicrystallization process and to establish a physical link between this phenomenon with the kinetic modeling. From an experimental point of view, we propose as a first approach the use *DSC* and density measurement to follow crystallinity ratio changes.

2.2.2.1. Differential Scanning Calorimetry (*DSC*)

Figure 48 presents the crystallinity changes (X_c) measured by *DSC* for the pure *PE* and the *PE* in the composite *PENC* exposed at 100°C.

For both materials, crystallinity rapidly increased after their respective induction time (at 100°C) and nearly kept a constant rate until reaching a common crystalline fraction close to 0.5. It can be said that at 100°C such value corresponded to a crystalline equilibrium [165] where observed crystallization extend measured by *DSC* was maximal.

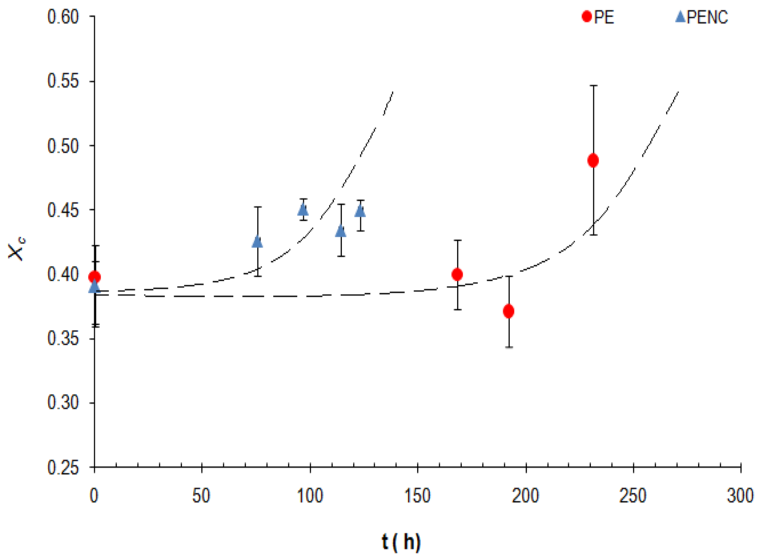

Figure 48 Variation of crystallinity content with time obtained from *DSC* tests for *PE* and *PENC*.

2.2.2.2. Density Measurements

Despite the fact that those morphological changes are hardly detectable at low conversions, variations of density of semicrystalline polymers may be accurately measured. In order to determine the density of the polyethylene in the nanocomposite, an expression was deduced through a density mixing law. The density of the polyethylene in the composite ($\delta_{PE\ in\ PENC}$) was estimated as:

$$\delta_{PE\ in\ PENC} = \frac{(1 - X_{clay})}{\left(\frac{1}{\delta_{PENC}} - \frac{X_{clay}}{\delta_{clay}}\right)} \tag{16}$$

where, $X_{clay} = 0.068$, $\delta_{clay} = 1800$ [kg m^{-3}] [177] , δ_{PENC} is the measured value.

Figure 49 presents the density values measured for different exposition times for pure polyethylene (*PE*) and the estimated density for the polyethylene in the composite (*PE in PENC*) for samples exposed at 100°C.

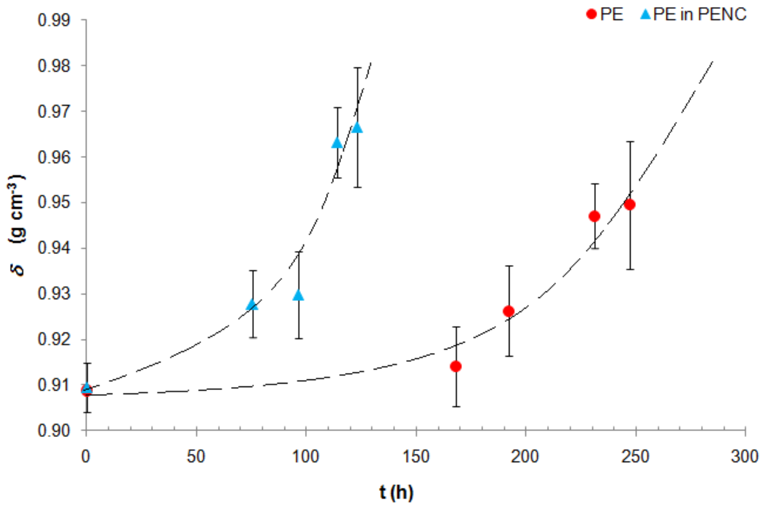

Figure 49 Density changes with time for the pure *PE* and *PE* in the nanocomposite *PENC* at 100°C.

Experimental results showed that the density of pure *PE* and *PE* in *PENC* increases with time. This behavior was similar to those exhibited by the *PE* in *PENC*. For an exposure at 100°C density varies from 0.91 g cm^{-3} to 0.99 g cm^{-3} for both polymers.

2.2.2.3. Discussion

The density of an oxidized sample could change in function of two aspects: the first is associated to the chemicrystallization phenomena in which the crystalline phase grows and being denser than the amorphous one, leads to a proportional augmentation of the sample density [165]. The second event is linked to gradual weight gains related to the number of oxygen atoms grafted to the polymer backbone as non volatile oxidation products remaining in the amorphous phase [178].

In order to differentiate chemicrystallization effects on the density increase from effects induced by an amorphous phase densification (by non volatile products) it was explored the impact caused by density changes on its associated crystalline extend. The relation to deduce an associated crystalline content to the measured density values (Equation 17) takes as reference the density value of the 100% crystalline (1 g cm^{-3}) [179] and the 100% amorphous polyethylene (0.85 g cm^{-3}) [165] as well as variation of density within exposition:

$$X_{c\ by\ \delta} = \left(\frac{\delta_{PE\ \ 100\%\ crystalline}}{\delta} \right) \left(\frac{\delta - \delta_{PE\ \ 100\%\ amorphous}}{\delta_{PE\ \ 100\%\ crystalline} - \delta_{PE\ \ 100\%\ amorphous}} \right) \tag{17}$$

Finally, apparent crystalline ratio ($X_{c\ by\ \delta}$) was corrected by the number of oxygen atoms correspondent to the typical polyethylene oxidation products such as ketones, alcohols, hydroperoxyls and carboxylic acids. This correction factor is equivalent to 0.63 for the polyethylene [178]. Figure 50 compares X_c with $X_{c\ by\ \delta}$ for the pure *PE* and the *PE* in the composite at 100°C.

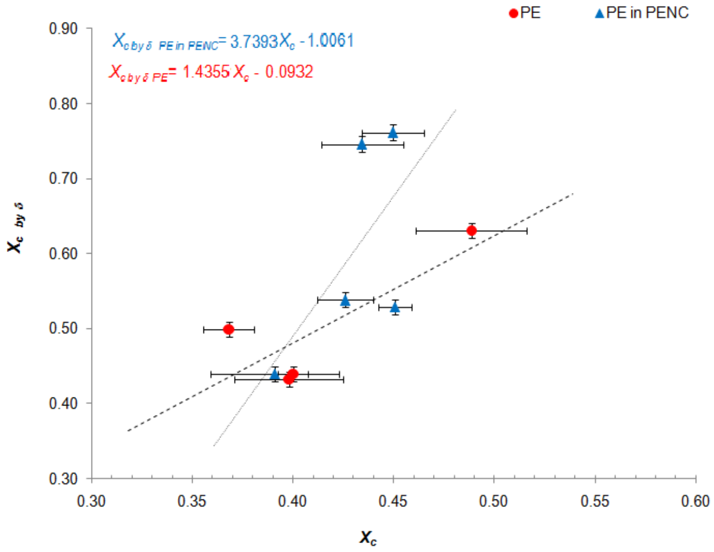

Figure 50 $X_{c\ by\ \delta}$ obtained by density measurements versus X_c measurements by *DSC* for the pure *PE* and *PE* in *PENC* at 100°C.

Relative high dispersion was observed for the crystalline fraction values obtained from *DSC* measurements compared to those obtained from density tests (apparent crystallinity). Since the correlation between the results obtained by these two different methods was not linear it was deduced that two different morphologic aspects were quantified.

Differences of crystalline content measured by two different techniques *DCS* and density in water reflected a more complex morphology than a simple diphasic material (amorphous and crystalline phases).

Figure 51 illustrates this situation by simultaneously presenting the variations with time of X_c and $X_{c\ by\ \delta}$ obtained by the different methods for a) the pure polyethylene and b) the nanocomposite *PENC*.

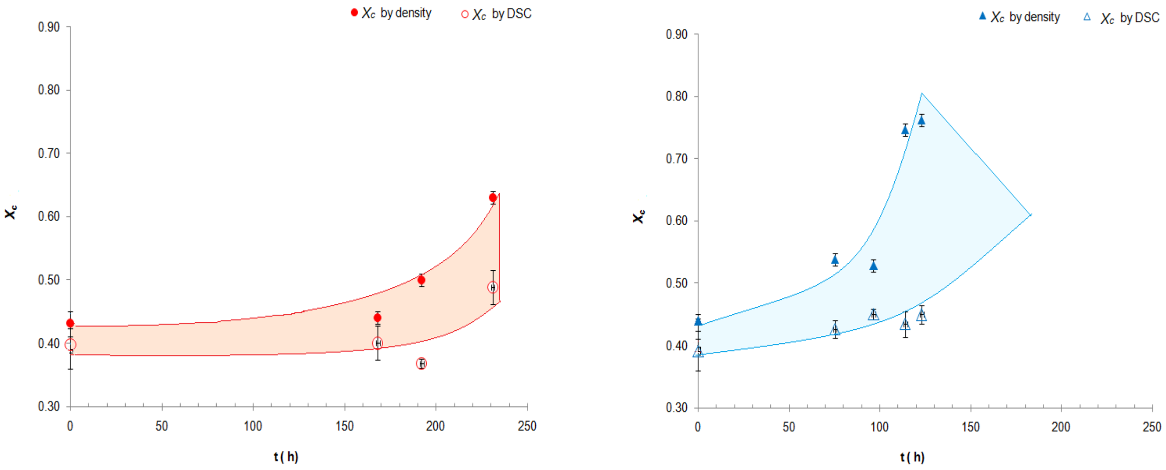

a)

b)

Figure 51 Interval X_c and $X_{c\ by\ \delta}$ variations with time for a) *PE* and b) *PENC* at 100°C.

The crystallinity ratios measured by *DSC* were consistent with the quantification of quasi-perfect crystals measured by *WAXS*. Raman spectroscopy allows determining the same crystallinity values detected by *DSC* and *WAXS*, but it must also permits to determine the interphase content [180] in *LDPE* or branched *PE* (it is not present in *HDPE*) [181,182]. This interphase is somehow supposed to be oriented and organized leads to a higher density than the amorphous phase. Finally, this interphase located between crystalline lamellae and amorphous phase could be considered as a mesophase responsible of β relaxation at about -30°C (Figure 52).

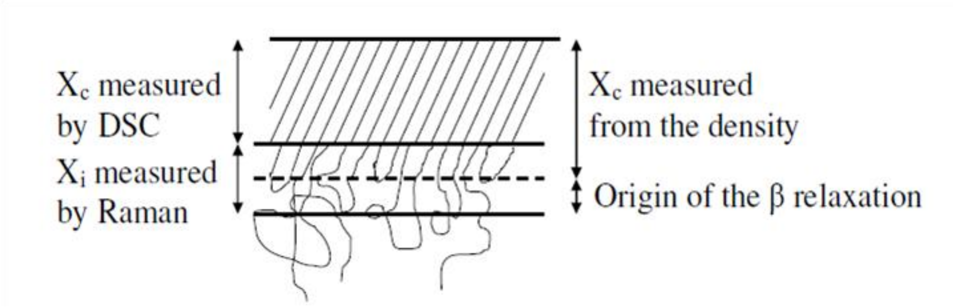

Figure 52. Sketch of a semicrystalline morphology including an interphase.

In branched *LDPE*, the amount of interphase could reach 15% in cases where the crystallinity ratios calculated based on densimetry measurements are significantly higher than the crystallinity ratios measured by *DSC*. Therefore, it seems that the chain scission process not only induces a chemicrystallization phenomenon (at low conversion degrees) but also increases the mesophase quantity for high conversion degrees (Figure 51).

Is this mesophase still an interphase? Is it present in the whole amorphous phase? Deeper studies should be done to precisely answer these questions. Experimental tools such as Raman spectroscopy and *SAXS* could provide valuable information about the mesophase nature especially knowing that at high conversion degrees, samples are highly brittle and techniques such as the Dynamic Mechanical Thermal Analysis *DMTA* cannot be used.

2.2.2.4. Chemicrystallization

It has been proposed that crystallinity ratio values can be linked to molar mass by defining a variable y related to the monomer units (or elementary chain segments) entering in the crystalline phase per scission event.

The instantaneous value y(t) of this yield is given by:

$$y(t) = \left(\frac{1}{M_m}\right)\left(\frac{dX_c}{dt}\Big/\frac{ds}{dt}\right) \tag{18}$$

where, M_m is the molar mass of the monomer unit (14 g mol^{-1} in the *PE* case), X_c is the crystallinity ratio and s is the number of chain scission event per mass unit.

According to Figure 53, the value of the yield can be assessed as 70. Quantitative data of chemicrystallization is relatively scarce in the literature: in the case of *PET* hydrolysis at 100°C, Ballara and Verdu [183] reported a value of 5-6 monomer units per scission. In the case of thermal *PE* thermal oxidation in the temperature range of 70°C to105°C, Viebke et al [166] found a value of 45 methylenes per scission. About the same value was found by Fayolle et al [165] for the *POM* thermal oxidation at 130°C.

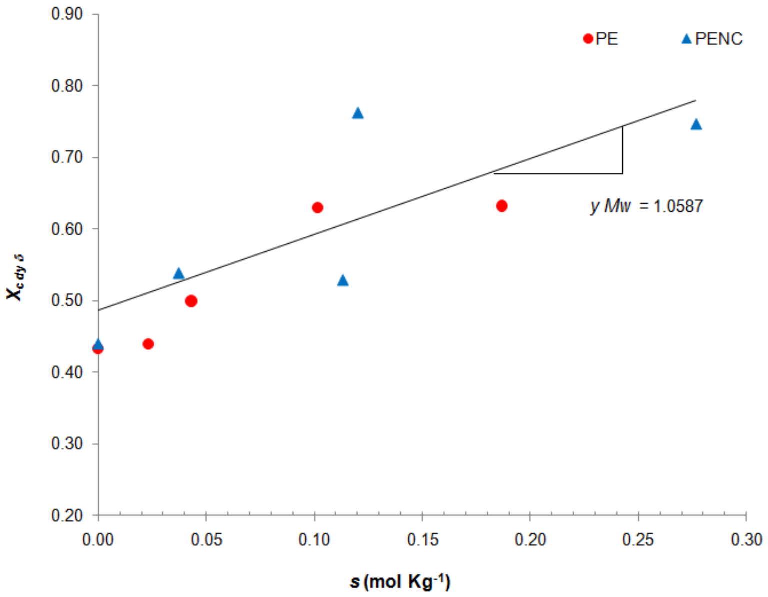

Figure 53 Experimental determination of ($yM_m = 1.0587$): graphics of $X_{c\ by\ \delta}$ against s for PE and $PENC$ exposed at 100°C.

From a theoretical analysis, Robelin-Souffaché and Rault [184] proposed:

$$x_c = 1 - \psi\left(\frac{1}{r_{WE}} - \frac{1}{r_W}\right) \tag{19}$$

where r_W and r_{WE} are the weight average gyration radio for the polymer under consideration and a polymer of which the molar mass is close to the entanglement threshold, respectively. ψ is a parameter depending on chemical structure and crystallization conditions.

Considering that, in a first approximation:

$$r_W \approx M_W^{1/2} \tag{20}$$

Equation 14 becomes:

$$X_c = \mathrm{a} + \mathrm{b}.M_W^{-1/2} \qquad (21)$$

where, a and b depend of the chemical structure and crystallization conditions.

Assuming that crystallinity is equal to the unity when molar mass is close to molar mass between entanglements, i.e. $X_c = 1$, when $M_W = M_{WE}$,

$$\mathrm{M}_{\mathrm{WE}} = \left(\frac{\mathrm{b}}{1-\mathrm{a}}\right)^2 \qquad (22)$$

By combining equations 21 and 22 the chemicrystallization model is the following [165,168,185]:

$$X_c = X_{c0} + \frac{1-X_{c0}}{\left[\left(\frac{M_{W0}}{M_{WE}}\right)^{1/2} - 1\right]} \cdot \left[\left(\frac{M_{W0}}{M_W}\right)^{1/2} - 1\right] \qquad (23)$$

where, X_{c0} and M_{w0} are the crystallinity fraction and the molar mass at time zero when sample has not been exposed and M_{WE} is the entanglement molar mass. According to literature, M_{WE} value is close to 2.95 kg mol^{-1} for polyoxymethylene *POM* [179,186], 3.5 kg mol^{-1} for polypropylene [187] and about 1.39 – 1.7 kg mol^{-1} for polyethylene [186,188].

Figure 54 compares the chemicrystallization curves to experimental values of X_c in function of the molar mass. The parameter values used in the chemicrystallization model are shown in Table 14.

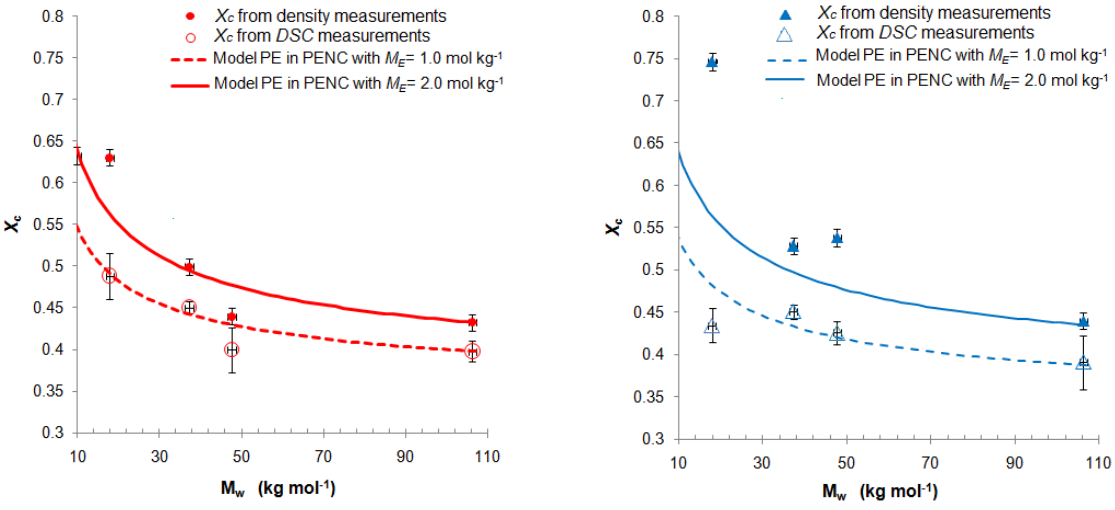

a) b)

Figure 54 Crystalline fraction obtained from density measurements versus molar mass for a) *PE* and b) *PE* in the composite.

$X_{c0\ PE}$	0.40	$M_{w0\ \mathrm{PE}}$ (kg mol^{-1})	106.3
$X_{c0\ PENC}$	0.39	$M_{w0\ \mathrm{PENC}}$ (kg mol^{-1})	96.5
$M_{wE\ \mathrm{minimum}}$		(kg mol^{-1})	1.0
$M_{wE\ \mathrm{maximum}}$		(kg mol^{-1})	2.0

Table 14. Parameter used in the chemicrystallization model.

The curves generated using the chemicrystallization model described well the general behavior of the variations of crystallinity extend in function of molar mass. By assigning different values to M_{WE} it was defined an interval where the vast majority of the experimental results were included. These values were obtained by the inverse method and fixed to 1.0 and 2.0 kg mol^{-1} for the low density polyethylene.

2.2.2.5. Prediction of the crystallinity changes with time

By using the Closed Loop Model (*CLM*) crystallinity fraction changes were simulated for *PE* and *PENC* at 100°C. For this purpose, the parameter of crystalline rate was included in the model (Equation 18). The origin of its changes was associated to the chemicrystallization process and the amorphous phase densification during aging.

$$\frac{dX_C}{dt} = yM_m\left(\frac{ds}{dt}\right) \tag{24}$$

with, yM_m assessed in Figure 53 (yM_m=1.058) and γ_s determined by inverse method ($\gamma s = 0.35$).

Including the full expression for $\frac{ds}{dt}$ (equation 15), $\frac{dX_C}{dt}$ was:

$$\frac{dX_C}{dt} = yM_m\begin{bmatrix}\gamma_s k_{1u}[POOH] + k_{1b}[POOH]^2 \\ +k_{1m}[POOH]^2 + k_{62}[POOP]_{cage}\end{bmatrix}\left[1 - MMT - X_c\right] \tag{25}$$

Experimental and simulation results of the simulated crystalline ratio (X_c) and the apparent crystalline ratio ($X_{c\text{ by }\delta}$) for the for the pure *PE* and the *PENC* were plotted on Figure 55.

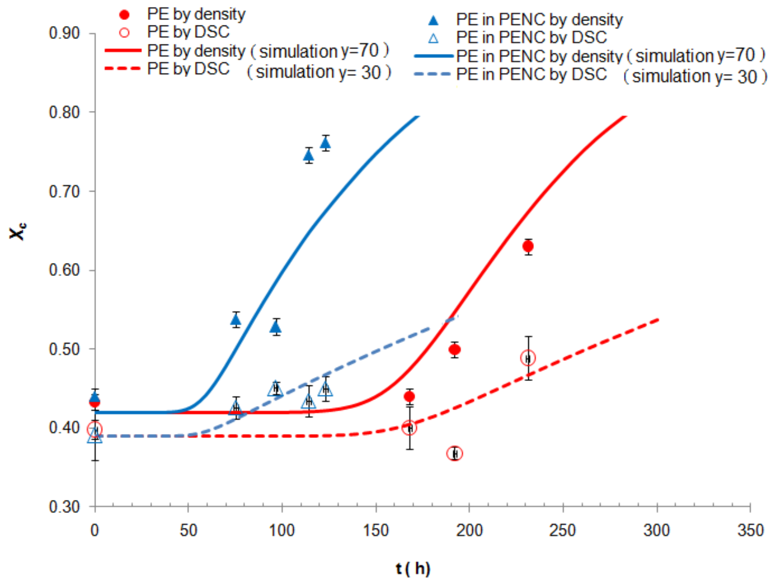

Figure 55 Predicted behavior for the crystalline ratio and for the apparent crystalline ratio for *PE* and *PENC* exposed at 100°C.

It was found a good agreement between apparent crystallinity ratios determined by densimetry and simulation results for both pure *PE* and nanocomposite *PENC* using a number of monomer units entering in the crystalline phase per scission event (y) equal to 70. A good agreement was found between crystallinity determined by *DSC* and simulation results of the crystallinity for y =30. The high values of crystallinity ratio calculated from density measurements suggest that chain scission process simultaneously induces lamella thickening and an increase of a mesophase content (less dense than the crystalline phase). Finally, based on the crystallinity ratio values predicted by the simulations, it can be supposed that the number of monomer units entering in the mesophase is higher than 70 for the *PE*.

2.2.3. Macroscopic Scale

2.2.3.1. Oxygen Permeability

The above mentioned morphological modifications should alter material macroscopic behavior even if those changes are associated to slight network damage. Oxygen permeability is a property that could be easily modified by small morphological variations such as the crystallinity ratio during the exposure time.

2.2.3.1.1. *Crystallinity Effect*

Since crystallinity phase can be considered as impermeable to oxygen flux, Compañ et al [189] proposed a model to calculate the diffusion coefficient (*D*) through the amorphous phase (D_{am}) in semicrystalline polymers in function of the crystallinity ratio (X_c) the temperature (*T*) and a constant *A* independent of the crystalline ratio and which has value of -1.75 when oxygen is the permeant fluid [189] (Equation 26):

$$D(X_c, T) = D_{am} \exp\left(-A(T)X_c\right) \qquad (26)$$

A homologous equation was used in the case of the permeability (*P*) including the parameter related to the amorphous phase permeability (P_{am}):

$$P(X_c, T) = P_{am} \exp\left(-A(T)X_c\right) \qquad (27)$$

Figure 56 presents experimental results obtained when testing pure *PE* and *PENC* at 23°C with different crystallinity ratios induced by an exposure at 100°C. Those results are compared to the oxygen permeability (P_{O2}) and oxygen diffusion coefficient (D_{O2}) simulated curves at 23°C.

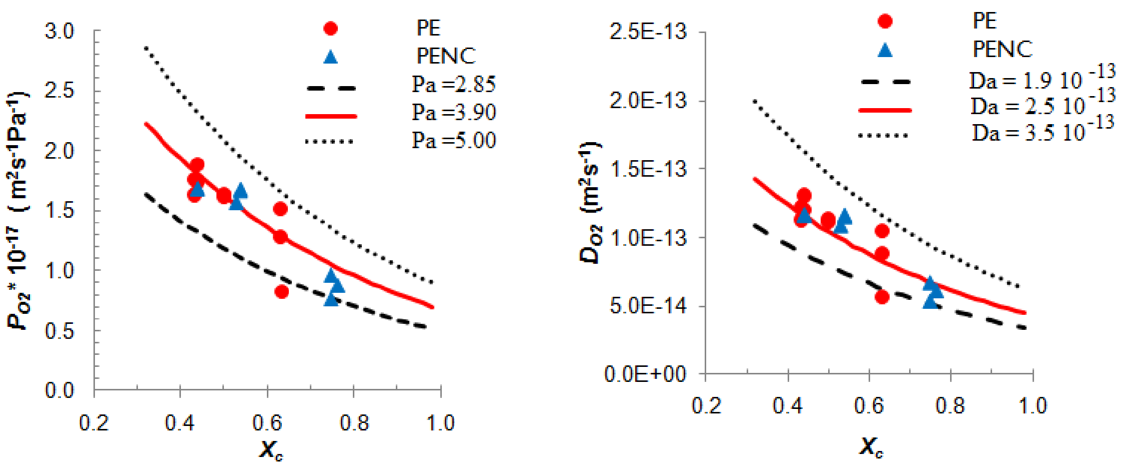

b) **b)**

Figure 56 Variation of permeability properties with the crystallinity content (X_c) at 23°C for *PE* and *PENC* samples exposed at 100°C. a) Oxygen permeability. b) Oxygen diffusion coefficient.

Firstly, there were not improvement effects induced by the nanoclay presence neither on the oxygen permeability (P_{O2}) nor on the polyethylene oxygen diffusion coefficient (D_{O2}). In other words, in this particular case (and with an intercalated morphology) the nanoclay did not affect the permeability properties of the pure polyethylene.

Secondly, it was put in evidence the effect of the crystallinity ratio on the oxygen permeability and on the oxygen diffusion coefficient: when the crystallinity ratio passes from 0.2 to 1, the oxygen permeability values decreased of 80%. The same analysis is valid for the oxygen diffusion coefficient: with a similar $\Delta X_c \approx 0.8$ D_{O2} varies from a value of about $2.0\ 10^{-13}\ m^2s^{-1}$ to $4.0\ 10^{-14}\ m^2s^{-1}$.

Based on these results and being examined the main oxidation effects manifested at molecular and morphologic scales, it is possible to predict the material permeability properties behavior during aging by including the oxygen diffusion term (Equation 28) in the *CLM*:

$$\frac{d[O_2]}{dt} = D_{O_2}\left(\frac{\partial^2[O_2]}{\partial^2 x^2}\right) - k_2[P^\bullet][O_2] + k_6[PO_2^\bullet]^2 \qquad (28)$$

The associated simulation conditions were: at any time, $[O_2]=[O_2]_s$ for $x=-\frac{L}{2}$ and $x=\frac{L}{2}$, the origin of depth coordinates was taken in the sample thickness middle.

Additionally to equation 28, it was necessary to use the expression related to the chain scission process calculated from molar mass measurements (section 2.2.1.1 and Figure 17), furthermore the changes of crystallinity ratio with exposure time (Figure 55) and the equations 26 and 27 were used to predict the values of P_{O2} and D_{O2} with time.

Figure 57 presents the experimental and simulated behavior of the oxygen permeability (P_{O2}) and the oxygen diffusion coefficient (D_{O2}) for an exposure at 100°C.

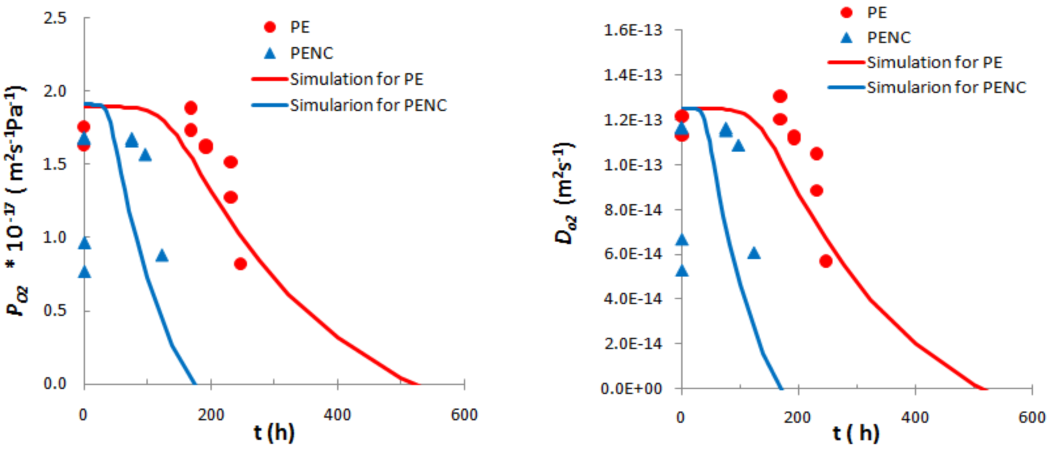

a) b)

Figure 57 Experimental and predicted behavior at 23°C for a) the oxygen permeability (P_{O2}) and b) the oxygen permeability coefficient (D_{O2}) with time at 23°C for pure *PE* and its clay nanocomposite *PENC.*

It was found a general good agreement between experimental and simulated behavior of the oxygen permeability and the oxygen diffusion coefficient. Based on molecular and morphological modifications it may be conceivable to define an oxygen permeability fail criterion to determine the endlife time of *PE* thin films.

3. Heterogeneous Oxidation – Thick Films

3.1. Oxidation Profiles

Oxidation profiles appeared within thick samples as a result of the oxidation controlled by an oxygen diffusion process. The distribution of degradation products along sample thickness result heterogeneous and an oxidation layer may be distinguished. Our goal was to validate the kinetic modeling by coupling the oxidation with the oxygen diffusion limitations. In order to put in evidence oxidation gradients, *FTIR* mapping and Micro Hardness Profiles tests were performed on thick samples (1400 µm). All experimental data was simulated by using our kinetic modeling including oxygen the diffusion process.

3.1.1. Experimental Results

The heterogeneous oxidation effects were measured by the techniques of *FTIR* in transmission mode (section 3.1.1.1) and *ATR/FTIR* (section 3.1.1.2) .for both PE and PENC 1400µm – thick films exposed at 100°C.

3.1.1.1. *FTIR* Mapping

Figure 58 corresponds to oxidation profiles of pure polyethylene for an uninterrupted exposition at 100°C during 0, 440, 459 and 697 hours. With time, carbonyl concentration on sample surface increased in a quasi uniform way along sample thickness including the center. A carbonyl slight profile started to appear after 440 hours of exposure. However, difference between carbonyl concentration values in the sample center and on the sample surface remained small. Finally, no oxidized layer could be clearly determined on these profiles.

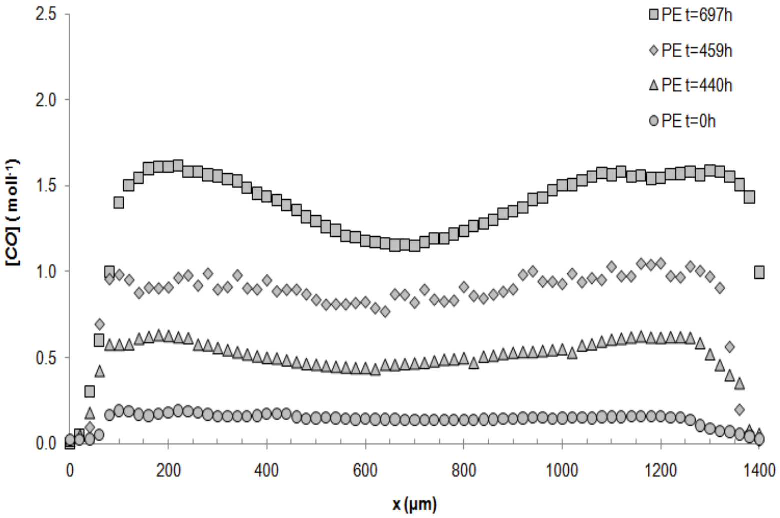

Figure 58 Oxidation profiles of the *PE* measured by *FTIR* mapping after different exposure times at 100°C.

Figure 59 presents oxidation profiles of the nanocomposite (*PENC*) measured after an uninterrupted exposition at 100°C during 0, 164, 179, 203, 214 and 221hours.

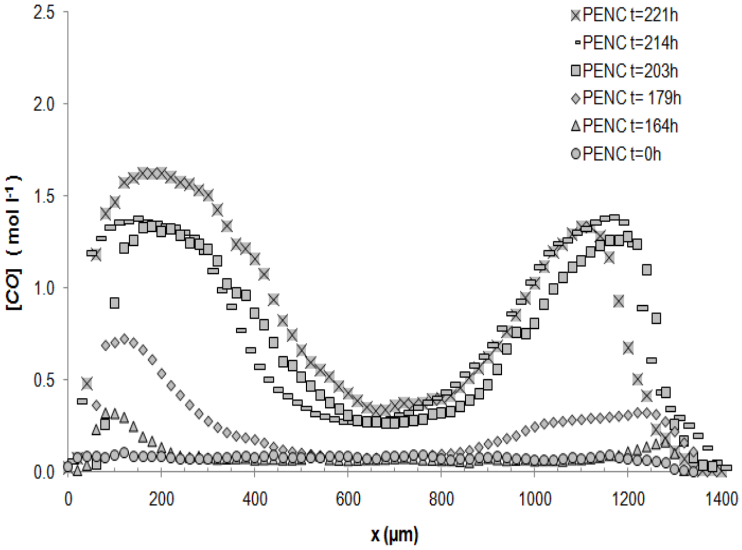

Figure 59 Oxidation profiles of the *PENC* measured by *FTIR* mapping after different exposure times at 100°C.

Two situations can be differentiated on the *PENC* oxidation profiles: the first case corresponds to low conversion degrees. Under this condition, carbonyl concentration on the surface increased with time, though a constant carbonyl concentration rests in the bulk. The latter may be generated when expending intramolecular oxygen during the degradation process. *PENC* profiles for 0, 164 and 179 hours of exposure belong to this category.

The second situation corresponds to high conversion degrees: a progressive oxidation of the sample surfaces and center can be seen since higher oxygen fluxes may pass toward the sample center. This diffusive phenomenon is faster compared to a relative slow degradation rate, which permits an additional oxygenation thus a higher degradation within the sample bulk. *PENC* curves for 203, 214 and 221 hours of exposure illustrate this category.

For both low and high conversion degrees, an oxidized layer thickness of 520µm was measured (on each *PENC* sample surface).

3.1.1.2. *ATR/FTIR* Imaging

Figure 60 a) and b) respectively present the carbonyl concentration profiles for pure *PE* after 0, 440, 459 and 697 hours and the composite *PENC* after 0, 164, 179, 203, 214 and 221hours of exposure. These profiles correspond to the first 400µm starting from the sample surface. The information provided by the *ATR/FTIR Imaging* for the *PE* and the *PENC* corroborated those obtained from *FTIR* measurements. A different situation was presented in Chapter III for the polypropylene system, where the *ATR/FTIR Imaging* was the chosen tool to detect thin oxidation layers about 15µm [164]. In the polypropylene case, such method permitted passing from a spatial resolution of 30µm (typical for *FTIR* measurements) to a higher resolution of 6µm needed to accurately study the *PE* and *PENC* oxidized layers.

Concerning *ATR/FTIR Imaging* results presented in Chapter IV, it was confirmed that for the *PE* no carbonyl profiles were formed before 697h (Figure 60 a). Finally, regarding the *PENC* profiles, for an interrupted exposure at 100°C the beginning of a transition from low to high conversion domain was found at 179h (Figure 60 b).

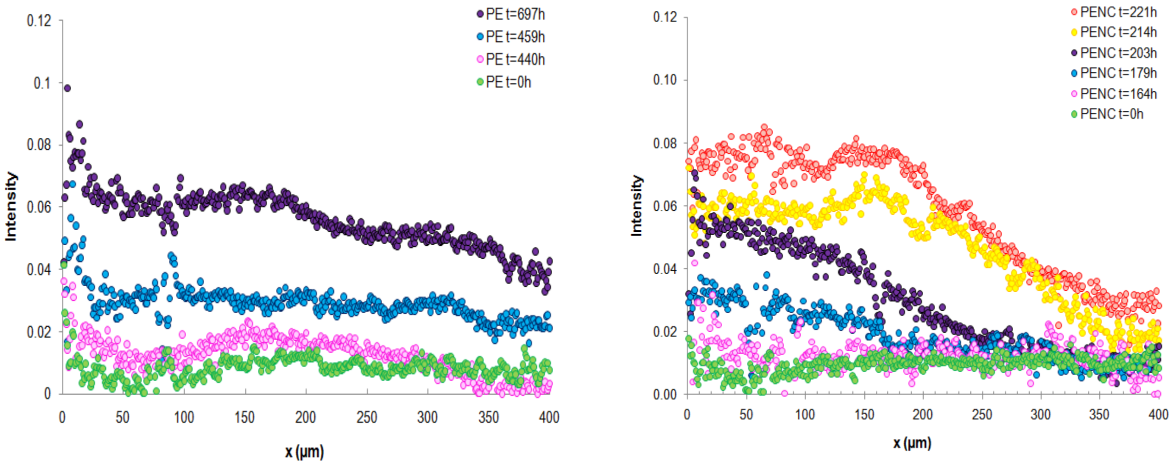

a) **b)**

Figure 60 Oxidation profiles measured by *ATR/FTIR imaging* after different exposure times at 100°C for 1400µm-thick films of a) *PE* and b) *PENC*.

3.1.2. Simulation of Oxidation Profiles

Among the variables used in the *CLM*, the oxygen permeability, the oxygen diffusion and the oxygen sorption coefficients are key parameters to successfully describe the oxidative behavior under heterogeneous conditions. For the sorption coefficient S_{O2} a common value of 1.8 10^{-8} mol $l^{-1}Pa^{-1}$ determined by inversed method was fixed for *PE* and *PENC*. This value was used to simulate the *PE* and *PENC* oxidation profiles. Concerning the D_{O2}, in chapter IV, section 1.4.2 it was set that clay presence do not change the *PE* permeability properties $D_{O2\,PE} = D_{O2PENC}$. Based on this result a unique common value of D_{O2} was chosen to simulate PE and PENC oxidation profiles. Extrapolating the literature date for D_{O2} at 100°C a value of 1.10 10^{-9} m^2s^{-1} was obtained [46,190,191,192]. Such value has the same order of magnitude that D_{O2} value determined by inversed method (D_{O2} = 19 10 10^{-9} m^2s^{-1}). These values were in good agreement but they differ from extrapolations at 100°C based on experimental values determined at 7°C, 23°C and 50°C. Even if there was this discrepancy due to experimental incertitude associated to the test, literature and inverse method calculated values are consistent, and this fact confirms the assumption made about S_{O2} that permitted to obtain realistic values of D_{O2}. Table 15 summarizes literature, experimental and inverse method determined values of D_{O2} and S_{O2} for polyethylene.

	T (°C)	**S_{O2} (mol l^{-1} Pa^{-1})**	**$D_{O2\,PP}$ (m^2s^{-1})**
Literature Ea ($kJmol^{-1}$)		8.2 10^{-1}	3.7 10^{1}
Extrapolation	100	1.9 10^{-8}	1.1 10^{-9}
Experimental	7	8.1 10^{-7}	5.9 10^{-14}
	23	6.7$10^{-7}$	1.2 10^{-13}
	50	3.4 10^{-6}	5.6 10^{-13}
Arrhenium Ea ($kJmol^{-1}$)	100	2.7 10^{1}	3.9 10^{1}
Extrapolation		8.7 10^{-6}	2.8 10^{-12}
Inverse method	100	1.8 10^{-8}	19 10^{-9}

Table 15 Oxygen diffusion and oxygen solubility values for PE .

Using the parameters determined by inverse method shown in Table 15 it was possible to describe all the carbonyl profiles for the *PE* (Figure 61) and low conversion degree profiles of the *PENC* (0h, 164h and 179h) (Figure 62).

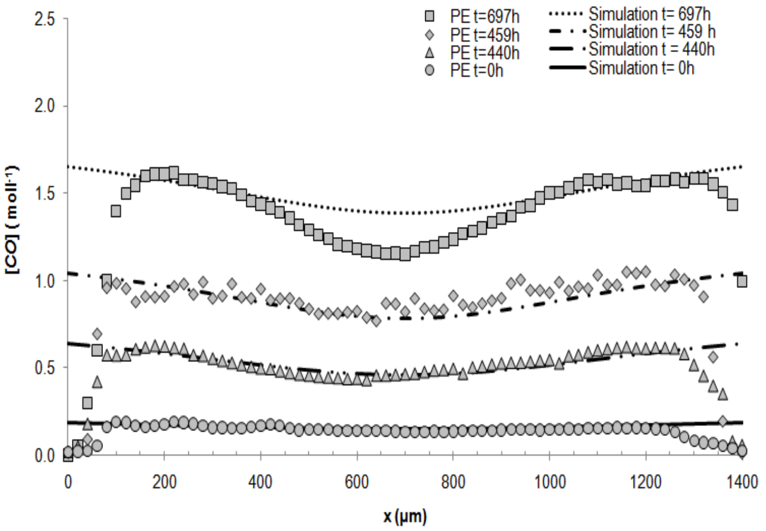

Figure 61 Simulation and experimental profiles of *PE*.

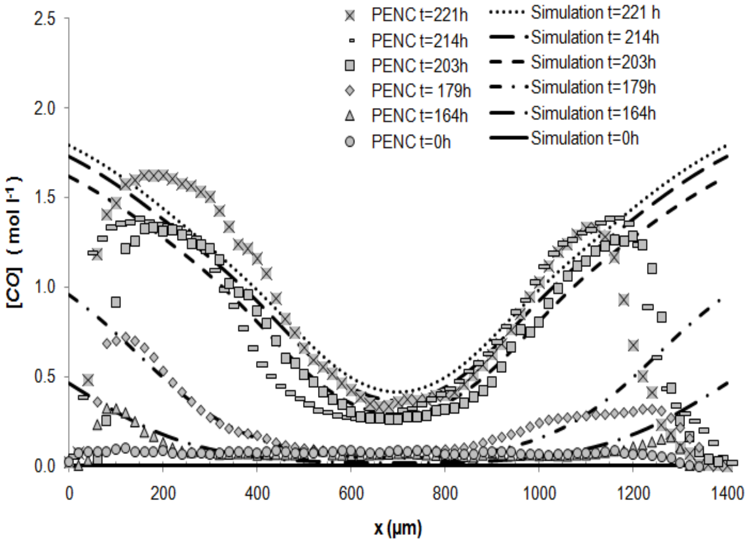

Figure 62 Simulation and experimental profiles of *PENC*

It was not possible simulate high conversion degrees (profiles present only in the *PENC* at t= 203h, 214h and 221h) using the same oxygen coefficient value. To describe those profiles it was need a D_{O2} of 3.95 10^{-9} m^2s^{-1}. It means that when a sample gets to a high oxidation degree its permeability properties change.

Experimental profiles for both *PE* and *PENC* are flattered near to their sample surfaces. Considering oxidation mechanism in semicrystalline polymers with a prior oxidation of the amorphous phase, the mesophase - in the image of crystal - should be less sensitive to oxidation than the amorphous phase. If the existence of a high content of mesophase at the surface is considered, it can imagine that the oxidation is slowed and nearly stopped. This hypothesis seems realistic and could explain the carbonyl content evolution at high conversion degree.

The especial characteristics of oxidation profiles resulting from the mesophase presence could not be simulated because this factor was not included when modeling our system. To integrate these morphological characteristics into the kinetic model, additional information regarding the physical nature and the oxidation behavior of the interphase is need it.

3.2. Pseudo – elastic Modulus

3.2.1. Micro Hardness Profiles tests

Micro hardness profiles measured for a *PENC* unaged sample and a *PENC* sample exposed 214h at 100°C are showed in Figure 63. In the unaged *PENC* sample no oxidation profile was detected. On the contrary, when sample reached a high degree of conversion an elastic modulus profile appeared. The oxidized layer thickness measured on such profile was 520 µm which corresponded to the same thickness measured on the *PENC* carbonyl profiles.

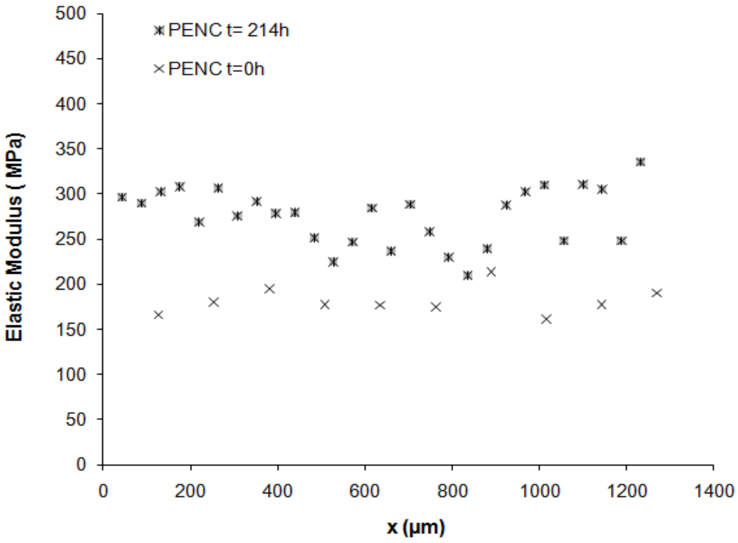

Figure 63 Micro hardness profiles for *PENC* at t=0 h and after t=214 h of exposure at 100°C.

3.2.2. Elastic Modulus Profiles – Modeling

Simulation of elastic modulus variations along the sample thickness was performed in two steps. During the first stage crystallinity ratio variations with time along sample thickness were calculated including an expression for the crystallization rate $\frac{dX_c}{dt}$ (Equations 15 and 25) in the *CLM*. Figure 64 presents the crystallinity ratio variation across *PENC* sample thickness for initial crystalline ratio (X_{c0}) on the surface equal to 0.39 (measured by *DSC* for unaged *PENC* samples) and $X_{c\,0}$ = 0.45 measured by *DSC* in a *PENC* sample after 123h of exposure.

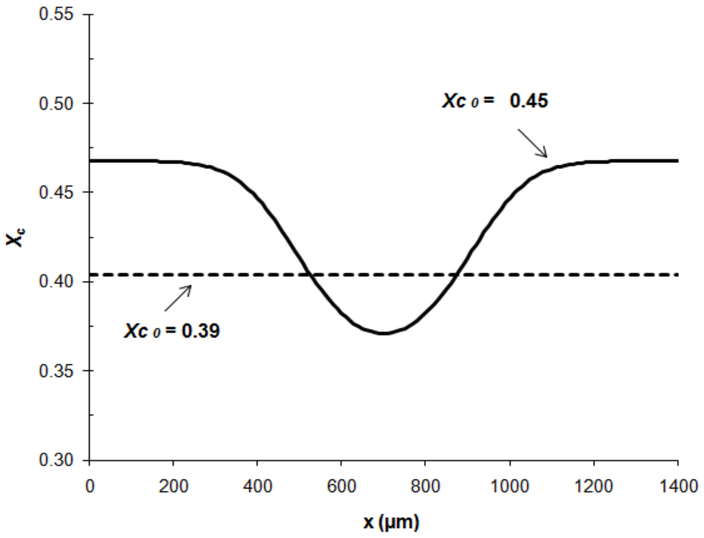

Figure 64 Simulated crystalline ratio profiles across the *PENC* thickness for X_{c0}= 0.39 and X_{c0} =0.46.

Using simulated crystalline ratio profiles for both unaged and aged *PENC* samples a mathematical function derived from a micromechanical model of the elastic properties of *PP* and *PE* was used in order to obtain values of elastic modulus in function of crystalline ratio variations (Figure 65) [193].

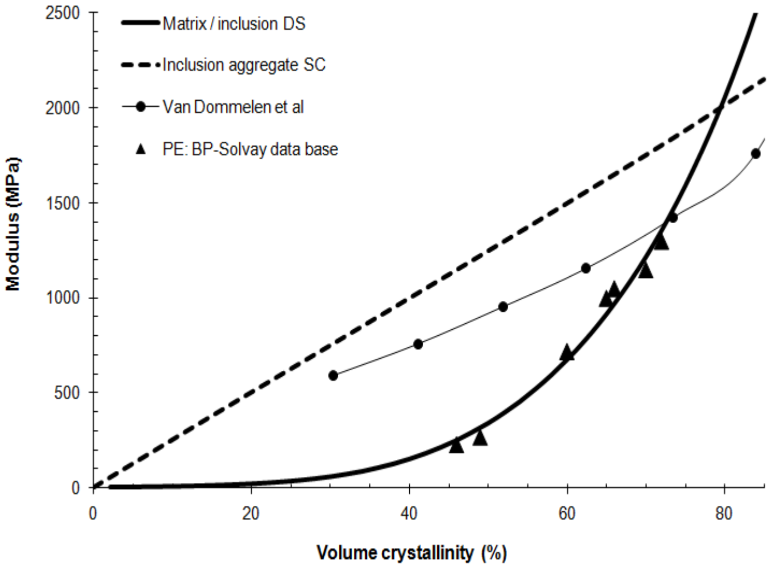

Figure 65 Micromechanical model of the changes of elastic modulus in function of crystalline fraction [193].

According to Figure 65, it is evident that the variations of modulus determined from microhardness measurements (150 to 300 MPa after 214h for *PENC*) can be explained only by a low variation of crystallinity – crystalline ratio measured by *DSC*- . Then the mesophase would have a low modulus, similar to those of the amorphous phase. This hypothesis is consistent if it is considered that the mesophase is like an interphase in *PE* and has its relaxation (β relaxation in *PE*) at -30°C. Microhardness tests at -50°C for example should provide experimental proofs to accept this hypothesis.

Figure 66 compares experimental results obtained from the micro hardness tests against simulation results for the *PENC* when using the minimal and the maximal crystallinity measured by *DSC* for the *PENC* at time zero (0.36 $<X_{c\ 0}<$0.42) and 0.434 $< X_{c0} <$ 0.465 measured for *PENC* at $[CO]_{av}$ = 0.4 mol l^{-1}(section 2.2.2.1).

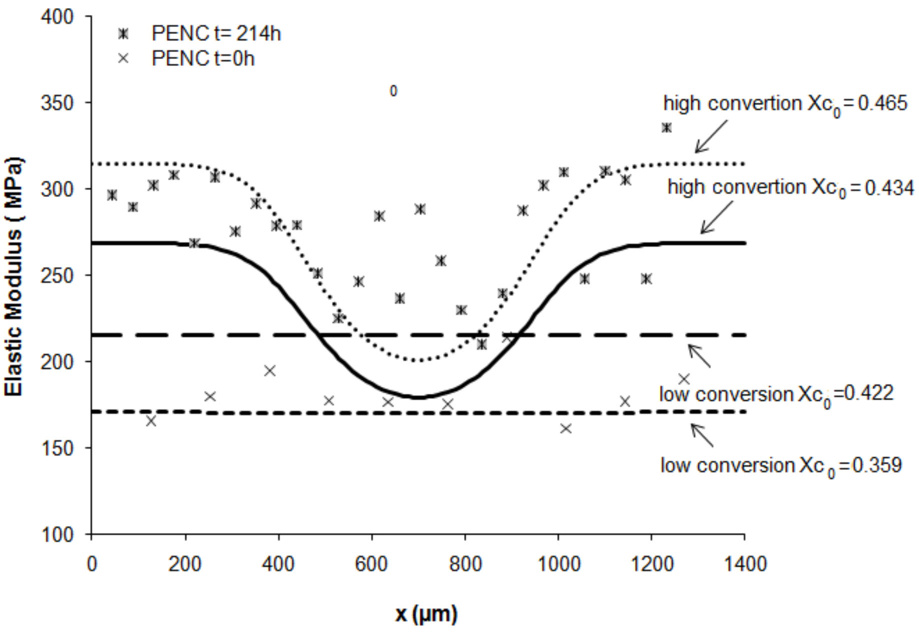

Figure 66 Experimental and simulation profiles of elastic modulus along *PENC* sample thickness after an exposure at 100°C for t= 0 and t = 214h.

It was possible to describe the general shape of the elastic modulus profile within the sample thickness for both exposure times. Also, measured thickness of the oxidation layer of about 520 µm was consistent to those measured on the carbonyl profiles (Figure 61).

3.3. Discussion of the Heterogeneous Behavior

Two differences between oxidation profiles of *PE* and *PENC* were found. Firstly, the oxidized layer thickness could not be determined for the *PE*, meanwhile for the *PENC* an oxidized layer of about 1040µm (twice 520µm) was measured. Secondly, for the pure polyethylene carbonyl profiles (Figure 58), a direct transition from non oxidized state (without profile) to a high conversion regime was observed. For *PE*, the first signs of a profile started to be noticed after 440 hours of exposure, contrary to the *PENC* case where the change of regimen rapidly took place.

On the other hand, from oxygen diffusion properties results (section 2.2.3.1) it was concluded that the clay presence in the *PENC* did not create an effective oxygen barrier to the oxygen flux through the sample.

By assembling these two aspects, it was deduced that differences between oxidized behavior of thick films of *PE* and *PENC* do not result from a tortuous path provided by the montmorillonite, but from the clay chemical action manifested as an increase of the oxidation rate. Such catalytic effect changes the physics of the oxidation process when it is controlled by oxygen diffusion. In other words, the difference between *PE* and *PENC* is due to a dominating degradation rate of *PENC*: the rapid formation of the *PENC* oxidized layer on the sample surface serves as a physical barrier which prevents oxygen flux toward sample bulk due to their higher crystallinity.

Regarding micro hardness profiles, it was possibly to predict the shape of elastic modulus profiles for a thick *PENC* sample using the simulated crystallinity profiles. Furthermore, effects of the crystalline - amorphous interphase were identified not only on the oxidation profiles by flattening them near to the sample surface but also on the elastic modulus profiles inducing similar effects. This latter result put in evidence the mechanical inactivity of the mesophase since the crystallinity profiles used to simulate the elastic ones were calculated using the *Xc* measured by *DSC* (Figure 67).

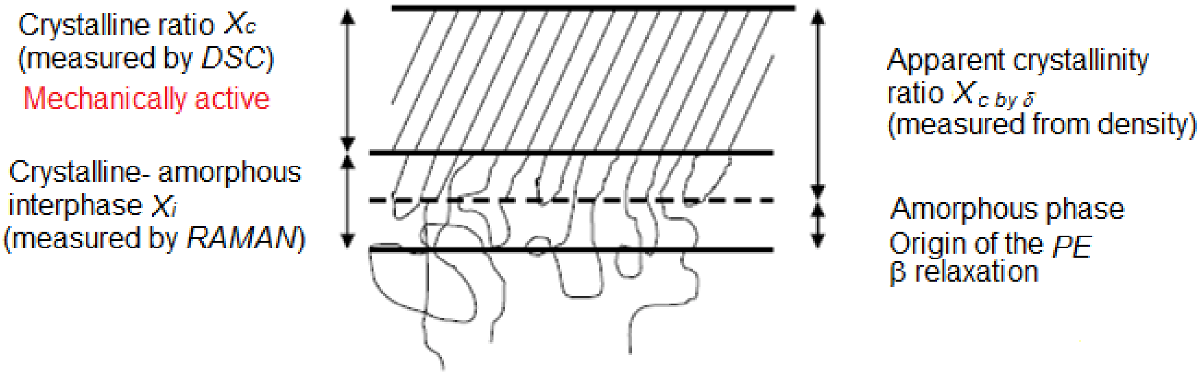

Figure 67 Schema of the morphologic configuration, methods of detection and mechanical function of each phase for the *PE* and *PENC*.

Finally, the thickness of the *PENC* oxidized layer measured in the elastic modulus profiles was accurately predicted in comparison to those obtained from *FTIR* measurements. These lasts results confirmed the possibility of predicting of material macroscopic behavior using the Closed Loop Model.

Conclusions

This chapter dealt with the thermal degradation of the unstabilized clay nanoreinforced polyethylene under low and moderated temperatures. The first part was dedicated to the homogeneous degradation of the above mentioned system, when not oxygen diffusion limitations were present. The second part studied corresponded to the heterogeneous degradation when oxidation is coupled to oxygen diffusion process.

A general strategy was applied to deal with the mentioned aspects using two complementary approaches: experimental testing at different material scales (molecular, morphologic and macroscopic) permitting to detect progressive but discrete changes induced by the chemical aging. As a complemented, a non empiric approach based on computational simulations using a radically kinetic model was applied.

From the homogeneous degradation study several conclusions were obtained: an important catalytic effect induced by the iron particles contained in the organically modified montmorillonite was found during the polyethylene homogeneous thermooxidation. Such effect was characterized and quantified using a rate constant k_{1m} having a pre-exponential factor of 1.5 10^{14} l $mol^{-1}s^{-1}$ and an activation energy $E_a\ k_{1m}$ equal to 130 kJ mol^{-1}.

Furthermore, the results compilation of different aspects studied under homogeneous degradation conditions was a confirmation of the cause – effect chain of the material property loss: chain scissions lead to morphological changes resulting on progressive decrease of molar mass with time. As a result, the inclusions of oxygen atoms within the amorphous phase coexist with the chemicrystallization phenomena. This association not only increases crystalline ratio, but also an interphase or mesophase content (growing with time) entailing to detectable property losses at macroscopic scale.

From the heterogeneous study, a good description of the carbonyl concentration profiles for *PE* and *PENC* across sample thickness was obtained. At high conversion degrees, the carbonyl concentration prediction is higher that experimentally measured, but it could be explained by the presence of a mesophase which would slow down the oxidation process. Also, it was possible to measure an oxidized layer thickness of 520 µm for the *PENC* samples exposed at 100°C.

As a general conclusion from the heterogeneous degradation study of *PE* and *PENC* it could be said that the first steps to coupling chemical aging to a macroscopic embrittlement process permitted to describe the long term mechanical behavior of the material. Nonetheless, it is necessary to push the inclusion of the high conversion degree conditions as additional factors to the low conversion degree description when simulating the degradation process. It is by combining this dual behavior that the aging process of thick and complex pieces could be globally tackled. Only under this condition it will be possible to provide a macroscopic realistic prediction of the long term behavior of thick pieces superficial layers that usually are the main responsible of piece fracture.

References

150 Hummel Dieter. Atlas of polymer and Plastics Analysis. Polymers: Structure and Spectra. Vol 1. 2 ed. 1978. Cologne.

151 Picard E, Vermogen A, Gerard J-F, Espuche E. Influence of the Compatibilizer Polarity and Molar Mass on the Morphology and the Gas Barrier Properties of Polyethylene/Clay Nanocomposites. Journal of Polymer Science: Part B: Polymer Physics. 2008; 46: 2593-2604.

.

152 Villanueva MP, Cebedo L, Lagaron JM, Gimenez E. Comparative Study of Nanocomposites of Polyolefin Compatibilizers Containing Kaolinite and Montmorillonite Organoclays. Journal of Polymer Applied Science. 2010; 115: 1325-1335.

153 Emanuel MN. Thermo-oxidative ageing of polymers. Polym. Sci. USSR. 1985; 27:1505-1526.

154 Allen NS, Katami H. Influence of titanium dioxide pigments on thermal and photochemical oxidation and stabilization of polyolefin films. Advances in Chemistry Series. 1996; 249: 532-535.

155 Hawkins WL, Matreyek W, Winslow F. H. The morphology of semicrystalline polymers. Part I. The effect of temperature on the oxidation of polyolefins. Journal of Polymer Scince. 1959; 41: 1-10.

156 Baum B. The mechanism of polyethylene oxidation. J. Appl. Polym. Sci. 1959; 2: 281-288

157 Gugumus F. Re-examination of the role of hydroperoxides in polyethylene and polypropylene: chemical and physical aspects of hydroperoxides in polyethylene. Polym. Deg. & Stab.1995; 49 :29-50.

158 Lacoste J, CarlssonDJ. Gamma-, photo-, and thermally-initiated oxidation of linear low density polyethylene: A quantitative comparison of oxidation products. Journal of Polymer Science Part A: Polymer Chemistry.1992; 30: 493-500.

159 Chirinos-Padrón, A.J. , Hernández, P.H. , Allen, N.S. , Vasilion, C. , Marshall, G.P. , de Poortere, M. Synergism of antioxidants in high density polyethylene. Polym. Deg. & Stab. 1987; 177-189.

160 Rudin A, Schreiber HP, Waldman MH. Measurement of Polyethylene Oxidation by Differential Thermal Analysis. *Ind. Eng. Chem.*1961;53: 137-140.

161 Phease T. L S. W, Billingham N. C, Bigger .The effect of carbon black on the oxidative induction time of medium-density polyethylene. Polymer.2000; 15: 9123-9130.

162 Colin J, Monchy-Leroy C, Audouin L, Verdu J. Lifetime prediction of polyethylene in nuclear plants. Nuclear INSTRUMENTS AND Methods in Physics Research B. 2007; 265: 251-255.

---

163 Khelidj N, Colin X, Audouin L, Verdu J, Monchy-Leroy C, Prunier V. Oxidation for polyethylene under irradiation at low temperature and low dose rate. Part II: Low temperature thermal oxidation. Polymer Degradation and Stability. 2006; 91: 1598- 1605.

164 Gutiérrez G, Fayolle B, Régnier G, Medina J. Thermal oxidation of clay-nanoreinforced polypropylene. Polymer Degradation and Stability. 2010; 95 (9): 1708- 1715. 2010.

165 Fayolle B, Richaud E, Colin W, Verdu J. Review: degradation-induced embrittlement in semi-crystalline polymers having their amorphous phase in rubbery state. J. Matter Sci. 2008; 43: 6999-7012.

166 Viekbe J, Elble E, Ifwarson M, Gedde UW. Degradation of unstabilized Medium-Density Polyethylene Pipes in Hot-Water Applications. Polymer Engineering and Science. 1994. 34: 1354 – 1361.

167 Suarez JCM, Biasotto E. Characterization of degradation gamma-irradiated recycled polyethylene blends by scanning electron microscopy. Polymer Degradation and Stability. 2001; 72: 217-221.

168 Fayolle B, Audouin L, Verdu J. A critical molar mass separating the ductile and brittle regimes as revealed by thermal oxidation in polypropylene. Polymer.2004; 45: 4323-4330.

169 Girois S, Audouin L, Verdu J, Delprat P, Marot G. Molecular weight changes during the photooxidation of isotactic polypropylene. Polymer Degradation and Stability. 1996. 51; 125-132.

170 Colin X, Verdu J. Polymer degradation during processing. C.R Chimie. 2006; (9): 1380-1395.

171 Fouad H . Effect of Long-Term Natural Aging on the Thermal, Mechanical, and Viscoelastic Behavior of Biomedical Grade of Ultra High Molecular Weight Polyethylene. Journal of Applied Polymer Science. 2010. 118 ; 17 – 24.

172 Watanabe S, Sano N, Noda I, Ozaki Y. Surface melting and lamella rearrangement process in linear low density poliethylene. J. Phys Chem B. 2009 ; 19 : 3385- 3394.

173 Grecco A, Maffezzoli A. Correction of melting peaks of different PE grades accounting for heat transfer in DSC samples. Polymer Testing . 2008; 27: 61- 74.

174 Kennedy MA, Peacock AJ, Mandelkern L. Tensile Properties of Crystalline Polymers: Linear Polyethylne. Macromolecules. 1994; 27: 5297 – 5310.

175 Kitta KH, Tanaka A. Dynamic mechanical properties of metallocene catalyzed linear polyethylenes. Polymer. 2001; 42: 1219- 1226.

176 Munaro M, Akcelrud L. Correlations between composition and crystallinity of LDPE/ HDPE blends. J Polym. Res. 2008; 15: 83-88.

177 Hari J, Dominkovics Z, Fekete E, Pukanszky. Kinetics of structure formation in PP/layered silicate nanocomposites. Express Polymer Letters. 2009; 3 (11): 692-702.

---

178 Langlois Valérie. Vieillissement Thermique du Polyethylene Reticulé. PhD Thesis, Ecole Nationale Supérieure d’Arts et Métiers - Centre de Paris, 1992.

179 Van Krevelen DW.1990. Properties of polymer. 3rd edition. Elsevier, Amsterdam.

[180] Rull F, Prieto AC, Casado JM, Sobron F, Edwards HGM· Estimation of crystallinity in polyethylene by Raman spectroscopy. Journal of Raman Spectroscopy.1993; 24: 545 – 550.

181 Humbert Séverine. Influence de la topologie moléculaire et de la microstructure sur les propriétés mécaniques des Polyéthylènes, PhD Thesis. INSA Lyon, 2009.

182 Humbert S, Lame O, Vigier G. Polyethylene yielding behaviour: What is behind the correlation between yield stress and crystallinity? Polymer. 2009; 50: 3755-3761.

183 Ballara A, verdu J. Physical aspects of the hydrolysis of polyethylene terephthalate. Polymer Degradation and Stability.1989 ; 26 : 361 – 364.

184 Robelin-Souffache E, Rault J. Origin of the long period and crystallinity in quenched semicrystalline polymers.Macfomolecules . 1989 ; 22 : 3581- 3594.

185 Fayolle B, Audouin L, Verdu J. Radiation induced embrittlement of PTFE. Polymer. 2003; 44: 2773-2780.

186 Wu Souheng. Chain Structure and entanglement. Journal of Polymer Science.1989; 27 (4): 723- 741

187 Greco R et al, 1987 Greco R, Ragosta G. Plastics Rubber Process Appl. 1897; 7: 163.

188 Fayolle B, Audouin L, Verdu J. Mechanism of degradation induced embrittlement in polyethylene. Polymer Degradation and Stability. 2007: 92: 231-238

189 Compañ V, Del Castillo LF, Lopez-Gonzales M.M, Riande E. Crystallinity Effect on the Gas Transport in Semicrystalline Coextruded Films Based on Linear Low Density Polyethylene. 2010. Journal of Polymer Science: Part: B: Polymer Physics; 48: 634-642.

190 Hedenqvist M, Angelstok A, Edsberg A, Larsson PT, Gedde UW. Diffusion of small-molecule penetrants in polyethylene: free volume and morphology. Polymer. 1996; 37: 2887-2902.

191 Scott G. Atmospheric oxidation and antioxidants. vol. 2, Elsevier Science Publishers, Amsterdam, 1993.

192 Premnath V, Harris VH, Jasty M, Merrill EW. Gamma sterilization of UHMWPE articular implants: an analysis of the oxidation problem. Biomaterials 1996; 17: 1741 – 1753.

193 Bédoui F, Diani J, Régnier G. Micromechanical modeling of elastic properties in polyolefins. Polymer. 2004; 45: 2433 – 2442.

GENERAL CONCLUSIONS AND PERSPECTIVES

Nowadays, clay nanoreinforced nanocomposites are used in several applications, packaging being particularly preferred due to an important increase of material barrier properties. Montmorillonite is one of the most commonly used bentonite clays in the production of polyolefinic clay nanocomposites.

If new clay nanoreinforced materials are potentially highly performing, the inconvenient arises when a prediction of their long term behavior is required. The ways in which clay presence affects material and their consequences on nanomaterial durability belonged to a rarely explored subject despite the boom of publications dealing with polyolefinic clay nanocomposites.

Our goal was to examin clay polyolefin nanocomposites in order to get a better comprehension of the effects induced by the presence of nanoclay on the thermooxidation process of polyolefins under low to moderated temperatures (60°C to 100°C). For this purpose, two systems were studied:

- Unstabilized polypropylene / coupling agent based on a polypropylene matrix/ organically modified montmorillonite (*MMT-O*).
- Unstabilized low density polyethylene / coupling agent based on a *LDPE* matrix/ organically modified montmorillonite (*MMT-O*).

Regarding the *PP*/coupling agent/ *MMT-O* system, the main properties of a polyolefinic nanocomposite were put into evidence:

- ✓ Nanocomposite oxygen permeability presented a decrease of 45% when clay was present in the intercalated / exfoliated system.
- ✓ A catalytic effect was detected speeding up the degradation rate. This effect was associated to metallic traces initially present in the *MMT-O*.

Additionally, an oxidation kinetic behavior modeling for the *PP*/coupling agent/ *MMT-O* was successfully performed for degradation process with and without oxygen diffusion control.

Concerning the second system (*LDPE*/coupling agent/ *MMT-O*), several aspects were put into evidence in our work:

- ✓ Little or no influence of the clay on the *LDPE* permeability properties was detected. A possible explanation to this fact is that *PENC* presented low dispersion of clay sheets at nanometric scale resulting in an intercalated morphology, less developed than the fully exfoliated and the intercalated / exfoliated morphologies.

- ✓ During homogeneous oxidation process (not controlled by the oxygen diffusion) a catalytic effect was detected and quantified as an initiation agent that induces a reaction for the hydroperoxyde decomposition.

- ✓ In addition, based on the behavior of the crystalline fraction during aging (measured by *DSC* and densimetry) it was observed that the chain scission process generates high conversion degrees that contribute to the creation of an important quantity of interphase or mesophase. This phase has an intermediary density compared to the amorphous and the crystalline phases.

Moreover, a homogeneous degradation process was successfully modeled not only to simulate the system chemical behavior, but also to prede changes induced by the oxidation process on the oxygen permeability properties at macroscopic scale. The adopted strategy permitted studying of the phenomena taking place at morphologic scale (such as chemicrystallization) allowing to link the molecular scale to the macroscopic world. In other words, this multi scaled approach can simulate all the modifications induced by oxidation using perfectly defined parameters.

In reference to the heterogeneous process when oxygen diffusion limitation governs degradation process, several aspects were highlighted:

- ✓ For thick samples exposed at 100°C, no oxidation profiles for the pure polyethylene were found, contrary to the clay nanoreinforced polyethylene where an approximately 520µm-thick oxidation layer was easily identified on both sample surfaces for the high conversion degree. This effect resulted of the clay catalytic effect on the degradation rate of the nanocomposite: a faster degradation rate induces a quick formation of an oxidized layer (highly crystallized) which does not permit oxygen to pass through towards sample bulk. The oxygen diffusion coefficient rests unaffected by the presence of clay and does not affect oxidation profiles.

Complementary to carbonyl profiles, clay nanocomposite oxidized profiles were also found when measuring modulus, thus confirming the degradation heterogeneity along sample thickness as well as the magnitude of the oxidized layers.

- ✓ Profiles across the sample thickness were successfully simulated by coupling degradation with oxygen diffusion. For the low conversion, simulations of carbonyl profiles were performed. Additionally, by using crystallinity changes detected by *DSC* and structure–property relations found in literature it was possible to simulate the modulus profiles. These results corresponded to a first simulation approach for predicting long term behavior in the case of oxidative aging of thick samples. For the high conversion degree (near to the surface of thick samples), predictions of carbonyl concentration are higher than its measured results. The reason of this behavior could be related to the role played by an interphase less sensitive to oxidation than the amorphous phase. The effect of such mesophase on the elastic properties seems moderated but logic if it is assumed (like certain research groups do) that it has a relaxation about -30°C. This temperature corresponds to the β relaxation of the *PE*.

To conclude, we wanted to list some features related to the thermal degradation of clay polyolefins nanocomposites we conceive as perspectives of this study:

- From an experimental point of view, investigation of clay polyolefinic systems having several exfoliation levels represents a first aspect to be explored. The effects of the clay spatial distribution on the endlife prediction are factors that until now were not taken into account when no empirical approaches were used.

- Additionally, knowing that the catalytic character of the clay is dominated by diverse facts such as the organic modification process, it could be interesting to carry out studies using clays presenting different kind of organic modification in order to compare the clay catalytic power during the composite degradation process.

- Since the present work deals with unstabilized clay / polyolefin systems, the next logical step is to study their degradation process using stabilizing systems. Interactions between stabilizers and clay and their impact on the nanocomposite lifetime are essential aspects to take into account when predicting stabilized nanomaterials endlife.

- Finally, it seems necessary to perform a detailed research of degradation process for the high conversion degrees. It should include a complete characterization of the mesophase and its functions. From an experimental point of view it could be performed by using raman spectroscopy, *SAXS* and nano indentation at different temperatures.

CONCLUSIONS GENERALES ET PERSPECTIVES

Les nanocomposites à base d’argile interviennent de nos jours dans de nombreuses applications, comme l’emballage qui demande l’emploi de matériaux présentant de bonnes propriétés barrières. La montmorillonite est l’une des argiles les plus utilisées dans l’obtention de nanocomposites à matrice polyoléfines. Si ces nouveaux matériaux ont potentiellement de bonnes propriétés, leur comportement à long terme reste à être évalué. Les conséquences de l’ajout de nanoargile sur leur durabilité reste un sujet peu exploré malgré le nombre impressionnant de publications traitant des nanocomposites.

Notre objectif dans ce travail consistait en l’étude approfondie de l’influence de l’ajout de nanoargiles dans le processus de thermoxydation des polyoléfines à températures modérées (60°C < T < 100°C). Pour cela on a étudié deux systèmes :

- Un nanocomposite constitué de charges de type montmorillonite organiquement modifiée et d'une matrice *PP* incorporant un agent de couplage à base polypropylène.
- Un nanocomposite constitué de charges de type montmorillonite organiquement modifiée et d'une matrice *PE* incorporant un agent de couplage à base polyéthylène.

Concernant le nanocomposite à matrice *PP*, les propriétés générales suivantes ont été déterminées :

- ✓ La perméabilité à l'oxygène du nano composite est réduite de 45% comparativement à la matrice seule.
- ✓ Un effet catalytique associé à la présence d'éléments métalliques initialement présent dans la *MMT-O* conduit à augmenter la vitesse d'oxydation.

Une modélisation cinétique de l'oxydation du nanocomposite a été mise en place, elle décrit avec succès le processus de dégradation que ce dernier soit contrôlé ou non par la diffusion d'oxygène.

Concernant le second système nanocomposite à matrice *PE*, nos travaux ont mis en évidence les aspects suivants :

- Pas d'influence significative de l'argile sur les propriétés de perméabilité, ceci pouvant être expliqué par le fait que l'état de dispersion des feuillets d'argile est seulement de type intercalé et non pas exfolié.

- Au cours d'une oxydation homogène dans l'épaisseur et donc non contrôlée par la diffusion d'oxygène, nous avons mis en évidence et quantifié un effet catalytique induisant un nouvel amorçage par décomposition des hydropéroxydes.

- En comparant les taux de cristallinités déterminés en *AED*, en diffraction des rayons *X* et par densimétrie au cours de l'oxydation du *PEBD* et du nanocomposite, le processus de chimie-cristallisation qui engendre des coupures de chaînes, semble induire à haut taux de conversion la création d'une quantité significative d'interphase ou d'une mésophase ayant une densité intermédiaire à celle des phases amorphe et cristalline.

Par ailleurs, le processus conduisant à la dégradation a été modélisé avec succès : les simulations ont permis non seulement de décrire les modifications chimiques mais aussi les variations de perméabilité à une échelle macroscopique. La stratégie adoptée conduit à l'étude des phénomènes se produisant à une échelle morphologiques (chimie-cristallisation) permettant de relier les échelles moléculaires aux échelles macroscopiques. Cette approche multi-physique a permis de simuler l'ensemble des modifications induites par l'oxydation avec des paramètres parfaitement définis.

- ✓ Dans le cas des échantillons épais exposés à 100°C, aucun gradient d'oxydation significatif n'a été mis en évidence pour la matrice pure, alors que pour le nanocomposite, des couches oxydées de 520 µm ont été détectés dans l'épaisseur aux fortes conversions. L'apparition de ces couches oxydées est la conséquence d'une augmentation de la vitesse d'oxydation due à l'effet catalytique, le coefficient de diffusion de l'oxygène restant peu affecté par la présence de la charge.

D'une façon complémentaire aux profils de carbonyle, des mesures de modules à une échelles de quelques dizaines de microns, ont permis aussi de mettre en évidence cette oxydation hétérogène dans l'épaisseur et ont confirmé l'ordre de grandeur de l'épaisseur de couche oxydée.

- ✓ Les profils de dégradation dans l'épaisseur ont été modélisés en utilisant notre modèle cinétique d'oxydation incluant la diffusion d'oxygène : les simulations décrivent avec succès les profils en carbonyle à bas taux de conversion mais aussi les profils de module en se basant sur les relations structure-propriétés disponibles dans la littérature et en prenant en compte l'évolution des taux de cristallinité mesurés en AED. Ces premières simulations constituent une première approche dans la prédiction du comportement mécanique de pièces épaisses au cours d'un vieillissement oxydant.

Pour les taux de conversion élevés (c'est-à-dire proche de la surface des échantillons dans le cas des échantillons épais), les prédictions de concentration en carbonyle sont supérieures aux mesures, la raison pourrait en être le rôle joué par l'interphase ou la mésophase qui devrait être moins sensible à l'oxydation, un peu à l'image du cristal vis-à-vis de la phase amorphe. Le rôle de cette mésophase sur les propriétés élastiques semble très modéré, mais logique si on suppose comme certains groupes de recherche que cette mésophase possède une relaxation autour de -30°C, relaxation qui correspondrait à la relaxation β du *PE*.

Enfin, les perspectives après ce travail sur la dégradation oxydante de nanocomposite à matrice polyoléfines sont les suivantes :

- D'un point de vue expérimental, il serait judicieux d'explorer des systèmes polyoléfines/nanocharges présentant différents degrés d'exfoliation, cela permettrait de prendre en compte le degré d'exfoliation dans une modélisation de la durée de vie.

- Parallèlement, l'utilisation de différents types d'argile présentant différents types de traitements organiques devrait permettre d'évaluer leur pouvoir catalytique respectif sur le processus d'oxydation.

- En se basant sur ce travail qui ne traite que de systèmes sans stabilisant, l'étape suivante serait d'étudier les possibles interactions entre les nanocharges et les stabilisants, ces derniers étant nécessairement utilisés dans les formulations industrielles.

- Enfin, suite à nos travaux, il apparait nécessaire d'approfondir les recherches concernant le processus d'oxydation à forts degrés de conversion, d'un point de vue expérimental, avec une étude approfondie de la morphologie du *PE* oxydé afin de caractériser la mésophase et son rôle, notamment par spectroscopie Raman, *SAXS* et nano-indentation en faisant varier la température..

OXYDATION DES NANOCOMPOSITES A MATRICE POLYOLEFINIQUE

RESUME : Les matériaux nanocomposites suscitent un intérêt grandissant en recherche dû au fait qu'ils améliorent les propriétés barrières en incorporant une faible quantité de nanocharges inférieure à 5%. Actuellement, les montmorillonites organiquement modifiées (*MMT-O*) sont les nanocharges les plus répandues grâce à leur rapport de forme élevé permettant de favoriser les interactions surfaciques argile/polymère. Si ces matériaux présentent d'excellentes performances, leur durabilité et l'impact de la présence d'argile dans la matrice polymère n'a pas encore été étudiée en profondeur. Notre objectif était d'étudier finement le comportement vis-à-vis de l'oxydation de nanocomposites à matrice polypropylène et polyéthylène non stabilisés afin de mettre en évidence les effets de l'argile sur le processus d'oxydation aux faibles températures Ces effets ont deux origines : une origine chimique et une origine physique. Pour étudier ces deux origines, une démarche expérimentale et de modélisation du processus d'oxydation contrôlée ou non par la diffusion d'oxygène (respectivement dégradation hétérogène et homogène) a été mise en place. D'une manière générale, il apparait que la présence de *MMT-O* accélère l'oxydation. Ce phénomène a été modélisé par l'ajout de réaction catalytique entre les particules métalliques initialement présentes dans la *MMT-O* et les hydroperoxydes liés à l'oxydation. Concernant l'effet de la *MMT-O* sur la perméabilité à l'oxygène, deux cas ont été observés : dans le cas du système à base polypropylène (morphologie intercalée/exfoliée), une diminution de 45% de perméabilité a été mesurée par rapport à la matrice seule, alors que dans le cas du système à base de polyéthylène (morphologie intercalée), pas de variation significative a été détectée. Les cinétiques et les profiles dans l'épaisseur des échantillons des produits d'oxydation ont été mesurés et simulés par un modèle couplant réactions d'oxydation et diffusion d'oxygène dans les deux systèmes. Dans le cas du système à matrice polyéthylène, les modifications induites par l'oxydation sur les masses molaires et sur la morphologie cristalline sont prédites. Enfin, en se basant sur des relations structure-propriétés, des profils de module mécanique ont été simulés dans le cas de la dégradation hétérogène (oxydation contrôlée par la diffusion). Ces simulations ont été confirmées par des mesures de modules dans l'épaisseur d'échantillons épais de nanocomposite à matrice polyéthylène oxydés.

Mots clés : Nanocomposite, Oxydation, Cinétique, Argile.

OXIDATION OF NANOREINFORCED POLYOLEFINS

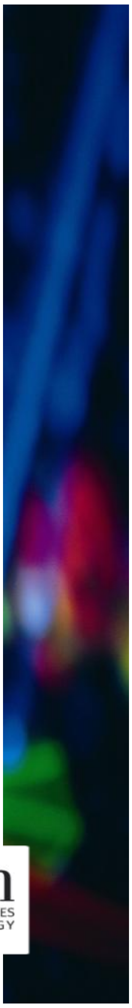

ABSTRACT: Nanocomposite materials attract search due to their improvements on barrier properties by incorporating low level of nanofiller of 5%w. Nowadays, organically modified montmorillonites (*MMT-O*) are the most used fillers due to their high aspect ratio which permits stronger clay/polymer interactions. If nanoreinforced materials are highly performing, the ways in which clay presence affects polyolefin durability have not being subject of a rigorous study, thus they are not yet clear. Our goal was to examine unstabilized clay polypropylene and unstabilized clay polyethylene nanocomposites to get a better comprehension of the clay effects on their thermooxidation process under low temperatures. The effects induced by a dual physic –chemical nature of the clay were explored. The problem was tackled from both experimental and theoretical point of views for degradation process not controlled and controlled by oxygen diffusion (homogenous and heterogeneous respectively). It seems that *MMT-O* speeds up oxidation. This phenomenon was modeled by adding a catalytic reaction between metallic particles initially present in the *MMT-O* and hydroperoxyde groups (main responsible of oxidation). Regarding the oxygen permeability two situations were confronted: for the clay polypropylene system a decrease of 45% of oxygen permeability was measured. On the other hand, no variation was found for the polyethylene case. This effect was attributed to the fact that polyethylene nanocomposite reached a blend morphology less developed than those of the polypropylene nanocomposite. Kinetics and oxidation products profiles across the sample thickness were simulated for both systems by coupling oxidation reactions with oxygen diffusion equations. For the polyethylene case, the effects induced by oxidation on molar mass and crystalline morphology were also simulated. Finally, based on structure – property relation, simulations of mechanic modulus profiles were performed for the heterogeneous degradation case (oxidation diffusion controlled). These results were confirmed by experimental measurements of modulus across the thickness of thick clay polyethylene nanocomposite samples.

Keywords : Nanocomposite, Oxidation, Kinetics, Clay.